

ASPECTS OF THE MAGNETOSPHERIC AMPLIFICATION PHENOMENON  
IN DUCTED WHISTLER-MODE WAVES

A DISSERTATION  
SUBMITTED TO THE DEPARTMENT OF ELECTRICAL ENGINEERING  
AND THE COMMITTEE ON GRADUATE STUDIES  
OF STANFORD UNIVERSITY  
IN PARTIAL FULFILLMENT OF THE REQUIREMENTS  
FOR THE DEGREE OF  
DOCTOR OF PHILOSOPHY

Thomas A. Mielke

December, 1993

©by Thomas A. Mielke 1993  
All Rights Reserved

I certify that I have read this dissertation and that in my opinion it is fully adequate, in scope and quality, as a dissertation for the degree of Doctor of Philosophy.



---

Robert A. Helliwell (Principal Advisor)

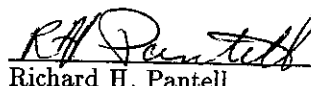
I certify that I have read this dissertation and that in my opinion it is fully adequate, in scope and quality, as a dissertation for the degree of Doctor of Philosophy.



---

Umran S. Inan

I certify that I have read this dissertation and that in my opinion it is fully adequate, in scope and quality, as a dissertation for the degree of Doctor of Philosophy.



---

Richard H. Pantell

Approved for the University Committee on Graduate Studies:

---

## Abstract

Interactions between ducted whistler-mode waves and energetic particles in the magnetosphere often lead to strong wave amplification, characteristically associated with such non-linear effects as the appearance of sidebands and triggering of free-running emissions. Experiments at Siple Station, Antarctica, were conducted to study the growth process. Data from the experiment on antenna polarization effects on coupling of wave energy into the whistler-mode agree well with theory. Results of experiments aimed at determining the wave-particle interaction underlying the observed wave growth were consistent with a gyro-resonance interaction but not with a Landau resonance interaction. Experiments using pulses with parabolic rather than linear frequency chirps also produced wave growth, providing the capability to test theories of the effects of spatial variations on the wave growth process. A further observed phenomenon, that of a wave power threshold below which the growth and emissions effect does not occur, was also investigated. While very suggestive, data from an experiment on the effects of artificial noise on the threshold level fail to conclusively discriminate between competing theories of wave growth (involving trapped versus non-trapped electrons interacting with the whistler-mode wave).

## Acknowledgments

I wish to thank my principal advisor, Professor R. A. Helliwell, and associate advisor, Professor U. S. Inan for their guidance and support. I also wish to thank my third reader, Professor R. H. Pantell, for his gracious assistance. Professor D. L. Carpenter gave both technical and moral support. Dr. T. F. Bell and Dr. V. S. Sonwalkar read parts of this manuscript and made valuable suggestions. Mr. Christopher Elkins performed most of the data analysis on the antenna polarization experiments. Mr. John Katsufakis managed the field programs in which the data were acquired, and Mr. William Trabucco, Mr. Evans Paschal, Mr. Thomas Wolf, and Mr. David Shafer designed and installed the polarization controller at Siple Station. Mr. James Logan and Mr. William Trabucco, in succession, operated the Siple Station VLF transmitter during the 1986-87 and 1987-88 seasons. Mr. Jerry Yarbrough provided tremendous assistance in the collection and spectral analysis of the data used in this research.

This research was supported by the Division of Polar Programs of the National Science Foundation under grants DPP 86-13783 and DPP 89-18326, and by the National Aeronautics and Space Administration under grant NAG5-476.

# TABLE OF CONTENTS

<u>Chapter</u>	<u>Page</u>
I. Introduction .....	1
A. The Plasma Environment in the Vicinity of the Earth .....	1
B. Wave Growth and Triggered Emissions in the Magnetosphere .....	1
C. Proposed Theories of Wave Growth in the Magnetosphere .....	6
D. Scaling Requirements for Laboratory Experiments .....	7
E. Contributions of this Research .....	7
II. Siple Station Experiments on Coupling of VLF waves into the magnetosphere .....	9
A. Background of the Experiment .....	9
B. Description of the Experiment .....	9
C. Antenna Coupling to the Whistler Mode .....	9
D. Observations of Ducted Signals with Discrete Paths .....	17
E. Observations of ducted signals with Multipath Effects Present .....	24
F. Observations of Ducted Signals with Single Path Propagation .....	24
G. Observations of Nonducted Signals .....	25
H. Summary and Discussion of the Transmitter Polarization Experiment .....	29
III. Siple Station Experiments on Wave-Particle Interactions with Linear Frequency "Chirps" and Frequency "Staircases" .....	30
A. Background of the Experiment .....	30
B. Experimental Data .....	30
C. Second Order Resonance Theory .....	36
D. Analytic Formulas .....	38
E. Comparison of Data and Theory .....	41
F. Summary of the Linear Frequency "chirp" Experiment .....	45
IV. Siple Station Experiments on Wave-Particle Interactions with Parabolic Frequency "Chirps" .....	46
A. Background of the Experiment .....	46
B. Description of the Experiment .....	46
C. Interpretation .....	51

D. Discussion of the Parabolic Frequency "Chirp" Experiment .....	53
V. Siple Station Experiments on the Threshold Effect in the Coherent Wave Instability .....	55
A. Background of the Experiment .....	55
B. Description of the Experiment .....	55
C. Data Interpretation .....	56
D. Conclusions of the Threshold Effect Experiment .....	61
VI. Summary and Conclusions .....	62
Appendix A. Survey of Siple Data and Suggested Future Work .....	64
Appendix B. Dispersion in the Plasmasphere .....	68
Appendix C. Third Order Gyroresonance Equations .....	71
Appendix D. Third Order Landau Resonance Equations .....	73
Appendix E. Some Criteria for Linking cw Pulses via Second Order Resonance .....	75
Bibliography .....	76

## LIST OF TABLES

<u>Table</u>		<u>Page</u>
1	Interaction lengths and encounter lengths for cw pulses .....	43
2	Phase deviations of frequency staircases relative to a resonant frequency ramp .....	43
3	List of Siple Station transmitter formats .....	66

## LIST OF ILLUSTRATIONS

<u>Figure</u>	<u>Page</u>
1.1 Sketch of the magnetosphere. ....	2
1.2 Whistler example. ....	3
1.3 Outline of Siple Station VLF active experiments. ....	4
1.4 Coherent Wave Instability example. ....	5
2.1 Siple antenna layout. ....	10
2.2 Whistler mode excitation at the air-ionosphere boundary. ....	11
2.3 Plots of power coupled into the whistler mode for various antenna polarizations. ....	15
2.4 Polarization experiments with transmitted frequency ramps. ....	16
2.5 Propagation path observations for Siple signals and whistlers with identical time delays. ....	19
2.6 Path selectivity of polarized transmissions. ....	20
2.7 Estimation of path endpoint location. ....	21
2.8 Multipath ducted signals. ....	22
2.9 Magnetospheric growth of Siple signals. ....	23
2.10 Saturated power on single-path propagation. ....	26
2.11 Satellite observation of nonducted Siple signals. ....	27
2.12 Wave amplitude observed on DE-1 satellite from the Siple Station transmitter. ....	28
3.1 Whistler-mode wave and energetic electron. ....	31
3.2 Magnetospheric growth on the rising frequency ramp, 10 ms and 25 ms rising frequency staircases, but not on the 50 ms staircase and 100 ms staircase. ....	32
3.3 Magnetospheric growth on the falling frequency ramp, 10 ms and 25 ms falling frequency staircases, but not on the 50 ms staircase and 100 ms staircase. ....	33
3.4 Magnetospheric growth on the +25 ms sawtooth, -25 ms sawtooth, and cw pulse. ....	34
3.5 Example of the "dot-dash anomaly". ....	35
3.6 Interaction lengths for the STACO frequency ramps and cw pulse. ....	42
3.7 Stronger magnetospheric growth on rising frequency staircases, cw pulses and sawtooth pulses than on falling frequency staircases. ....	44
4.1 Natural and artificial nose whistlers with magnetospheric growth and emissions. ....	47
4.2 Simulated nose whistler and constant frequency pulse. ....	48
4.3 NOWS cluster and diagnostic sequence. ....	49
4.4 Schematic of the NOWS interaction. ....	52

5.1	The NETH (Noise Effect on Threshold) experiment, showing the suppression of the CWI by simulated noise. ....	57
5.2	Number of triggered emissions versus intensity of the simulated noise. ....	58
5.3	Natural noise near the expected CWI interaction region observed by the DE-1 satellite. ....	59
5.4	Histogram of natural noise intensity observed on DE-1 with the noise level estimated by the NETH experiment indicated. ....	60

## I. Introduction

### A. THE PLASMA ENVIRONMENT IN THE VICINITY OF THE EARTH

The interaction of the solar wind with the magnetic field of the earth leads to a complex plasma environment, called the magnetosphere, which is sketched in Figure 1.1. This dissertation is particularly concerned with the plasmasphere, a region of relatively dense plasma near the earth (within about five earth radii), indicated in Figure 1.1. The plasmasphere is a region where the magnetic field is still, to a good approximation, that of a dipole situated at the center of the earth. Energetic electrons and ions, confined by the dipole field, form the radiation belts. In addition to these energetic particles ("hot plasma"), a relatively dense "cold plasma" background is also found in this region. The cold plasma is not always smooth; ducts of slightly enhanced plasma density which are aligned with the dipole field often form. These ducts guide Very Low Frequency (VLF) radio waves just as a graded-index fiber optic cable guides light waves. Ducted VLF waves propagate in the "whistler" mode. A VLF signal injected into the magnetosphere in one hemisphere can emerge in the opposite hemisphere with considerable distortion. The distortion caused by dispersion in the whistler mode is well understood; distortion associated with wave growth is not. An example of whistler mode dispersion is shown in Figure 1.2. In this spectrogram of radio data recorded at Byrd Station, Antarctica, (frequency is displayed on the vertical axis versus time on the horizontal axis), radio atmospherics (sferics) and whistlers can be seen. A sferic is an impulsive event caused by lightning, which covers a wide frequency range for a short time. An excellent example can be seen at 1.8 seconds. A sferic which propagates through the magnetosphere in a duct emerges as a whistler. This is due to dispersion in the whistler mode; wave group velocity (and hence delay) is a function of frequency. An example can be seen at 2-4 seconds.

### B. WAVE GROWTH AND TRIGGERED EMISSIONS IN THE MAGNETOSPHERE

Numerous experiments on magnetospheric VLF propagation have been conducted, as illustrated in Figure 1.3. VLF waves at 2-5 kHz are transmitted from Siple Station, Antarctica. Ducted whistler mode waves propagate through the cold plasma and also interact with the energetic electrons of the hot plasma. Receivers in Canada, at Roberval (RO) or Lake Mistissini (LM), record the ducted VLF waves after passage through the magnetosphere. Unducted whistler mode waves are also excited, and are recorded on the DE-1 satellite. If the VLF receivers can be monitored in real time (this is rarely the case), communications with Siple Station via the ATS-3 satellite permit immediate modification of the experiment. It should be noted that while a satellite could, in principle, fly through a duct in which a Siple Station transmission was propagating, the chances of such a serendipitous event are small. No such encounter has yet been reported.

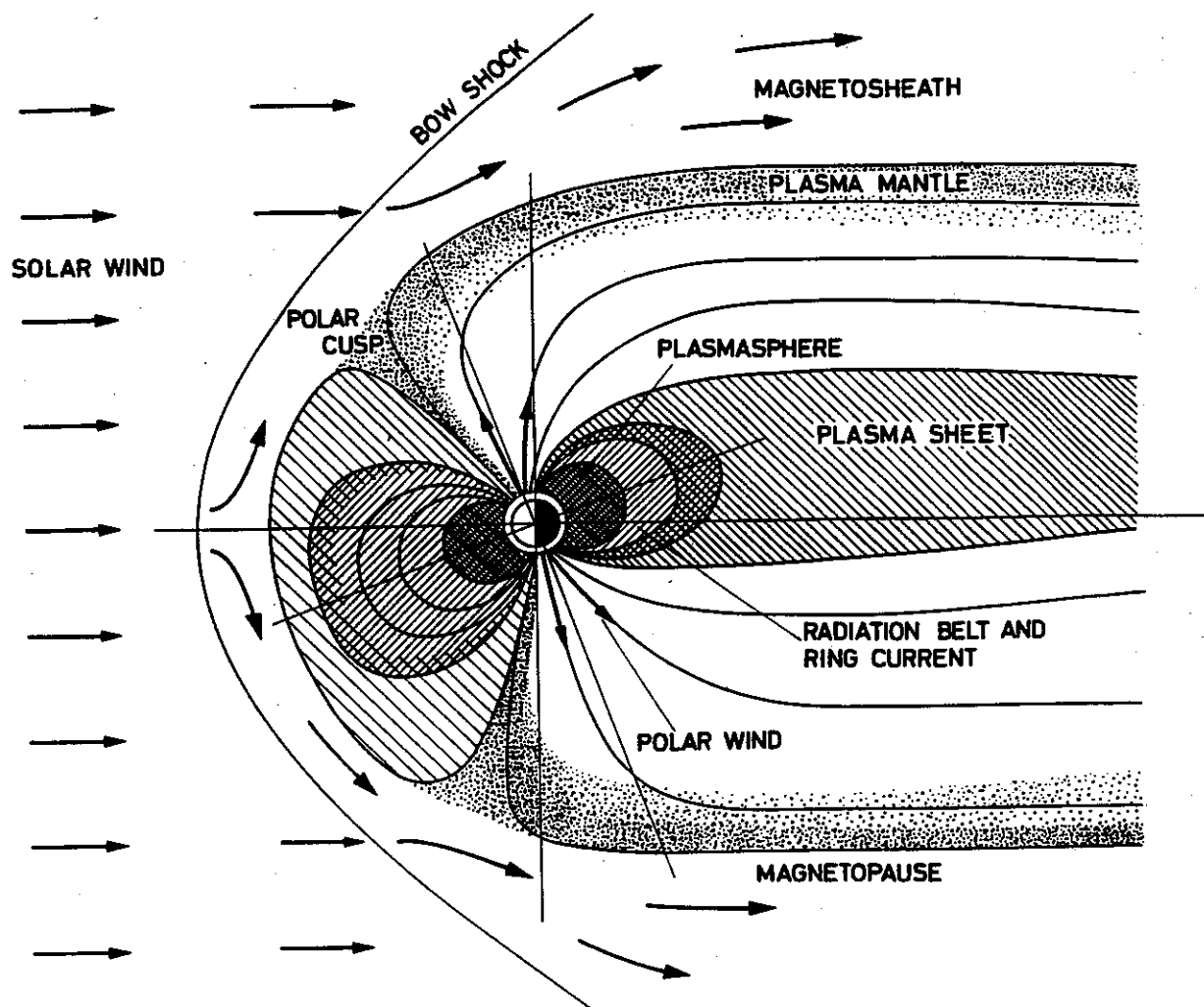


Figure 1.1. Sketch of the magnetosphere. After R. H. Eather, *Majestic Lights*, p. 219, 1980, copyright by the American Geophysical Union.

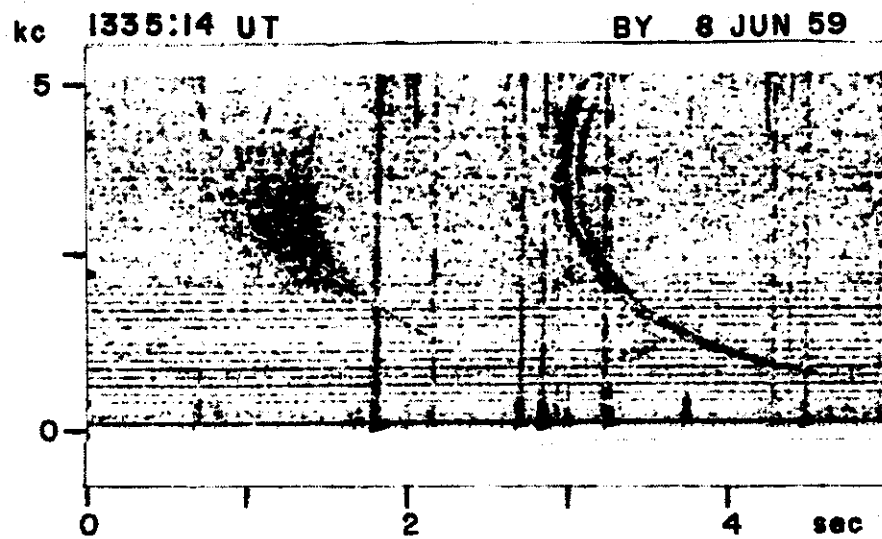


Figure 1.2. Whistler example. After R. A. Helliwell, *Whistlers and Related Ionospheric Phenomena*, p. 105, 1965, Stanford University Press.

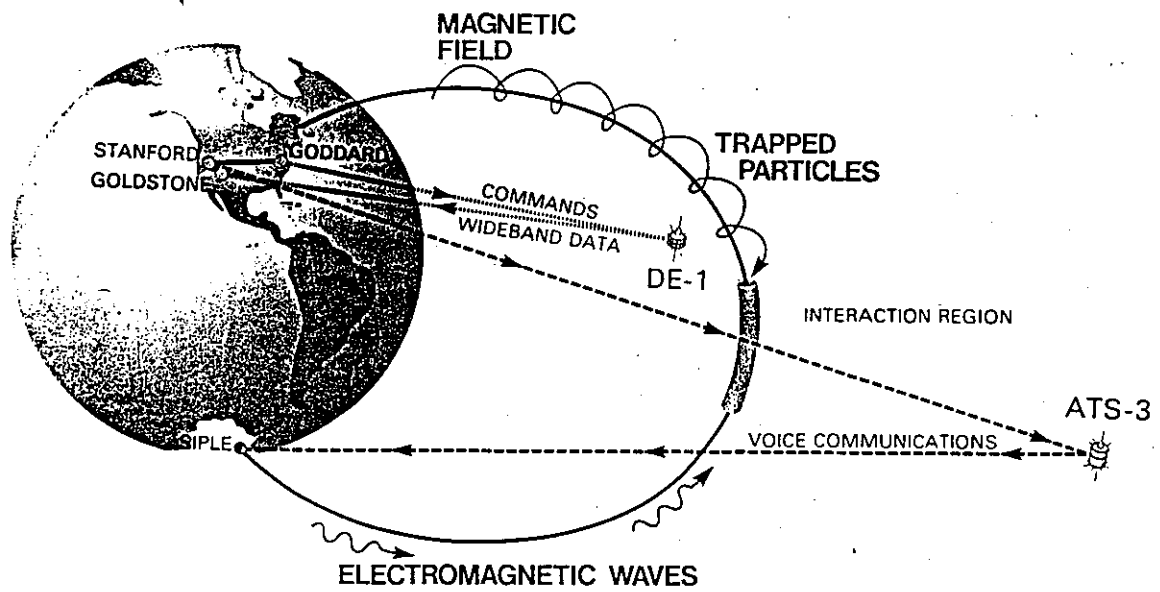


Figure 1.3. Outline of Siple Station VLF active experiments.

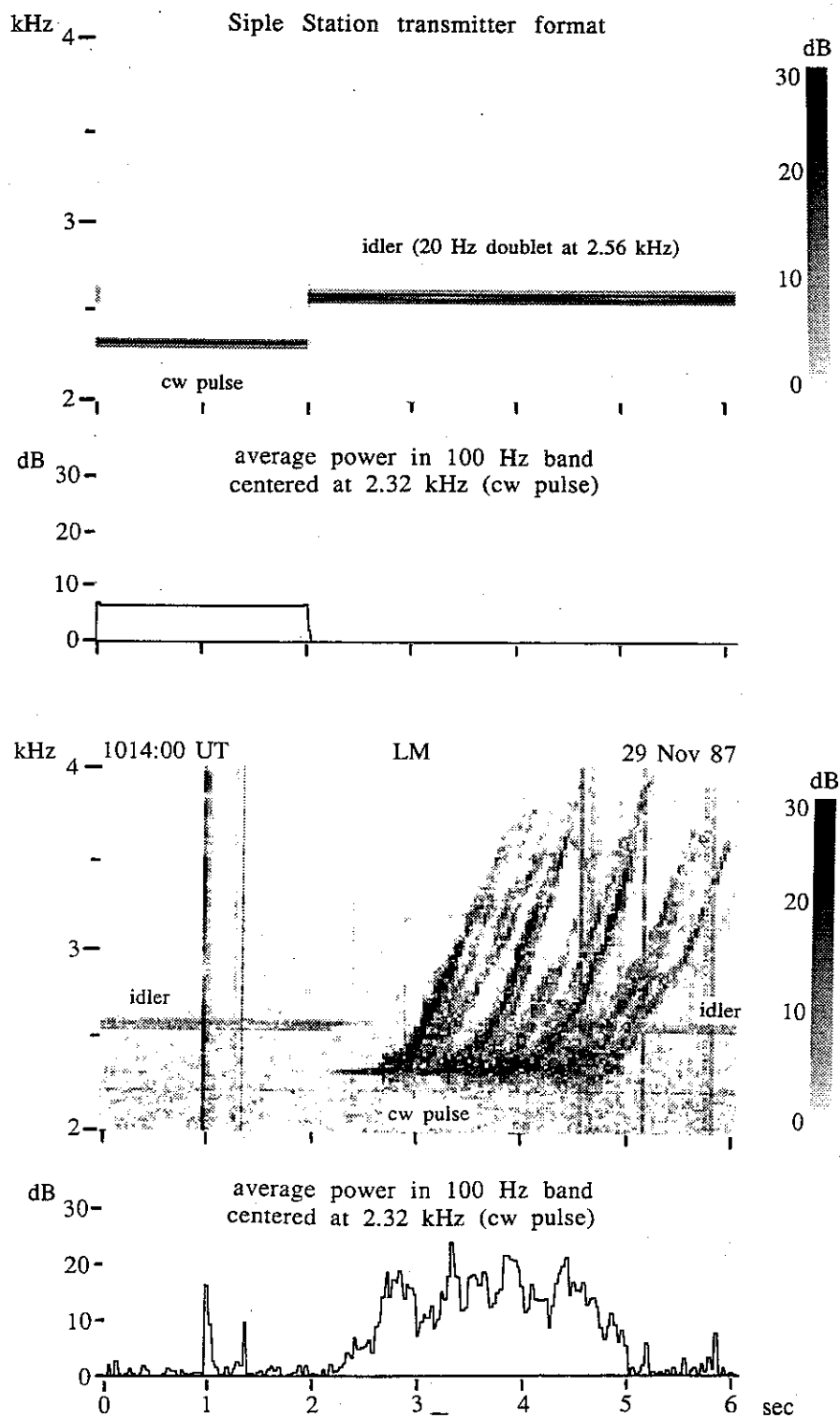


Figure 1.4. Coherent Wave Instability example.

Figure 1.4 shows an example of data from the Siple Station active experiments. It illustrates distortion caused by wave growth. This phenomenon is called the coherent wave instability (CWI) and is not fully understood. Spectra (frequency versus time) of the transmitted and received VLF signals are shown. Signal intensity is indicated by a grey scale on the spectra (a darker line is a more intense signal) and also by a power chart below the spectra. The transmission is as simple a signal as possible; a constant-frequency (cw), constant-amplitude pulse. At pulse start and termination, rather than turn the transmitter on and off, which produces undesirable stresses in the power supply, we switch to an "idler" signal. This idler consists of two constant frequencies spaced 20 Hz apart, which is observed to interact weakly with energetic electrons compared to a single constant frequency signal. The pulse received at Lake Mistissini after a 2 second propagation delay shows both amplitude and frequency modulation. (The idlers show no apparent change.) The coherent wave instability is not time invariant; with a constant input the output is time-dependent. The CWI is also not linear in the systems sense; doubling the input does not double the output. As linear, time-invariant systems are considerably easier to work with than nonlinear systems, the limited understanding of the CWI is understandable. Simulations are widely used to explain the observations [Carlson et. al., 1990; Molvig et. al., 1988].

### C. PROPOSED THEORIES OF WAVE GROWTH IN THE MAGNETOSPHERE

The CWI is thought to be due to interactions between the whistler mode wave and energetic electrons in which the electrons are slowed down and give up energy to the wave [Brice, 1964]. Such interactions are used in electron tubes to build amplifiers and oscillators [Chodorow and Susskind, 1964]. A wave-particle interaction is strongest at resonance, where the particle "sees" either a constant or periodic wave field. A constant field (in the electron frame of reference) should provide a stronger interaction than a periodic field, thus the higher order resonances may be neglected. There are two candidate interactions: Landau resonance and gyroresonance. The Landau resonance occurs when the electron velocity and wave propagation are in the same direction, and the electron parallel velocity equals the wave phase velocity. The gyroresonance occurs when the electron velocity and wave propagation are in opposite directions, and the Doppler-shifted wave frequency equals the electron gyrofrequency (also called cyclotron frequency). Under those circumstances, the spiral traced by the counterstreaming electron matches the helix of the circularly polarized whistler mode wave, and the electron "sees" a constant wave field. In either Landau resonance or gyroresonance, one might consider small-signal theories (in which the wave-particle interaction perturbs the electron's natural motion) or large-signal theories (in which the wave-particle interaction dramatically alters the electron trajectory). The Siple Station active experiments can be used to test at least some parts of coherent wave instability theories. As plasmas and plasma instabilities are important in a

variety of fields, ranging from astrophysics to fusion research, the Siple Station data set can have broad applications.

#### D. SCALING REQUIREMENTS FOR LABORATORY EXPERIMENTS

A different approach to study of the CWI would be to build laboratory plasma devices which, in suitably scaled form, reproduce the environment of the radiation belts. This is difficult, as the following example shows. From the magneto-ionic theory, scaling requires keeping the three ratios  $f/f_P$ ,  $f/f_H$ , and  $f/\nu$  constant. In addition, the laboratory device must be large enough that boundary effects are negligible. For the Siple Station experiments, typical magnetospheric conditions near the magnetic equator at a distance from the earth's center of 4.5 earth radii (McIlwain shell parameter  $L=4.5$ ) are: wave frequency  $f=3$  kHz, plasma frequency  $f_P=150$  kHz, gyrofrequency  $f_H=10$  kHz, and collision frequency  $\nu$  is negligible. If one requires a wavelength (in the plasma) on the order of 1 cm for the laboratory device, the corresponding scaled frequencies are:  $f=1$  GHz,  $f_P=50$  GHz (implying a density of  $2 \times 10^{17}$  per cc),  $f_H=3$  GHz (implying a magnetic field of  $2 \times 10^{-2}$  T), and a relatively high (on the order of GHz) collision frequency  $\nu$ . The high  $\nu$  relative to  $f$  prevents successful scaling. The collision frequency decreases as the plasma temperature increases, but a plasma temperature of greater than 4 keV is required before the collision frequency is again negligible compared to the wave frequency. Such specifications are technically challenging [Chen, 1984].

#### E. CONTRIBUTIONS OF THIS RESEARCH

The remaining chapters cover Siple Station experiments on the coupling of VLF waves from the antenna into the magnetosphere and wave-particle interactions in the magnetosphere. Four papers have been published on these topics[Helliwell et al, 1990; Mielke et al, 1992; Mielke and Helliwell, 1992; Mielke and Helliwell, 1993], which are adapted here for the purposes of this dissertation. Contributions made by the author in the course of this research include:

- Derivation of an analytic theory of coupling from the Siple Station antenna to whistler-mode signals in the magnetosphere, which was found to be consistent with observations of Siple Station transmitter signals at Lake Mistissini and on the Dynamics Explorer-1 satellite.
- Application of the coupling theory and dispersion data to identify likely duct end point locations.
- Extension of analytic second order gyroresonance theory to regions farther from the magnetic equator, permitting application of analytic theory to frequency ramps with larger  $df/dt$  than was previously possible.
- Application of the extended second order gyroresonance theory to experimental data from Siple Station transmissions, which provided confirmation of the gyroresonance mechanism in the

beginning stages of the CWI, and an explanation of the breakdown of wave growth for coarse frequency "staircase" approximations to a frequency ramp.

- Analysis of experimental data showing magnetospheric growth and triggered emissions on pulses with parabolic frequency-versus-time "chirps". As growth of such parabolic "chirps" via second order gyroresonance occurs away from the magnetic equator, this phenomenon could be used to probe the plasma environment on open magnetic field lines, outside the plasmasphere.

- Analysis of experimental data on the "threshold effect" [Helliwell et al, 1980], in which the transmitted wave intensity must exceed some threshold intensity before the CWI is excited. This experiment tested the hypothesis that in-situ hiss is responsible for the threshold effect. Results were consistent with the "in-situ hiss" hypothesis.

## II. Siple Station Experiments on Coupling of VLF Waves Into the Magnetosphere

Much of this material was reported in [Mielke et al, 1992], and is adapted here for summary and discussion.

### A. BACKGROUND OF THE EXPERIMENT

Magneto-ionic theory as applied in a homogeneous medium with a vertical magnetic field and a sharp lower boundary predicts that an upgoing right-hand circular polarized wave normally incident on the lower ionosphere would couple twice as much power into the whistler mode as a linear polarized wave of the same strength, and a left-hand circular polarized wave would fail altogether to couple into the whistler mode [Budden, 1985]. Thus only right-hand whistler mode waves are expected to be launched into the ionosphere, regardless of antenna polarization. This is a fair approximation of coupling into an overhead duct from an antenna on the ground in polar regions. Experiments made at Siple Station, Antarctica, Lake Mistissini, Quebec, and on the DE-1 satellite in 1986 displayed the expected results. A simple model of the coupling from a horizontal dipole antenna into the ionosphere and to variously positioned ducts can, in conjunction with observed multipath and magnetospheric wave growth, account for the observed data.

### B. DESCRIPTION OF THE EXPERIMENT

Siple station, Antarctica (76 S, 84 W) rests atop some two kilometers of ice. This permits large horizontal half-wave dipole antennas on the surface to operate with  $\approx 1-3\%$  efficiency [Raghuram et al, 1974]. At the time of the experiments described, two 21 km crossed dipoles (see Figure 2.1) were in use. These antennas were laid out in the magnetic north-south and magnetic east-west directions. Six antenna polarizations were used: right-hand circular (abbreviated RH), left-hand circular (abbreviated LH), linear along a northeast-southwest axis (abbreviated D1), linear along a northwest-southeast axis (abbreviated D2), linear along a north-south axis (abbreviated NS), and linear along an east-west axis (abbreviated EW). Transmissions were made from Siple Station, with receivers at Lake Mistissini, Quebec near the geomagnetic conjugate point and on the Dynamics Explorer-1 (DE-1) satellite. Various sequences (designated POLAD, POLA1, and POLA2) of constant-frequency pulses, interspersed with pulses with linearly varying frequency, were sent. Further details of the transmitter-receiver configurations can be found elsewhere [Helliwell, 1988].

### C. ANTENNA COUPLING TO THE WHISTLER MODE

The Siple station antenna layout is sketched in Figure 2.1. Radiation at frequencies from 2 to 12 kHz is incident on the ionosphere at a height of 70 to 90 km and generates whistler-mode waves in the magnetosphere.



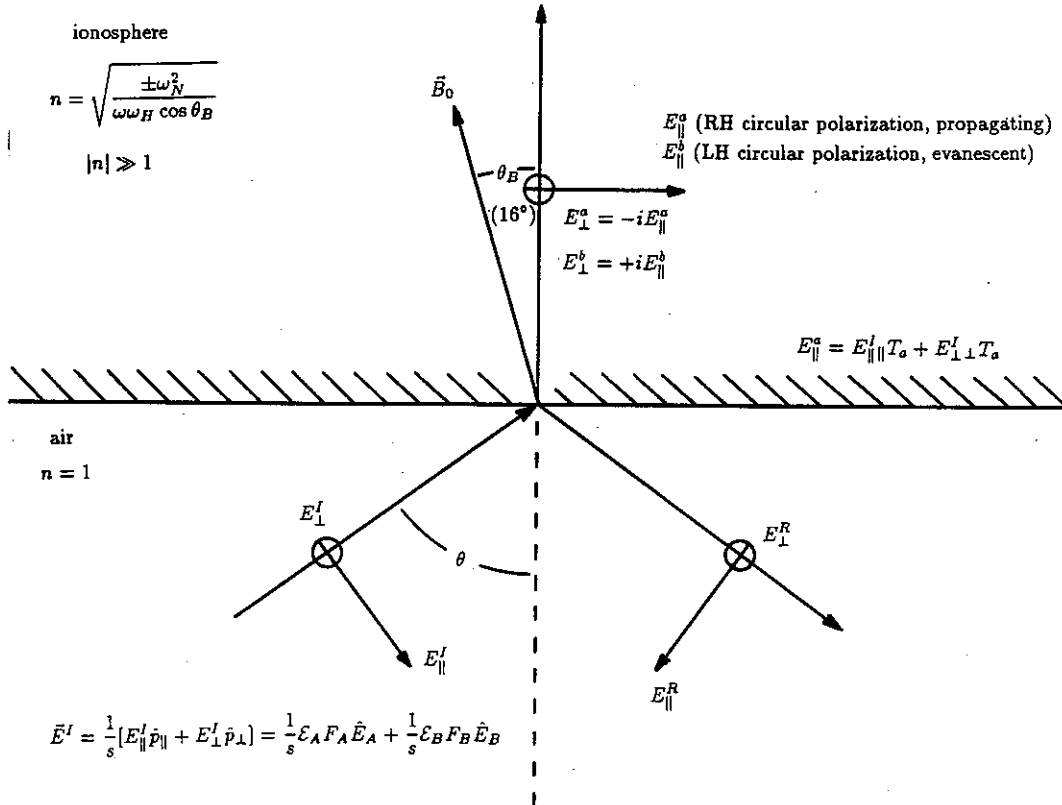


Figure 2.2. Whistler mode excitation at the air-ionosphere boundary. After [Mielke et. al., 1992].

The dependence of the whistler-mode excitation on azimuth ( $\phi$ ), zenith angle ( $\theta$ ), and antenna polarization is developed here. Numerous approximations are employed in order to obtain closed form expressions. The major assumptions are:

- 1) The ionosphere is treated as an abrupt boundary, a common assumption in VLF problems [Budden, 1985]. This is justified by the large free space wavelengths (on the order of 25 to 150 km) and the sharp boundary of the lower ionosphere (density changes from  $10^{-2} \text{ cm}^{-3}$  to  $10^{+1} \text{ cm}^{-3}$  within  $< 10 \text{ km}$ ) [Inan et al, 1988].
- 2) At any given patch of ionosphere, the direct ray from the transmitter and the ray reflected from the ice surface are combined into a single ray with constant phase and amplitude, independent of zenith angle  $\theta$ . Polarization of this composite ray is that of the direct ray from the transmitter. Given the measured permittivity of Antarctic ice [Peden et al, 1972] the reflection at the ice surface is nearly independent of both incidence angle and polarization up to a zenith angle of  $\approx 60$  degrees. As the antenna is typically 2 to 3 meters (less than 0.1% of a wavelength) above the surface of the ice, the path length difference between the direct ray and ice reflection is negligible.
- 3) Above 6 kHz, the reflection from the rock beneath the ice is ignored. This ray must typically travel through several skin depths of ice and so is much weaker than the combination of direct ray and ice reflection. Below 6 kHz, the ice attenuation is weaker but due to the large relative permittivity of the ice sheet ( $\epsilon_r = 25 + j36$  at 4 kHz for example) the ray in the ice is nearly vertical regardless of incidence angle at the air-ice boundary. Thus the phase of the ray reflecting from the rock is nearly independent of zenith angle (in air) and this ray can be combined with the direct ray and ice reflection to produce a composite ray with phase and amplitude independent of zenith angle.
- 4) As observations are taken at great distances from Siple station near-field antenna terms are ignored. This is clearly the case for both Lake Mistissini ground data and DE-1 high altitude satellite data.

With a slab model of the ionosphere and assumed incident plane waves the transmission coefficients for the excitation of whistler-mode waves by parallel and perpendicular incident waves can be calculated. This is illustrated in Figure 2.2, with the transmission coefficients for  $n \gg 1$  and  $\theta < 60$  degrees derived from Budden [1961]. The earth's magnetic field at Siple Station ( $\vec{B}_0$ ) is 16.2 degrees from the vertical, directed upward. This value was used in Budden's approximate formulas. After much algebra, the incident parallel and perpendicular waves can be expressed in terms of the antenna excitations. Because of the ice and rock reflections discussed above, the effective antenna excitations (current in an ideal dipole in free space to obtain the same radiated power) are estimated to be about 25% of the actual antenna current. The resulting theory of coupling from antenna to whistler-mode describes the essential physics of the process. High accuracy should not be expected

from so simple a model, but the trends it predicts should be reliable. Using the following definitions,

$\vec{E}^I$  = incident wave on air-ionosphere boundary

$E_{\parallel}^a$  = transmitted wave in ionosphere (RH circular polarization, propagating)

$E_{\parallel}^b$  = transmitted wave in ionosphere (LH circular polarization, evanescent)

$\mathcal{E}_A = |\mathcal{E}_A|e^{i\delta_A}$  = N-S antenna excitation

$\mathcal{E}_B = |\mathcal{E}_B|e^{i\delta_B}$  = E-W antenna excitation

$F_A$  = N-S antenna pattern

$F_B$  = E-W antenna pattern

$\hat{E}_A$  = N-S antenna field unit vector

$\hat{E}_B$  = E-W antenna field unit vector

$\hat{p}_{\parallel}$  = parallel field unit vector

$\hat{p}_{\perp}$  = perpendicular field unit vector

$s$  = slant distance to antenna

$_{\parallel}T_a = \frac{1}{|n|} =_{\parallel}$  to RH transmission coefficient

$_{\perp}T_a = \frac{i \cos \theta}{|n|} =_{\perp}$  to RH transmission coefficient

$n = \sqrt{\frac{\pm \omega_N^2}{\omega \omega_H \cos \theta_B}}$  = refractive index in ionosphere

$n_a = |n|$  = ordinary wave (whistler mode) refractive index

$n_b = -i|n|$  = extraordinary wave refractive index

$\delta_A$  = N-S antenna phase

$\delta_B$  = E-W antenna phase

$L$  = antenna length

$h$  = ionosphere height

$P^a = n_a |E_{\parallel}^a|^2$  = whistler-mode power,

the general case is :

$$P^a = \frac{\cos^4 \theta}{|n|h^2} \left[ |\mathcal{E}_A|^2 \left( \frac{\cos(\frac{\pi L}{\lambda} \sin \theta \cos \phi) - \cos(\frac{\pi L}{\lambda})}{1 - \sin^2 \theta \cos^2 \phi} \right)^2 + |\mathcal{E}_B|^2 \left( \frac{\cos(\frac{\pi L}{\lambda} \sin \theta \sin \phi) - \cos(\frac{\pi L}{\lambda})}{1 - \sin^2 \theta \sin^2 \phi} \right)^2 \right. \\ \left. + 2|\mathcal{E}_A||\mathcal{E}_B| \left( \frac{\cos(\frac{\pi L}{\lambda} \sin \theta \cos \phi) - \cos(\frac{\pi L}{\lambda})}{1 - \sin^2 \theta \cos^2 \phi} \right) \left( \frac{\cos(\frac{\pi L}{\lambda} \sin \theta \sin \phi) - \cos(\frac{\pi L}{\lambda})}{1 - \sin^2 \theta \sin^2 \phi} \right) \sin(\delta_B - \delta_A) \right]$$

Two interesting special cases are  $L \ll \lambda$  (short dipole)

$$P^a = \frac{\cos^4 \theta}{|n|h^2} [|\mathcal{E}_A|^2 + |\mathcal{E}_B|^2 + 2|\mathcal{E}_A||\mathcal{E}_B| \sin(\delta_B - \delta_A)]$$

and  $L = \lambda/2$  (half-wave dipole)

$$P^a = \frac{\cos^4 \theta}{|n|h^2} \left[ |\mathcal{E}_A|^2 \left( \frac{\cos(\frac{\pi}{2} \sin \theta \cos \phi)}{1 - \sin^2 \theta \cos^2 \phi} \right)^2 + |\mathcal{E}_B|^2 \left( \frac{\cos(\frac{\pi}{2} \sin \theta \sin \phi)}{1 - \sin^2 \theta \sin^2 \phi} \right)^2 + 2|\mathcal{E}_A||\mathcal{E}_B| \frac{\cos(\frac{\pi}{2} \sin \theta \cos \phi)}{1 - \sin^2 \theta \cos^2 \phi} \frac{\cos(\frac{\pi}{2} \sin \theta \sin \phi)}{1 - \sin^2 \theta \sin^2 \phi} \sin(\delta_B - \delta_A) \right]$$

The following antenna excitation values correspond to the experimental polarizations used at Siple Station:

RH:  $|\mathcal{E}_A| = |\mathcal{E}_B|$  and  $\delta_B - \delta_A = \pi/2$

LH:  $|\mathcal{E}_A| = |\mathcal{E}_B|$  and  $\delta_B - \delta_A = -\pi/2$

D1:  $|\mathcal{E}_A| = |\mathcal{E}_B|$  and  $\delta_B - \delta_A = 0$

D2:  $|\mathcal{E}_A| = |\mathcal{E}_B|$  and  $\delta_B - \delta_A = \pi$

N-S:  $|\mathcal{E}_B| = 0$

E-W:  $|\mathcal{E}_A| = 0$

At the zenith, both half-wave and short crossed dipole antennas give the same result. The major difference between results occurs for the LH transmitter polarization. In that case the half-wave dipole antenna will excite the whistler-mode off the zenith and away from the azimuth angles of 45, 135, 225, and 315 degrees (which form symmetry axes when both antennas are equally excited), while the short dipole antenna with LH polarization does not excite the whistler-mode at any azimuth. Plots of the whistler-mode power (coupled into the base of the ionosphere from the half-wave crossed dipole antenna) as a function of azimuth and distance from Siple Station are shown in Figure 2.3.

The determination of the ionospheric entry or exit points of a ducted whistler-mode signal is difficult [Burgess, 1993] and is only discussed in general terms in one of the cases studied. Uncertain ionospheric absorption and propagation losses make absolute signal strengths difficult to obtain. In this paper, ratios of received signal strengths for different given transmitting antenna polarizations constitute the available experimental data. Because of the nulls in whistler-mode excitation for LH antenna polarization the ratios involving LH are sensitive to duct location relative to the antenna. Ratios of the power coupled into the whistler-mode wave for various antenna polarizations do not change significantly between the short and half-wave dipoles. RH/D (D1 and D2 give identical power ratios) has at maximum a 1% deviation from the short dipole result, while NS/RH and NS/D show a maximum of 20% deviation. This corresponds to 1 dB or less, which is below the natural fluctuations in received signal intensity. LH/RH, LH/D, and LH/NS increase from zero with the short dipole to .008, .015, and .04, respectively, for the half-wave dipole. While the LH ratios show large percentage changes, the absolute changes remain small. Given the approximate nature of this model, the short dipole model is adequate for all but left-hand antenna polarization.

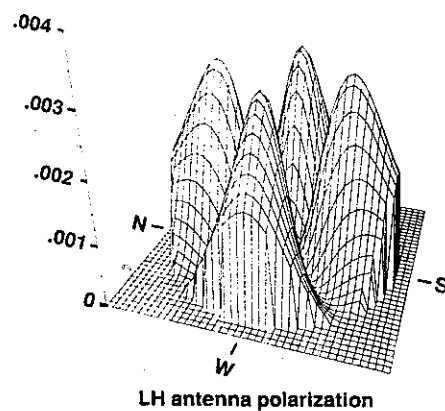
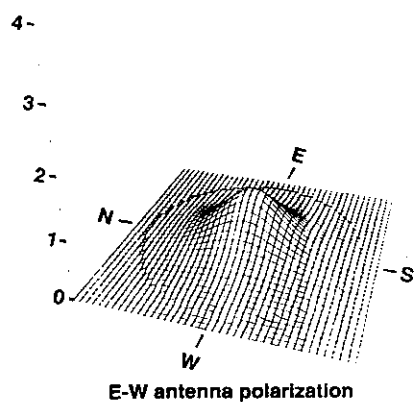
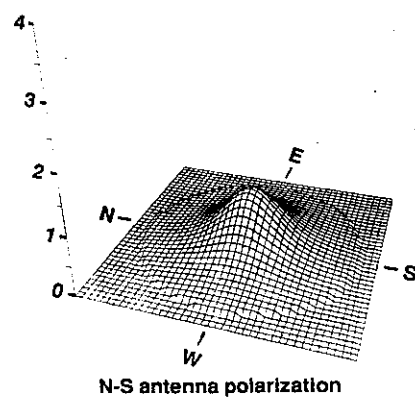
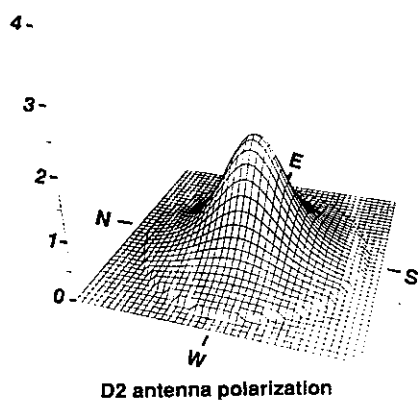
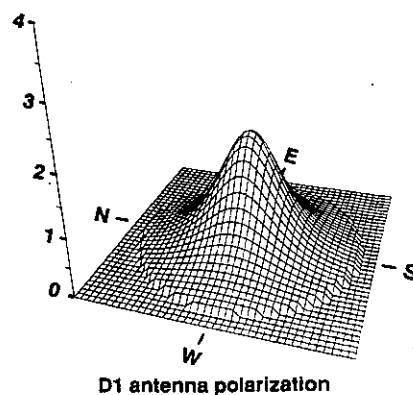
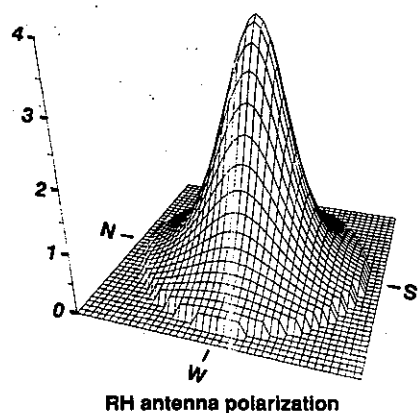


Figure 2.3. Plots of power coupled into the whistler mode at the air-ionosphere boundary (relative to the power coupled at the zenith from a single antenna) for various antenna polarizations. All plots are centered on Siple Station. Plots end at a zenith angle of  $60^\circ$  (corresponding to a 155-km radius for an ionospheric height of 90 km). Antennas are half wave dipoles. Note that coupling from LH antenna polarization is much weaker than coupling from other antenna polarizations and also exhibits distinct nulls. After [Mielke et. al., 1992].

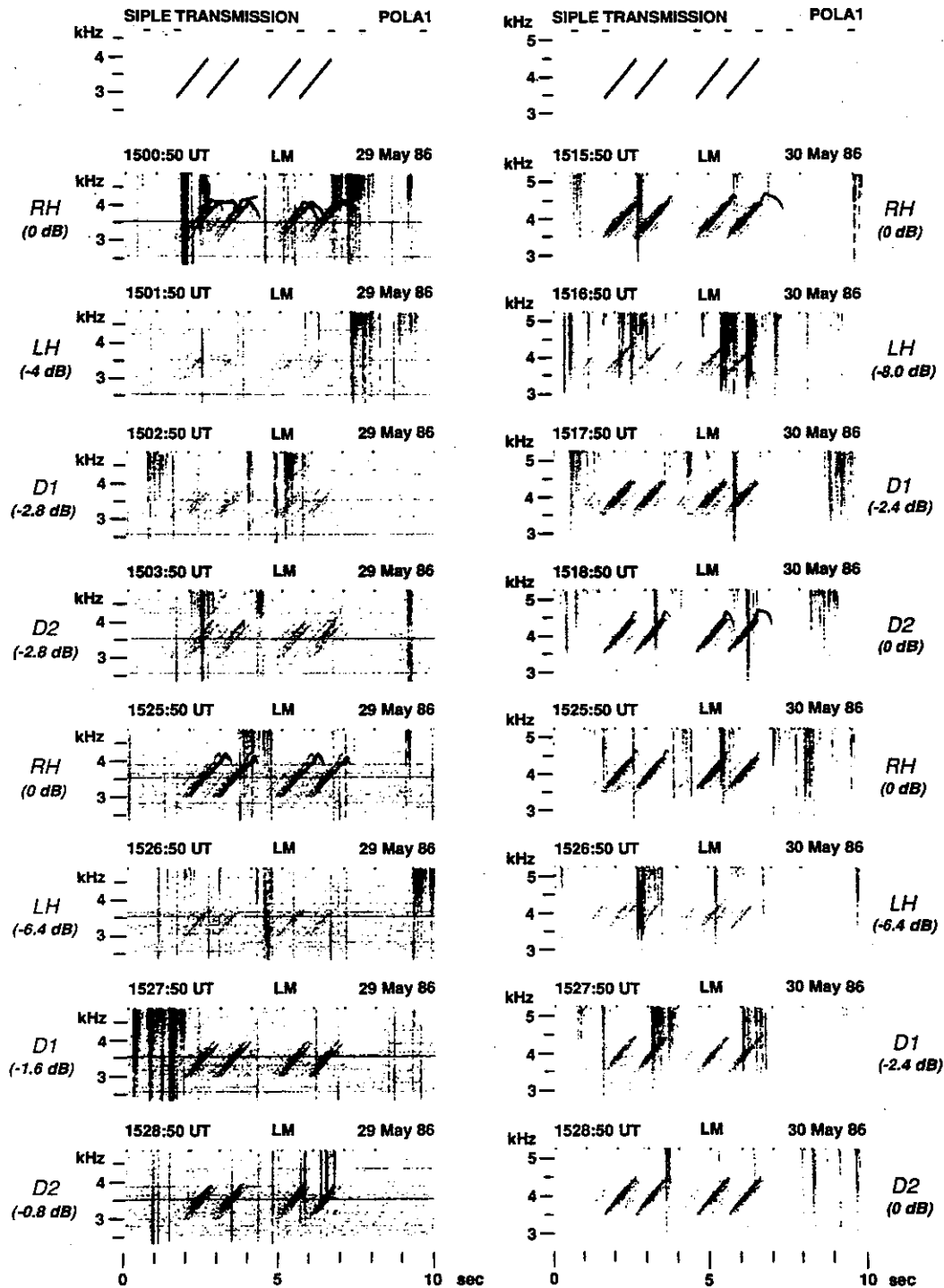


Figure 2.4. Polarization experiments with transmitted frequency ramps. Peak power at center frequency is shown in parentheses for various antenna polarizations. After [Mielke et. al., 1992].

In the case of left-hand antenna polarization the half-wave model shows that some whistler-mode waves can be excited but probably underestimates the strength of the excitation. Factors ignored in this model, such as ice reflections, rock reflections, near field effects, mode conversion in the ionosphere, etc., can all be expected to degrade the purity of the left-hand transmission and therefore increase the coupling into the whistler-mode wave.

#### D. OBSERVATIONS OF DUCTED SIGNALS WITH DISCRETE PATHS

Figure 2.4 displays spectrograms showing 1 kHz/s frequency ramps transmitted at Siple station and received at the conjugate station, Lake Mistissini. Four time periods are shown, two during May 29, 1986 and two during May 30, 1986. These spectrograms illustrate the predicted power relationships between differently polarized transmissions,  $RH > D2 \approx D1 > LH$ . The physical picture behind these power relationships is straightforward. The polarization ellipse of a plane wave from the antenna, when projected on the air-ionosphere boundary, will generally contain a component of RH circular polarization. It is this RH circular element which couples into the whistler mode. The RH circular component is maximum for a RH circular antenna polarization and minimum for a LH circular antenna polarization. Linear antenna polarizations D1 and D2 are intermediate cases. Note the repeatability throughout an hour and from day to day. The amplitudes given for each polarization represent the peak value of the strongest ramp at 3.477 kHz for May 29 and 3.96 kHz for May 30. A 100 Hz filter bandwidth was used in this measurement. These values should only be taken as a rough measure of the relative intensities between polarizations. Although D2 has the same peak value as RH for its strongest ramp, RH shows the strongest response and excites the largest number of paths. LH shows the weakest response and excites the smallest number of paths.

Modelling of coupling from the antenna into the ionosphere indicates that for fixed transmitter power, power ratios between different transmitter polarizations change with zenith angle and azimuth. If we know the location of the field-aligned ducts the signals travel in, we can determine zenith angle  $\theta$  and azimuth  $\phi$ , then predict the power ratios we should see between antenna polarizations. This provides a method for testing the model. However, we also need to consider attenuation from Siple to the duct entry point in the south and from the duct exit point in the north to Lake Mistissini. The procedure used to determine the location of the ducts was the following:

- 1) Determine the time delay of each 1 kHz/s ramp at a specific frequency (2.7 kHz in this case).
- 2) Compare this to the whistlers and their time delays at the same frequency. Then, by finding a whistler with the same time delay, identify the whistler corresponding to the specific path taken by the ramp.
- 3) Determine the nose frequency and nose time delay for this whistler and calculate the L-shell and equatorial electron density of the associated path [Ho and Bernard, 1973].

4) Once the L-shell is known, it can be mapped relative to Siple Station and the zenith angle and azimuth of the path end point can be estimated. Unless the L-shell indicates otherwise, the duct entrance point is assumed to be within 100 km of Siple Station [Carpenter, 1980].

An example of this procedure is illustrated in Figures 2.5, 2.6, and 2.7. Figure 2.5 displays a spectrogram showing the transmitted signal (1 kHz/s frequency ramp) along with a spectrogram and a chart of the amplitude in a 300 Hz band centered at 2.7 kHz for the signal received at Lake Mistissini. Due to multipath effects each signal transmitted at Siple Station gives rise to five signals at Lake Mistissini, designated P1 through P5. A spectrogram of a multipath whistler and its sferic as observed at Siple shortly after this transmission is also shown. The whistlers labelled WP1 through WP5 have delay times corresponding to ramps P1 through P5. L-shells and equatorial electron densities for these whistlers are indicated. It is necessary to obtain L-shells from the whistlers rather than from the frequency ramps due to the difficulty of making good dispersion measurements on the much narrower-band frequency ramps. Note that the path WP1 has a much smaller equatorial number density than any of the other whistler paths. This is presumably due to longitudinal variations in the L-value of the plasmopause. Such effects have been seen in previous whistler studies [Angerami and Carpenter, 1966].

In Figure 2.6 spectrograms showing the Siple transmitted signal, RH and LH polarized signals as received at Lake Mistissini, and charts of received amplitude in a 100 Hz band centered at 2.7 kHz are shown. For the RH polarized transmission four paths labelled 6P1 through 6P4 are evident at Lake Mistissini. Paths 6P1, 6P3, and 6P4 respectively correspond to paths P1, P2, and P5 of Figure 2.5. No whistler corresponding to path 6P2 was found. For the LH polarized transmission only paths 6P1 and 6P4 can be seen at Lake Mistissini. As all paths show evidence of growth and triggered emissions, and since the saturated power of a signal after magnetospheric growth is not dependent on input signal power [Helliwell et al, 1980], it is no surprise to see that the LH and RH powers received on paths 6P1 and 6P4 are similar. The magnetospheric growth which can be observed in this experiment corresponds to the "temporal growth" of [Helliwell et al, 1980] or the "nonlinear amplification" of [Dowden et al, 1978]. This magnetospheric growth exhibits a threshold effect, in which weak input signals produce no growth but stronger input signals result in growth to the saturated power level [Helliwell et al, 1980]. Thus on paths 6P2 and 6P3 the RH transmission was presumably above the threshold for growth while the LH transmission was not. As sketched in Figure 2.7, path 6P3 is on the 4.53 L-shell and is probably nearest to the symmetry axes at 45 degrees to the antenna, where the LH polarized transmission coupling to the ionosphere approaches zero. Paths 6P1 and 6P4 are on L-shells of 4.62 and 4.53 respectively, away from the LH nulls and within 100 km of Siple Station.

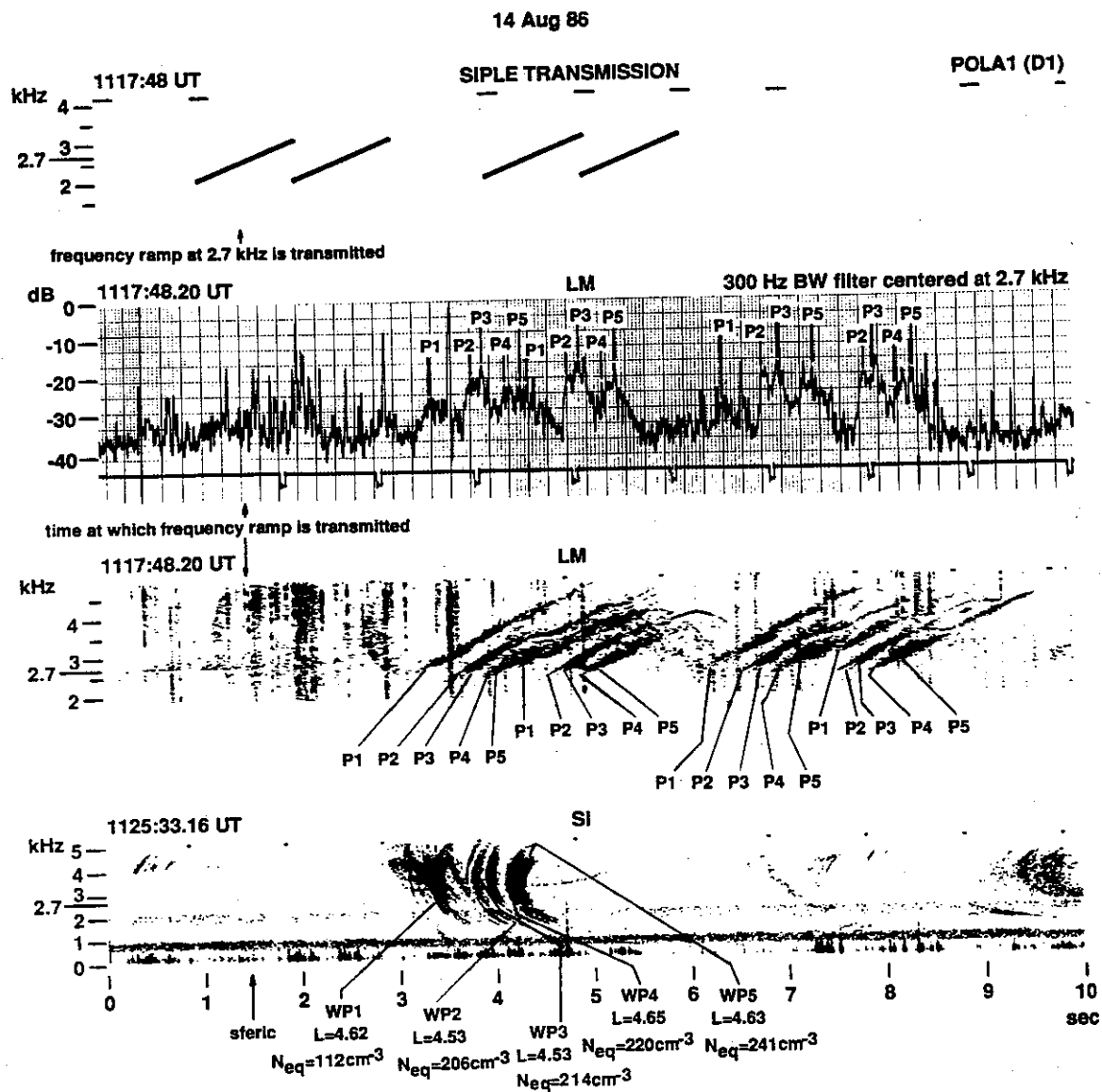


Figure 2.5. Propagation path observations for Siple signals and whistlers with identical time delays. After [Mielke et. al., 1992].

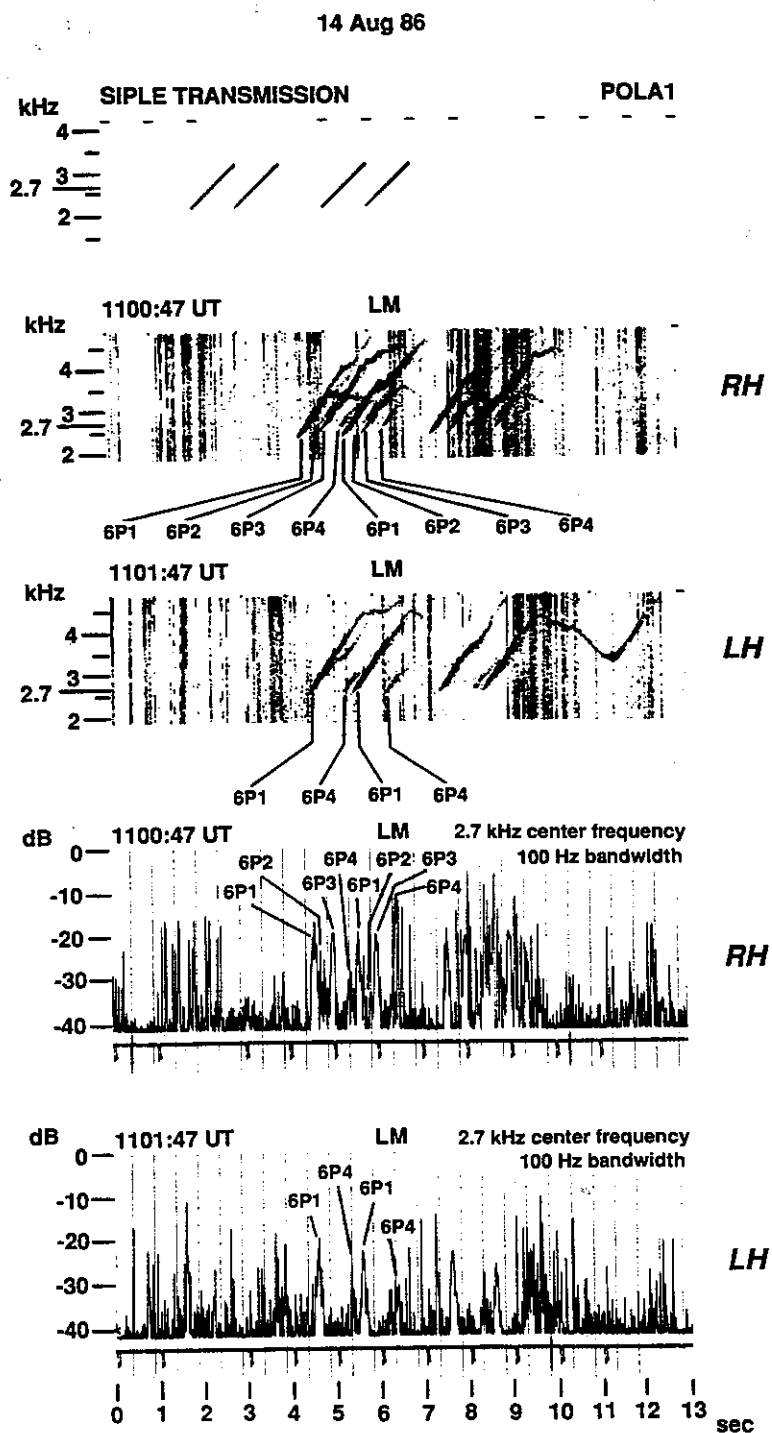
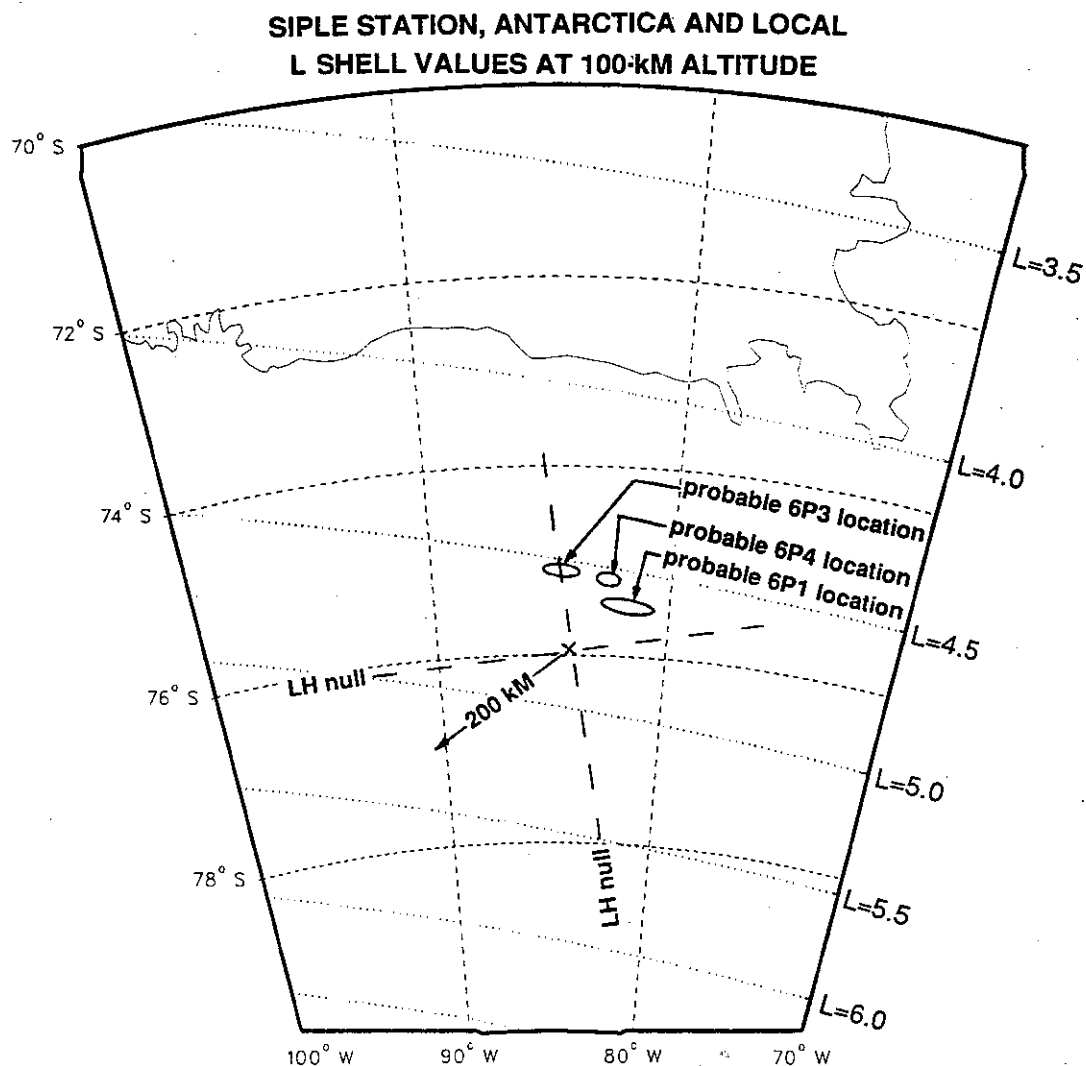


Figure 2.6. Path selectivity of polarized transmissions. After [Mielke et. al., 1992].



path 6P1 = path P1 = path WP1 (L=4.62)  
 path 6P3 = path P2 = path WP2 (L=4.53)  
 path 6P4 = path P3 = path WP3 (L=4.53)

RH on 6P1, 6P3, and 6P4  
 LH on 6P1 and 6P4

Figure 2.7. Estimation of path endpoint location. After [Mielke et. al., 1992].

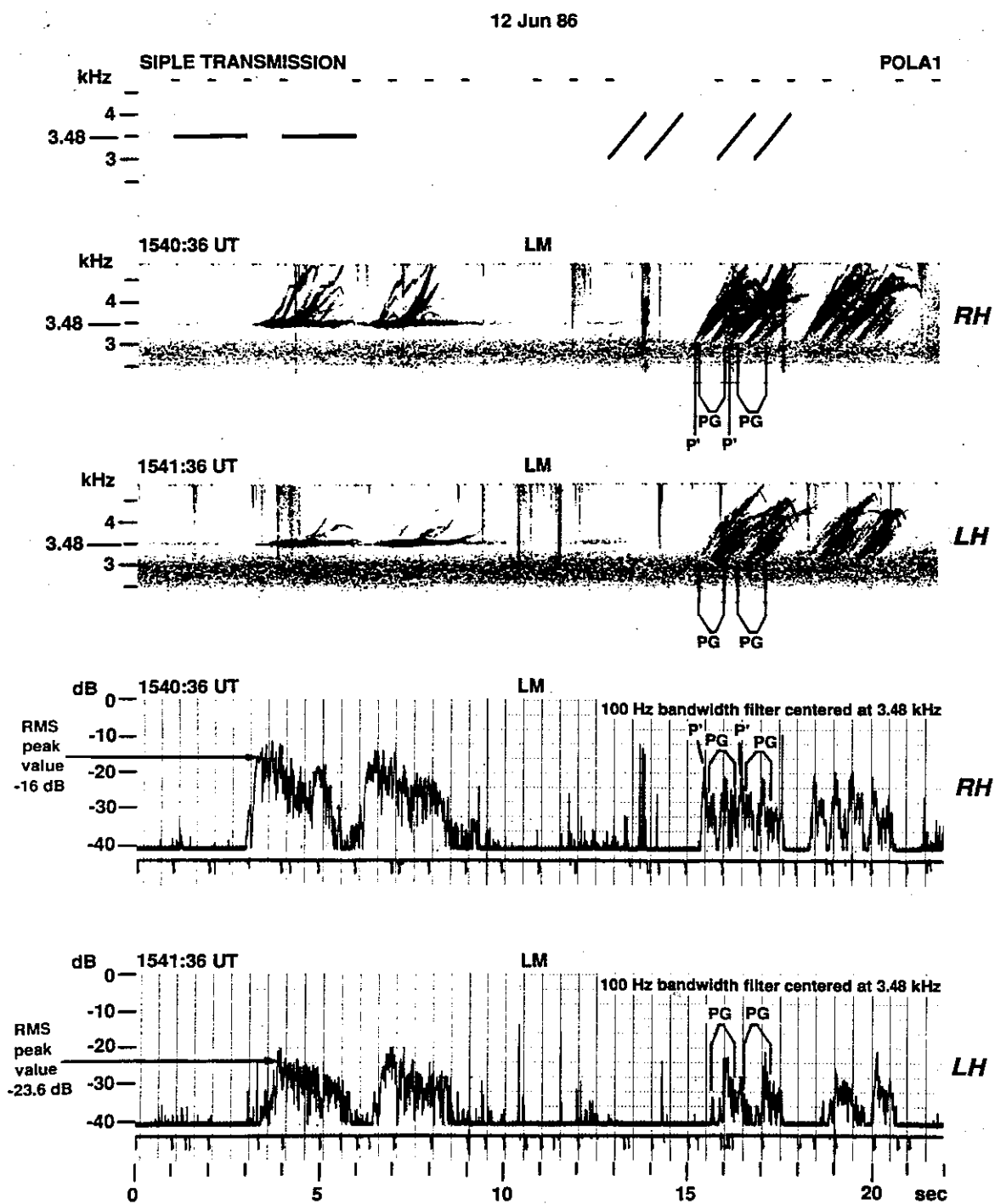


Figure 2.8. Multipath ducted signals. After [Mielke et. al., 1992].

22 Sep 86

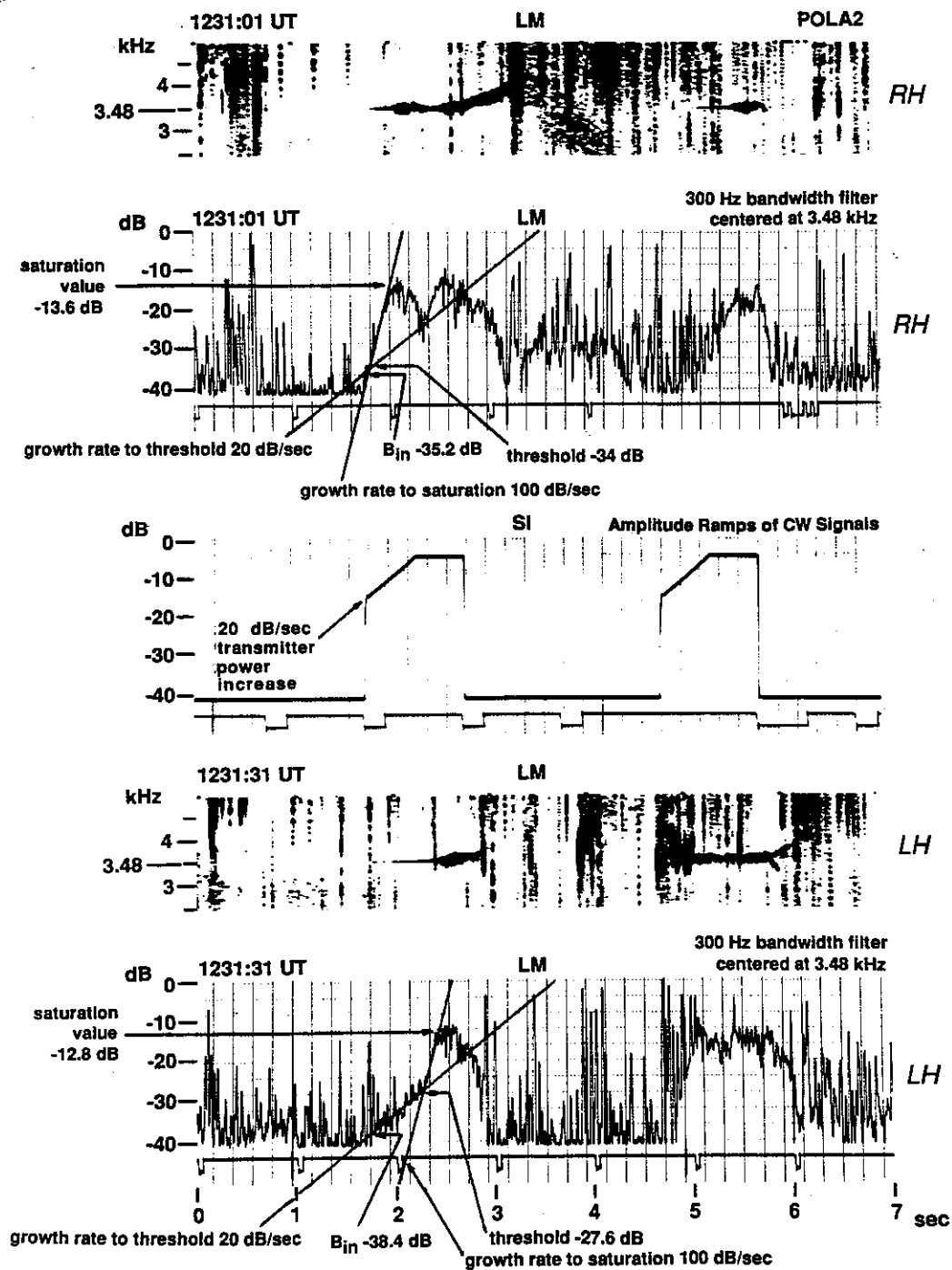


Figure 2.9. Magnetospheric growth of Siple signals. After [Mielke et. al., 1992].

### E. OBSERVATIONS OF DUCTED SIGNALS WITH MULTIPATH EFFECTS PRESENT

Multipath effects are also present on single frequency signals most of the time. One result of multipath is that the received pulse is longer than the transmitted pulse, and the received amplitude is the sum of several pulses with different amplitudes, time delays, and magnetospheric growth histories. Rarely can these components be disentangled. However, if the multipath effects are severe, with numerous paths contributing to the received signal, an estimate of the impact can be made as follows. Assume that the received signal is dominated by those paths on which the whistler-mode input signal is above the threshold for growth. On average, these paths will each produce similar saturated powers that add together in an incoherent manner at the receiver. If the ducts that give rise to these paths are both numerous and distributed more or less uniformly in the ionosphere above the transmitter, the number of ducts above threshold will depend on the ionospheric area in which strong coupling from the antenna to the whistler mode is present. The ratio of powers received from different transmitter polarizations of single frequency pulses thus depends on the areas that these polarizations illuminate above the threshold for growth rather than on the ratios of whistler-mode coupling at any particular duct. Unlike the single path cases of Figure 2.6 (where saturation effects can cause near equality of received signals with different transmitter polarizations despite lower magnetospheric input for one of them) this process preserves the hierarchy  $RH > D2 \approx D1 > LH$  (since given a fixed threshold for growth, the respectively weaker coupling into the whistler mode of these transmitter polarizations will excite respectively smaller ionospheric areas above that threshold).

Figure 2.8 shows an example of this multipath effect. The top spectrogram shows the Siple transmission to illustrate the format. A pulse consisting of a single frequency for one second, followed by a one-second doublet with 30 Hz separation is transmitted twice. This is followed by four 1 kHz/s frequency ramps, each one second long. Transmitter polarization is constant for the 22 second segments shown. Spectrograms and charts of amplitude in a 100 Hz band centered at 3.48 kHz are shown for RH and LH transmitter polarizations as received at Lake Mistissini. The peak RH amplitude is about 7.6 dB greater than the peak LH amplitude on the single frequency pulses. The cause can be seen on the frequency ramps, where P' labels a path excited only by RH transmissions and PG labels a group of paths excited by both RH and LH transmitter polarizations. Note that most of the ramps reach threshold, grow to saturation, and trigger emissions for the RH transmitter polarization while fewer of the LH transmitter polarization ramps show emissions. In a like manner on the constant frequency pulses the triggered emissions are more numerous and start nearer the leading edge on the RH transmitter polarization.

### F. OBSERVATIONS OF DUCTED SIGNALS WITH SINGLE PATH PROPAGATION

Figure 2.9 shows a rare instance of single path propagation for which magnetospheric growth

and triggered emissions occurred. The transmitter format in this case is a single frequency, amplitude modulated pulse. For the first half second the amplitude increases at the rate of 20 dB per second, after which the amplitude remains constant for the remaining half second. Each successive pulse is of a different transmitter polarization. Spectrograms and charts of amplitude in a 300 Hz bandwidth centered at 3.48 kHz for the signal received at Lake Mistissini are shown. An example of the transmitted signal is also provided. The pulse at 1231:03 UT was transmitted with RH polarization. Its initial amplitude was very close to the threshold for magnetospheric growth, so the signal's 20 dB/sec amplitude ramp is seen for only 50 msec. At this time the signal strength crosses the threshold and growth becomes independent of the signal input level; we see 100 dB/sec growth although the transmitted signal amplitude was increased at a rate of only 20 dB/sec. Once the saturation level is reached growth stops. Note that growth to saturation occurs twice and is also detectable on the spectrogram. A rising emission is triggered at pulse termination and continues for about one second.

The pulse at 1231:33 UT was transmitted with LH polarization. Note that the initial amplitude is 3.2 dB less than that of the RH transmitted signal. The growth rate to threshold is 20 dB/sec for almost the entire 0.5 sec. Once threshold is reached, though, the behaviour is the same as that for RH; i.e., 100 dB/sec growth until saturation is reached. Even the saturation levels agree. The threshold values on these two pulses are not the same even though the consistent time delays and single path propagation conditions of this data set indicate that they travelled in the same duct. The threshold level has been seen to change quickly with time [Helliwell et al, 1980], and a 7 dB change in 30 sec as seen here is not unreasonable. The threshold values between RH and LH transmitted signals only 3 sec apart were measured at -34.4 dB (RH, 1231:03 UT) versus -32.4 dB (LH, 1231:06 UT) and -34.4 dB (RH, 1231:15 UT) versus -33.6 dB (LH, 1231:19 UT). Given the difficulties in measuring these levels in the presence of atmospheric noise, they agree fairly well.

Results of similar measurements made for the period of 1231 - 1238 UT on 22 September 1986 are shown in Figure 2.10. Although temporal variation in the saturation level is 3 to 4 dB, the average difference between RH and LH values is only .33 dB when the signals are measured close enough together in time (3 seconds) to minimize the effects of temporal variations.

#### G. OBSERVATIONS OF NONDUCTED SIGNALS

Examples of observations of polarized Siple transmissions on the Dynamics Explorer-1 (DE-1) are shown in Figure 2.11. A thirty second segment consisting of a spectrogram of the Siple transmission (shifted by 2.5 seconds so as to line up with the satellite data), a spectrogram of the signal received on DE-1, and amplitude from a 300 Hz wide filter centered at 4.8 kHz demonstrates the increased coupling into the whistler-mode of RH versus LH transmitter polarizations.

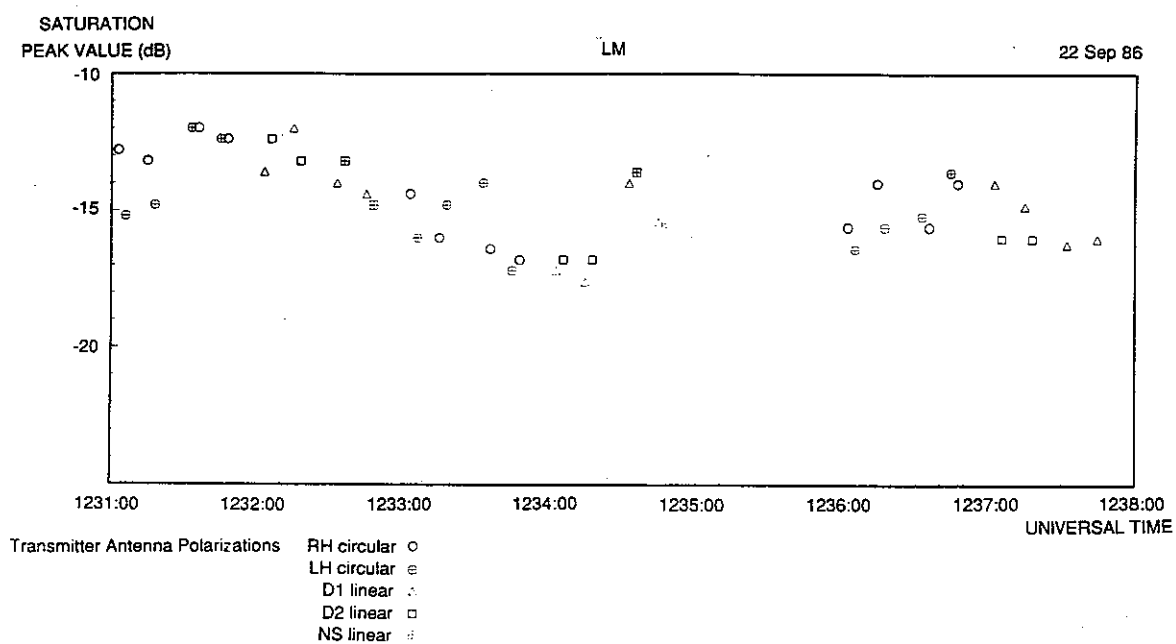


Figure 2.10. Saturated power on single-path propagation. After [Mielke et. al., 1992].

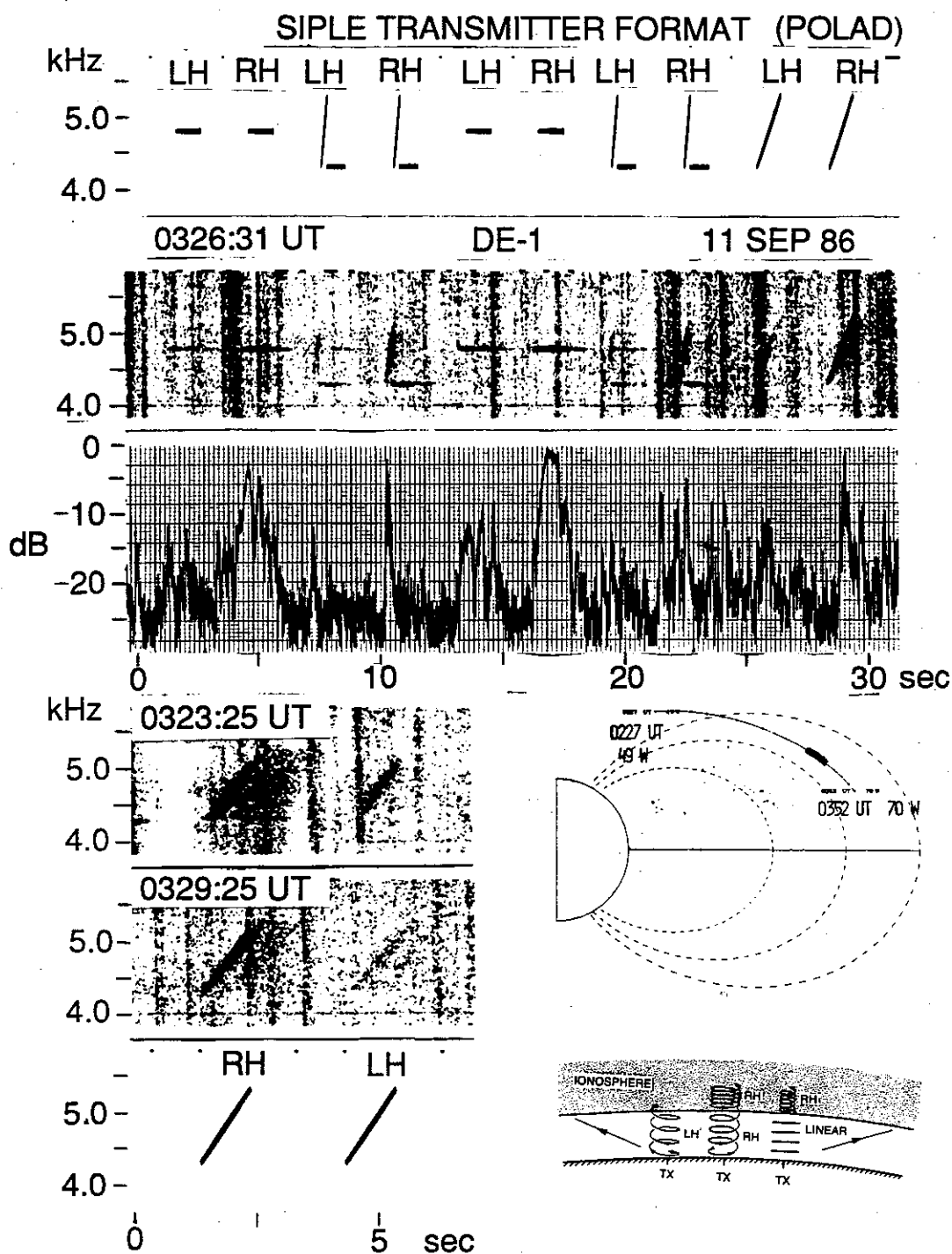


Figure 2.11. Satellite observation of nonducted Siple signals. After [Mielke et. al., 1992].

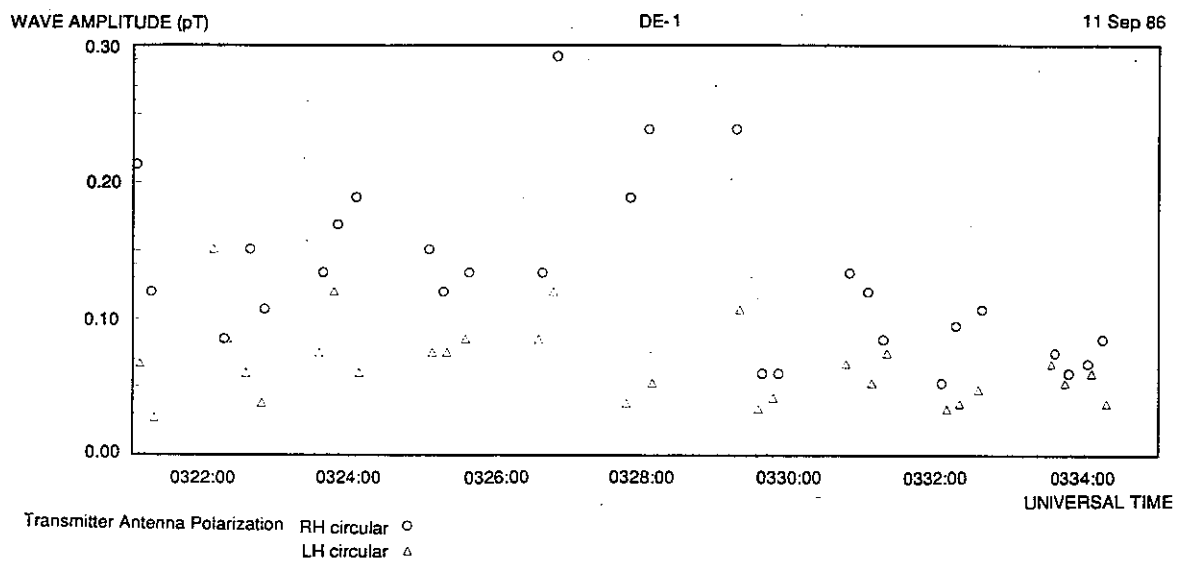


Figure 2.12. Wave amplitude observed on DE-1 satellite from the 112-kW Siple Station transmitter. After [Mielke et. al., 1992].

Note that the presence of impulsive noise requires some care in determining amplitudes of the Siple signal. Also shown are spectrograms of frequency ramps observed on DE-1 at 0323:25 UT and 0329:25 UT with an example of the ramps transmitted at Siple Station. Both multipath and temporal fading are apparent. A meridional plane projection of the DE-1 orbital position is also shown for reference. Measured wave amplitude (in picotesla) of the Siple signal as seen on DE-1 as a function of time is shown in Figure 2.12. These data were obtained with the magnetic loop antenna coupled to the linear wave receiver [Shawhan et al, 1981; Sonwalkar and Inan, 1986]. A 300 Hz filter centered at 4.8 kHz was used to process the wideband satellite recordings. Data were also taken with the electric antenna but reliable amplitudes could not be obtained due to spin fading (spin period = 6 s), causing gaps of up to a minute in the plotted results. At Siple station the power input to the antennas was 62 kW for the E-W leg and 50 kW for the N-S leg. As there is no evidence of magnetospheric growth on this data set, the variations in signal intensity are presumably due to a combination of temporal variations in ionospheric coupling along with multiple ray paths reaching the satellite [Sonwalkar et al, 1984]. The frequency ramps in Figure 2.11 show clear evidence of such multipath, and an orbit passing through regions of focusing and defocusing of ray paths should exhibit variations in signal intensity. Despite these complications, the RH transmitter polarization is always greater than or approximately equal to the LH transmitter polarization response. This agrees with the theory for whistler-mode excitation in the absence of magnetospheric growth.

#### H. SUMMARY AND DISCUSSION OF THE TRANSMITTER POLARIZATION EXPERIMENT

Experimental data from transmitter polarization experiments at Siple station are in general agreement with predictions based on classical magnetoionic theory. More accurate modelling of the coupling from transmitter to whistler-mode can, in conjunction with L-shell information, identify likely duct locations. Such efforts would involve taking advantage of the lobed structure of the LH transmitter coupling while using dispersion to identify the L-shell. Ionosonde and imaging riometer data would be required to produce a satisfactory model given the changeable nature of the ionosphere. The possibility of selectively exciting a single field-aligned duct is likewise of utility both for the study of the ducting process and in providing better data on the wave-particle interaction responsible for magnetospheric growth. Also, the whistler-mode power available using RH transmitter polarization is about twice that available from linear polarization, as shown in Figure 2.3. This increased whistler-mode power is of particular value in experiments aimed at artificial precipitation of energetic particles. The improved power achieved using RH polarization allows excitation of more paths above threshold providing possible motivation for using lower transmitter power into a crossed dipole antenna instead of higher transmitter power into a single dipole antenna.

### III. Siple Station Experiments on Wave-Particle Interactions with Linear Frequency "Chirps" and Frequency "Staircases"

Much of this material was reported in [Mielke and Helliwell, 1993], and is adapted here for summary and discussion.

#### A. BACKGROUND OF THE EXPERIMENT

Whistler-mode waves injected at Siple Station, Antarctica are often received at Roberval or Lake Mistissini, Quebec (near the north magnetic conjugate point) showing evidence of non-linear amplification [Carlson et al, 1985]. Such amplification is presumably due to interaction with energetic electrons in the magnetosphere. The process, sometimes called the coherent wave instability (CWI) [Helliwell et al, 1980, Carlson et al, 1990], is sketched in Figure 3.1. The detailed nature of this interaction is uncertain, but the data reported in this paper support previous suggestions that electron cyclotron resonance is the underlying mechanism. Earlier studies, assuming both cyclotron resonance and wave fields that are strong enough to cause particle trapping [Dysthe, 1971; Nunn, 1974; Dowden et al, 1978], were able to reproduce some of the features of the CWI. More recent work [Carlson et al, 1990] found wave amplification with cyclotron resonance even for signals much too weak to cause particle trapping. All of this previous work has been hampered by computing resources inadequate to fully simulate the wave-particle interaction, and by a paucity of in-situ data which could rigorously verify the consequent approximations. The experiment reported here was designed to test the cyclotron resonance hypothesis; it does not appear to provide any obvious test of the strong-vs-weak field controversy.

#### B. EXPERIMENTAL DATA

Data on the response of the magnetosphere to various rising frequency staircases are given in Figure 3.2 which shows dynamic spectra and amplitudes of both the Siple Station transmitter format and the signals as received at Lake Mistissini. The step durations were 1 ms (equivalent to a 1 kHz/s frequency ramp), 10 ms, 25 ms, 50 ms, and 100 ms. Despite interference from atmospherics, two important features in the received signal are apparent. First, the received signal shows exponential amplitude growth (approximately 30 dB/s growth rate) up to a saturation level (about 25 dB) despite a constant amplitude transmitted signal on the first three frequency staircases. Second, on the first two staircases a free-running emission (visible on the received spectra) is triggered at pulse termination. The last (and coarsest) two staircases show little evidence of either exponential growth or emissions. It might be noted that the 10 ms and 25 ms staircases show lower growth rates than the 1 ms staircase ( $\approx 25\text{dB/s}$  and  $\approx 15\text{dB/s}$  respectively, versus  $\approx 30\text{dB/s}$ ). This may be due to progressively weaker wave-particle interactions for progressively coarser approximations to a

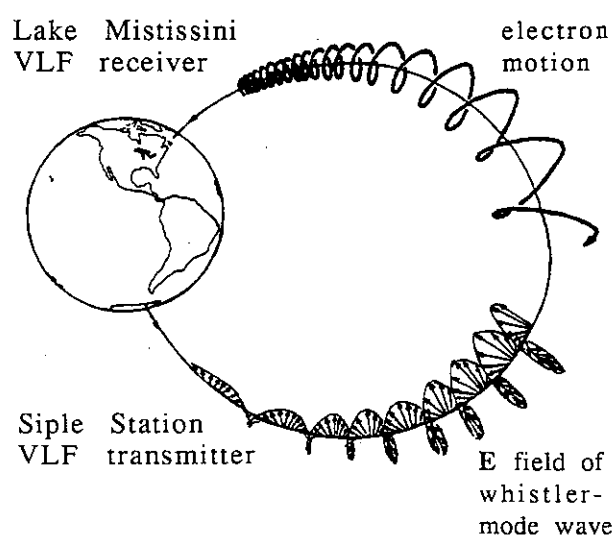


Figure 3.1. Whistler-mode wave and energetic electron. After [Mielke and Helliwell, 1993].

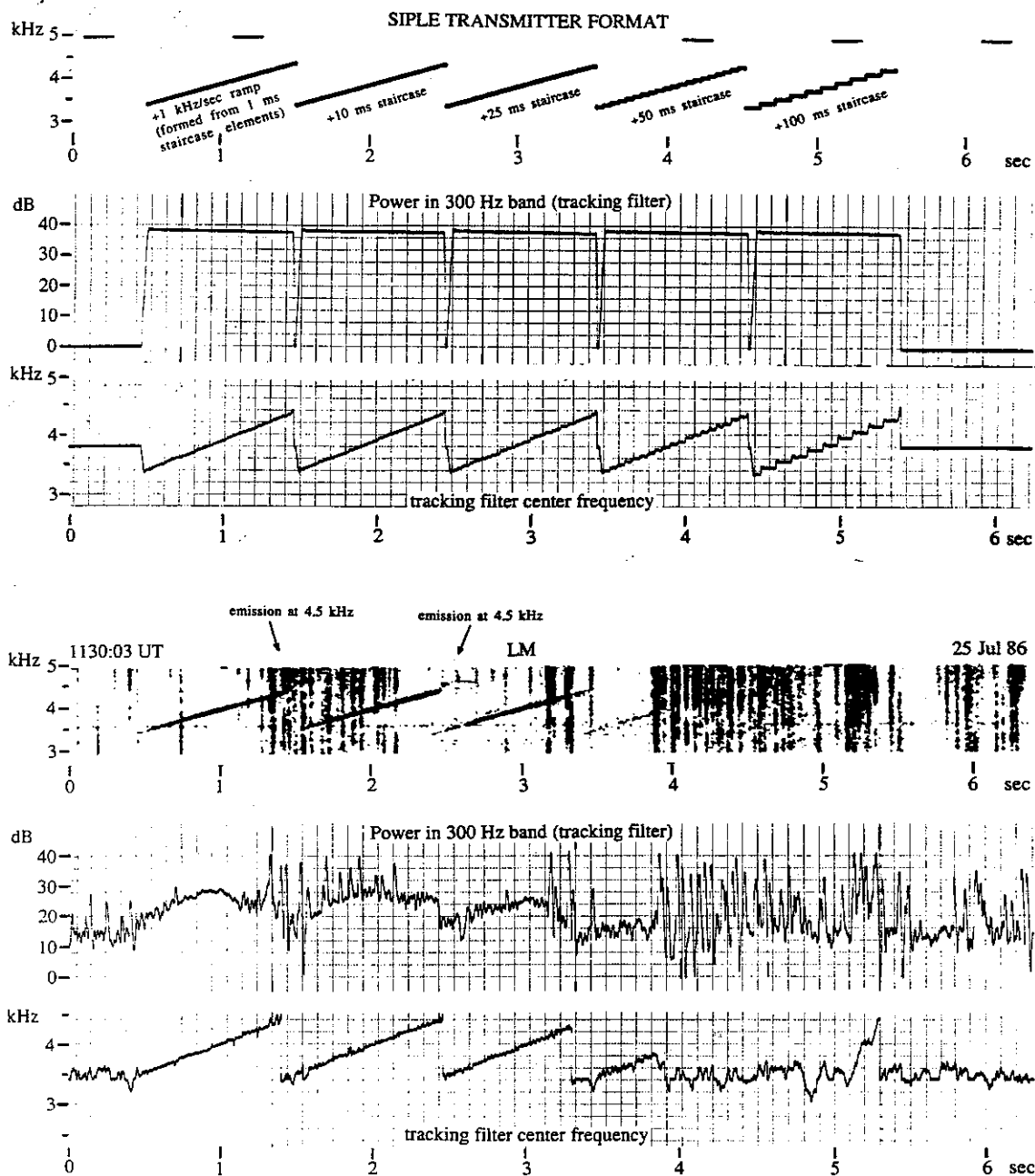


Figure 3.2. Rising frequency ramp, 10 ms and 25 ms rising frequency staircases show magnetospheric growth, but 50 ms staircase and 100 ms staircase do not. Note: on this and subsequent spectra the frequency resolution is 20 Hz, so only the 50 ms and 100 ms staircase steps are clearly resolved. The 200 ms constant frequency pulses at 5 kHz provide timing data. Spectral intensity is indicated by gray scale. For the power charts the tracking filter adjusts the center of the passband to follow the slowly varying carrier frequency. The spikes in the tracking filter output are caused by sferics. After [Mielke and Helliwell, 1993].

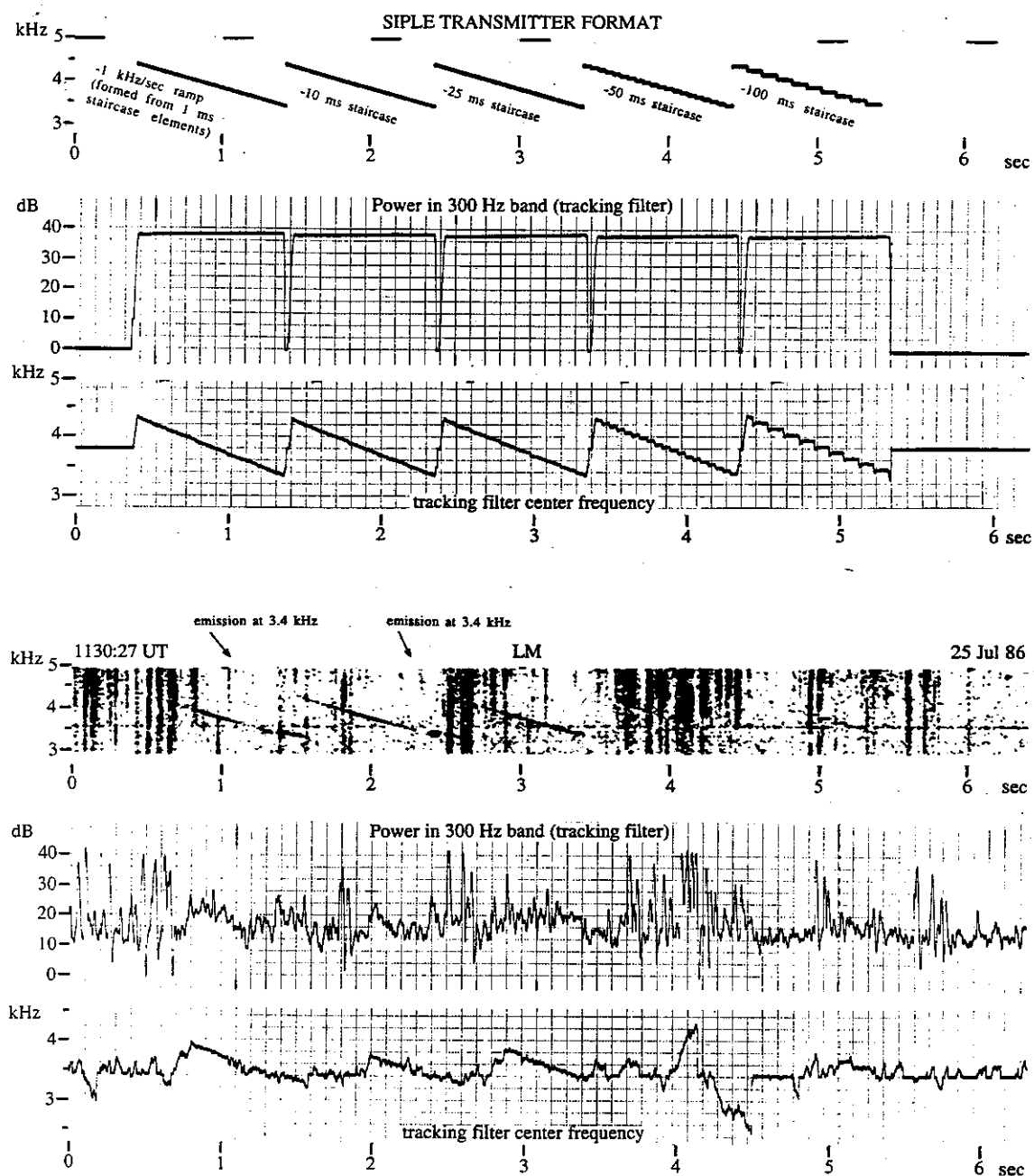


Figure 3.3. Falling frequency ramp, 10 ms and 25 ms falling frequency staircases show magnetospheric growth, but 50 ms staircase and 100 ms staircase do not. (100 ms staircase appears to act as a sequence of independent cw pulses. ) After [Mielke and Helliwell, 1993].

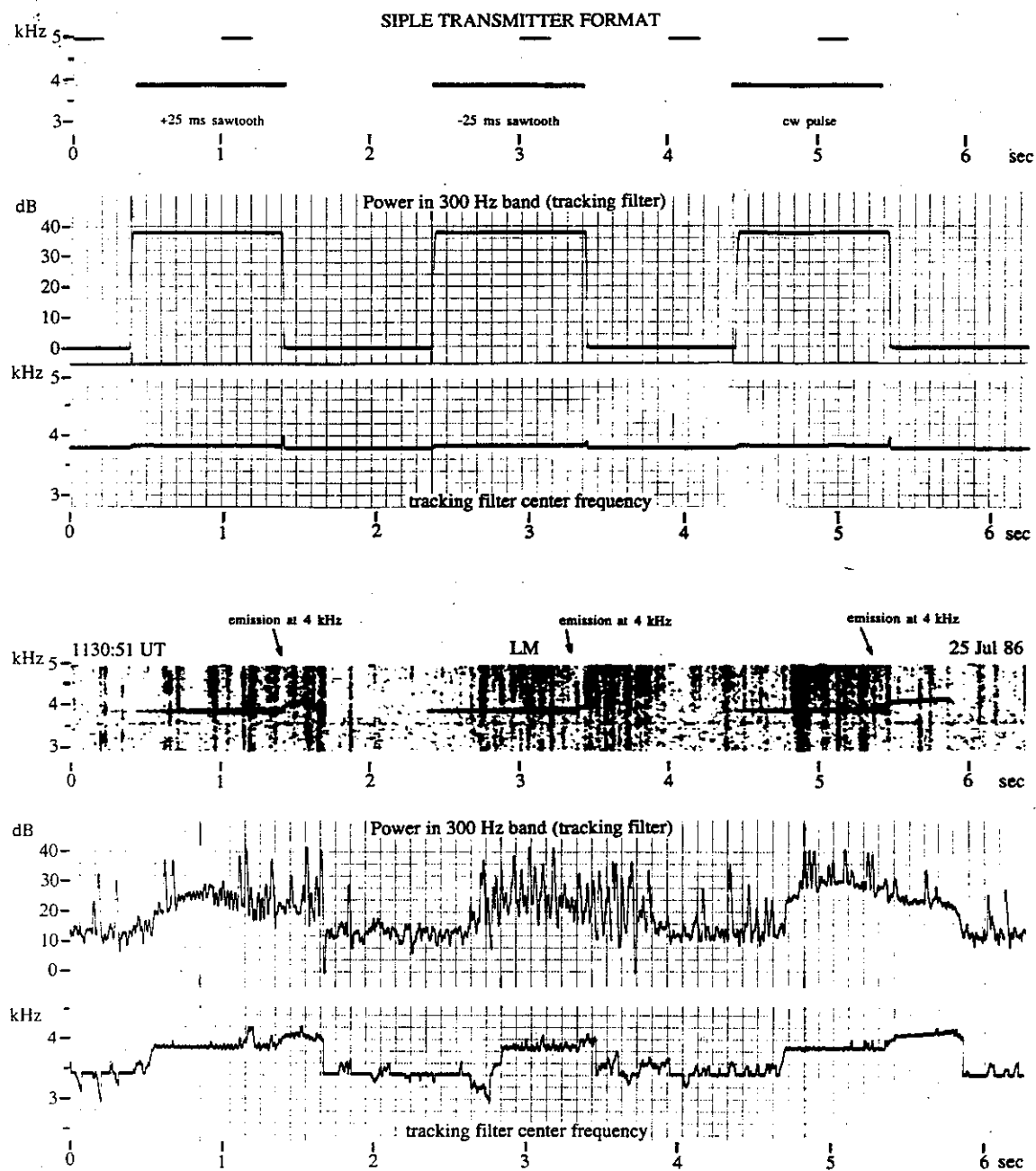


Figure 3.4. +25 ms sawtooth, -25 ms sawtooth, and cw pulse all show magnetospheric growth. After [Mielke and Helliwell, 1993].

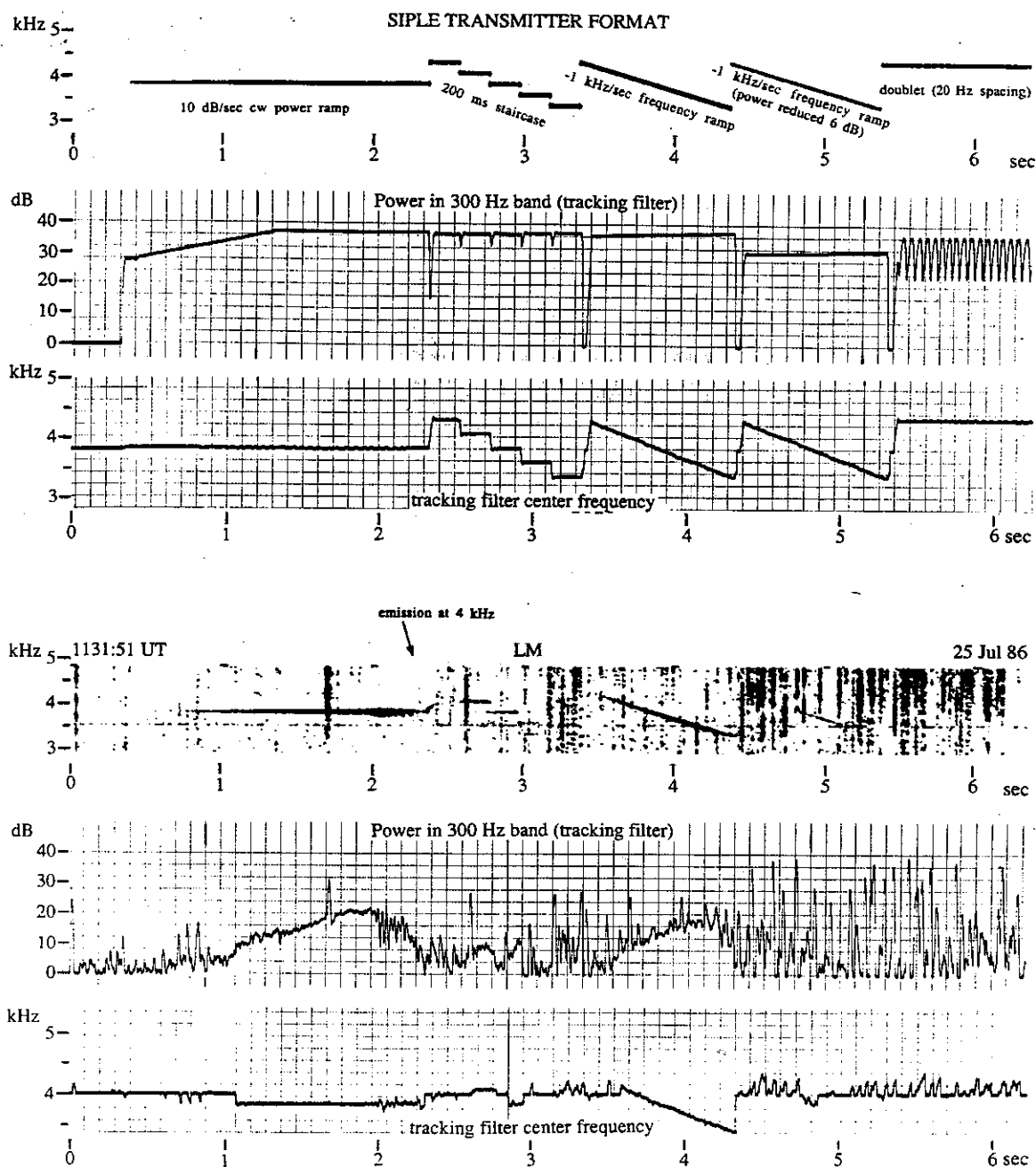


Figure 3.5. Example of the "dot-dash anomaly". The cw power ramp and the -1 kHz/s frequency ramp both grow and reach saturation. The reduced power frequency ramp is below threshold and does not grow. Only the second and third 200 ms steps in the frequency staircase can be identified. Both show growth but do not reach saturation. After [Mielke and Helliwell, 1993].

frequency ramp.

Figure 3.3 (falling frequency staircases) shows essentially the same behaviour as Figure 3.2. Growth and emissions are present on the first two staircases (1 ms and 10 ms step durations), growth, but no emissions, on the third staircase (25 ms step duration), and neither growth nor emissions on the last two (50 ms and 100 ms step durations), which are almost invisible in the spectra. Interference from sferics and emissions prevents determination of growth rates.

For step sizes greater than 50 ms a staircase appears to be too crude an approximation of a frequency ramp to exhibit the coherent wave instability. Comparison of Figures 3.2 and 3.3 shows that the major change from rising to falling frequency ramps is that saturated power is slightly reduced (about 20 dB versus 25 dB). Such moderate fluctuations in received power at Lake Mistissini are common and may relate to ionospheric absorption variations.

In Figure 3.4 (constant average frequency pulses) the rising and falling sawtooth pulses (made up of contiguous 25 ms long 1 kHz/s frequency ramps) show only slightly less growth (27 dB and 24 dB, respectively) than the constant frequency pulse (30 dB), while all show similar emission triggering. The fact that the sawtooth pulses are about as good an approximation to the constant frequency pulse as the 25 ms staircases are to the frequency ramps is consistent with the previous data.

Figure 3.5 shows a diagnostic sequence (for monitoring propagation and growth) transmitted 50 seconds after the coherence experiment. This example illustrates the effect of pulse length on growth, first observed on Morse code signals and called the "dot-dash anomaly" [Helliwell and Katsufakis, 1974; Helliwell et al, 1964]. The 2 s long constant frequency pulse shows growth and emission triggering, but the 200 ms long constant frequency pulses show no triggering and much less growth. While the 200 ms pulses are staggered in time so as to form a staircase, examination of the received spectra clearly shows each step is independent of adjacent steps.

### C. SECOND ORDER RESONANCE THEORY

It is commonly believed that wave growth comes about through interaction with energetic electrons in the magnetosphere. Both electron motion and whistler-mode waves in the magnetosphere have characteristic helical structures, sketched in Figure 3.1. The axis of the electron helix follows a magnetic field line of the earth, but that of the wave may deviate slightly. The pitch of the helix is a function of position on the magnetic field line. Where the pitch of wave and electron match, the electron sees a constant (rather than oscillating) electric field due to the wave, and at that location the strongest wave-particle interaction should occur. This condition corresponds to "first order resonance". As Figure 3.1 shows, the helix described by electron motion stretches along the axis as the electron approaches the equator. Conversely, the helix described by the whistler-mode

wave becomes compressed as the wave approaches the equator. Thus, the length of magnetic field line over which strong interaction occurs will depend on how rapidly the two helices diverge in pitch.

A measure of the length over which strong interaction takes place can be obtained from the "second order resonance" condition, the derivation of which is straightforward.

At location  $s_0$  on a magnetic field line of the earth, an electron moving along the field line with a velocity  $v_{\parallel}$  encounters a ducted whistler-mode wave at a frequency  $f$  and phase velocity  $v_p$ . In a reference frame moving along the field line at  $v_{\parallel}$  the electron executes a circular motion at the local gyrofrequency  $f_H$  while the electric field of the whistler-mode wave executes a circular motion at the Doppler-shifted wave frequency  $f' = f(1 + \frac{v_{\parallel}}{v_p})$ . With  $s$  being distance along the field line in the direction of  $v_{\parallel}$ , the gyrofrequency and Doppler-shifted wave frequency can each be expanded in a Taylor series:

$$f_H(s) = f_H|_{s_0} + \frac{df_H}{ds}|_{s_0}\Delta s + \frac{1}{2}\frac{d^2f_H}{ds^2}|_{s_0}\Delta s^2 + \dots$$

$$f'(s) = f'|_{s_0} + \frac{df'}{ds}|_{s_0}\Delta s + \frac{1}{2}\frac{d^2f'}{ds^2}|_{s_0}\Delta s^2 + \dots$$

For first order resonance the first terms of the two Taylor series are equal; for second order resonance the second terms of the two Taylor series are also equal.

The phase deviation over a distance  $\Delta s$  between the perpendicular velocity  $v_{\perp}$  of the resonant electron and the electric field of the wave can be expressed as:

$$\theta = \int_0^{\Delta s} \frac{2\pi}{v_{\parallel}} (f_H(s) - f'(s)) ds$$

When this phase deviation reaches  $\frac{\pi}{2}$  the coherent interaction between electron and wave is considered to end. Twice  $\Delta s$  is designated the "interaction length"  $l_i$  [Helliwell, 1967]. A short "interaction length" should lead to a weak interaction and a long "interaction length" to an extended and therefore strong interaction, all else being equal.

Another quantity of interest is the length of field line along which the electron encounters a wave pulse of duration  $\tau$ . This "encounter length" might be greater than or less than the "interaction length" depending on pulse duration. A short pulse, with a correspondingly short "encounter length", is expected to interact only weakly with the electron. Where  $v_g$  is the wave group velocity, this "encounter length"  $l_e$  [Mielke and Helliwell, 1993] is given by:

$$l_e = \frac{\tau}{\frac{1}{v_{\parallel}} + \frac{1}{v_g}}$$

If the transmitted pulse is a frequency staircase or sawtooth instead of a frequency ramp or constant frequency pulse, the instantaneous phase deviation  $\theta_i$  (relative to a resonant ramp or constant frequency pulse of the same average  $\frac{df}{dt}$ ) will depend on the step length. If  $\theta_i$  is small the staircase or sawtooth should behave like a slightly perturbed resonant pulse. The quantity  $\theta_i$  can be calculated from the expression for  $\theta$ , using the instantaneous rather than the average pulse frequency.

#### D. ANALYTIC FORMULAS

An analytical form for "second order resonance" and interaction lengths, , applicable at or very near the equator, was developed in the paper which introduced the "second order resonance" concept [Helliwell, 1967, 1970]. Numerical modelling has been used to examine some aspects of the theory (but not interaction lengths) over a wide range of electron pitch angles and magnetic latitudes at an L-shell of 4.5 [Carlson et al, 1985]. This section presents extended analytic results useful within about 10 degrees of the equator.

For a dipole field model and a non-relativistic electron [Roederer, 1970] [Helliwell, 1965], gyrofrequency  $f_H$ , equatorial gyrofrequency  $f_{H_{eq}}$ , equatorial plasma frequency  $f_{p_{eq}}$ , electron pitch angle  $\alpha$ , group velocity  $v_g$ , and phase velocity  $v_p$  (for a wave propagating parallel to  $B_0$ ) are given by:

$$f_H(\phi) = f_{H_{eq}} \frac{(4 - 3 \cos^2 \phi)^{1/2}}{\cos^6 \phi}$$

$$f_{H_{eq}} = \frac{873.6}{L^3} \text{ kHz}$$

$$f_{p_{eq}} = 8.9775 \sqrt{n_{eq}} \text{ kHz with electron density } n_{eq} \text{ in } \text{cm}^{-3}$$

$$v_p = c \frac{f_H}{f_p} \Lambda^{1/2} (1 - \Lambda)^{1/2}$$

$$v_g = 2c \frac{f_H}{f_p} \Lambda^{1/2} (1 - \Lambda)^{3/2}$$

$$\sin^2 \alpha = \frac{f_H}{f_{H_{eq}}} \sin^2 \alpha_{eq}$$

where  $\Lambda = f/f_H$  and  $\alpha_{eq}$  is the equatorial pitch angle.

Within about 10 degrees of the geomagnetic equator the plasma frequency  $f_p$  can be taken as constant [Park, 1972] and reasonably simple forms of the Taylor series can be obtained. The results presented here also assume that the wave frequency varies linearly with time. The value

of  $\frac{df}{dt}$  will vary with position along the propagation path due to dispersion, but the variation of frequency with time is assumed to remain linear. At  $L \approx 4.5$  and  $\frac{df}{dt} \approx 1 \text{ kHz/s}$  (the conditions of the STACO experiment) this is reasonable. For  $\frac{df}{dt} \geq 10 \text{ kHz/s}$  dispersion introduces significant curvature and a more complicated analysis is required. The formulas for  $\frac{df'}{ds}$  and  $\frac{d^2 f'}{ds^2}$  make use of the first order resonance condition  $f' = f_H$  to simplify the algebra but do not specify any other implicit relationship. With these caveats:

$$\frac{df_H}{ds} = -f_H \frac{3 \sin \phi (8 - 5 \cos^2 \phi)}{R_{eq} \cos \phi (4 - 3 \cos^2 \phi)}$$

$$\frac{d^2 f_H}{ds^2} = f_H \frac{3(3 + 36 \sin^2 \phi + 118 \sin^4 \phi + 75 \sin^6 \phi)}{R_{eq}^2 (1 + 3 \sin^2 \phi)^2}$$

with  $R_{eq} = L R_{earth} = L(6371 \text{ km})$

$$\frac{df'}{ds} = \frac{df}{dt} \frac{(1 + 2\Lambda)^2}{4v_p \Lambda (1 - \Lambda)} - \frac{df_H}{ds} \frac{1 + (1 - \Lambda) \tan^2 \alpha}{2}$$

$$\begin{aligned} \frac{d^2 f'}{ds^2} = & -\frac{d^2 f_H}{ds^2} \frac{1 + (1 - \Lambda) \tan^2 \alpha}{2} + \left(\frac{df_H}{ds}\right)^2 \frac{4 - [1 - (1 - \Lambda) \tan^2 \alpha]^2}{4f_H (1 - \Lambda)} \\ & - \frac{df_H}{ds} \frac{df}{dt} \frac{(1 + 2\Lambda)[3(1 + 2\Lambda) + 2(1 - \Lambda)^2 \tan^2 \alpha]}{8f_H v_p \Lambda (1 - \Lambda)^2} + \left(\frac{df}{dt}\right)^2 \frac{(1 + 2\Lambda)^2 (1 - 4\Lambda)}{16f_H v_p^2 \Lambda^2 (1 - \Lambda)^3} \end{aligned}$$

Dispersion will alter the slope of a transmitted frequency ramp. To calculate this effect, the group delay from Siple Station to the equator ( $\Delta t_{eq}$ ) [Bernard, 1973] is differentiated with respect to frequency. Within about 10 degrees of the equator propagation over an additional distance  $s$  from the equator introduces an additional group delay ( $\Delta t_s$ ) which is also differentiated with respect to frequency. The resulting slope changes are :

$$\frac{d(\Delta t_{eq})}{df} = \frac{t_n [(1 + \Lambda_n)(3\Lambda_n - f_n/f) - (3\Lambda_n - 1)(1 + \Lambda_n f/f_n)]}{8(f/f_n)^{1/2} f_n (1 - \Lambda_n f/f_n)^2}$$

where  $\Lambda_n = f_n/f_{H_{eq}}$  with  $f_n$  = nose frequency and  $t_n$  = nose delay

$$\frac{d(\Delta t_s)}{df} = \frac{f_{p_{eq}} R_{eq} \phi}{4c f^{3/2} f_{H_{eq}}^{1/2} (1 - f/f_{H_{eq}})^{5/2}} \left[ -1 + 4f/f_{H_{eq}} + \frac{3}{4} \phi^2 \frac{1 - 8f/f_{H_{eq}} - 8(f/f_{H_{eq}})^2}{1 - f/f_{H_{eq}}} \right]$$

The slope of a transmitted frequency ramp at a location  $s$  is then given by:

$$\frac{df}{dt} = \left[ \frac{d(\Delta t_{eq})}{df} + \frac{d(\Delta t_s)}{df} + \frac{1}{M_{TX}} \right]^{-1}$$

where  $M_{TX} = \frac{df}{dt}$  at the transmitter.

At a location  $s$  application of the second order resonance condition  $\frac{df'}{ds} = \frac{df_H}{ds}$  requires a choice of electron pitch angle  $\alpha$ . The second order resonance condition is not very sensitive to electron pitch angle for  $\alpha \leq 45^\circ$ . Accordingly, loss cone electrons were selected in order to minimize assumptions about the electron distribution function. The magnetosphere contains a diverse population of energetic particles. This leads to a theorem which might be phrased as "anything you want will be there". In this case, electrons slightly more energetic than the resonant electrons are expected to give up energy to the wave and provide growth while slightly less energetic electrons are expected to be accelerated by the wave and produce damping. Electrons far from resonance should interact only weakly with the wave and can be neglected. An unfortunate corollary to the above theorem might be stated "all the stuff you don't want will be there too"; thus as lower energy electrons are typically more numerous than higher energy electrons damping should be expected. A way out of this difficulty is to select resonant electrons at the loss cone, assumed to be empty. In that case for a given resonant  $v_{\parallel}$  only electrons with  $v_{\perp}$  greater than that of the resonant electrons will be present. Thus the resonant electrons are taken to have pitch angles given by [Roederer, 1970]:

$$\sin^2 \alpha_{eq} = \frac{1}{L^3 \sqrt{4 - 3/L}}$$

An alternative wave-particle interaction mechanism is possible between a co-streaming electron and the whistler-mode wave when the electron  $v_{\parallel}$  equals wave phase velocity  $v_p$  (Landau resonance) [Brice, 1960]. Here again the electron sees an essentially constant field and if a longitudinal wave E field exists (which is to be expected in a ducted as well as a non-ducted whistler-mode wave), a strong interaction can occur. As  $v_{\parallel}$  is greatest at the equator (a dipole field is assumed) while  $v_p$  is minimum there, such a co-streaming interaction can occur over only a limited region. By expressing both  $v_p$  and  $v_{\parallel}$  in Taylor series and matching terms in the respective series one can estimate the location and extent of the interaction region in a manner analogous to that used for the gyro resonance case. An important difference between the longitudinal and gyro resonance cases is that gyro resonance places far more stringent restrictions on wave coherence. The gyro resonant (counterstreaming) electron "sees" hundreds of cycles of the wave as it traverses its interaction region, and if wave coherence fails then the interaction is prematurely ended. In contrast, the Landau resonant (co-streaming) electron "sees" only a single point of the wave. The length of the interaction region can in fact be defined by those locations at which the electron has "slipped" relative to the wave by a quarter wavelength ( $\pm\lambda/4$ ). In the Landau resonance case therefore staircase step length and pulse length (for steps and pulses longer than one wavelength) are unimportant to the interaction. Since the "dot-dash anomaly" shows experimentally that pulse length is important in the coherent wave

instability, Landau resonance is presumably not the cause.

### E. COMPARISON OF DATA AND THEORY

The STACO format (a variety of constant frequency pulses, linear frequency ramps, frequency staircases and frequency sawtooth pulses) was transmitted from Siple Station, Antarctica and received at Lake Mistissini (near Roberval, Quebec) on 25 July 1986. It provides an excellent test of the first and second order resonance concepts. Measurements of frequency and time delay of the received signal [Ho and Bernard, 1973], combined with a diffusive equilibrium magnetospheric model [Park, 1972] yielded the propagation parameters  $L_{\text{shell}} = 4.5$  and  $n_{eq} = 530$  per cc. With these parameters and the transmitted signal characteristics ( $f = 3.8$  kHz and  $\frac{df}{dt} = +1$  kHz/sec,  $-1$  kHz/sec, or  $0$  kHz/sec) it was possible to determine the second-order resonance locations. Loss cone electrons were assumed. The centers of the regions of second-order resonance were located at the geomagnetic latitudes of  $-5.684$  degrees for the  $+1$  kHz/sec ramps,  $+6.005$  degrees for the  $-1$  kHz/sec ramps, and  $0$  degrees for the constant frequency pulses. Sketches of the pertinent variables, with the Landau resonance case included for comparison, are shown in Figure 3.6. Interaction lengths  $l_i$  were calculated to be about 900 km, while the encounter length  $l_e$  for a one second pulse was calculated to be about 5000 km. This prediction of strong interaction between coherent whistler-mode waves and energetic electrons fits with the growth and emissions seen on the frequency ramps and constant frequency pulse.

Encounter lengths were also calculated for the individual steps of the frequency staircases and sawtooth pulses. The greatest step encounter length was 460 km for the 100 ms staircase pulse (Figures 3.2, 3.3), considerably less than the interaction length. This suggests weak wave-particle interaction for a single isolated step even for the longest steps. In the data the 100 ms steps do not seem to be coupled to adjacent steps, and are also much weaker than the one second pulses.

For the 200 ms pulse in the diagnostic sequence (Figure 3.5) the encounter length is about equal to the interaction length. It would appear that an encounter length somewhat greater than the interaction length is required to produce growth to saturation and emission triggering. Based on extrapolation of the observed growth rate and on the saturated power level of the 2 s pulse, the required ratio of encounter length to interaction length is around  $2 - 3$ , corresponding in this instance to a 400 - 600 ms pulse length. These data are summarized in Table 1.

Examination of the instantaneous phase deviation of the 50 ms and greater staircase pulses gives a reason for the uncoupling of adjacent steps. The maximum instantaneous phase deviation was calculated for all frequency staircases and sawtooth pulses. For steps of 1, 10, 25, 50, and 100 ms the corresponding maximum  $\theta_i$  were  $0.0003\pi$ ,  $0.03\pi$ ,  $0.17\pi$ ,  $0.67\pi$ , and  $2.7\pi$  respectively. As these data show, maximum  $\theta_i$  exceeded  $\frac{\pi}{2}$  only for the 50 ms and 100 ms staircases.

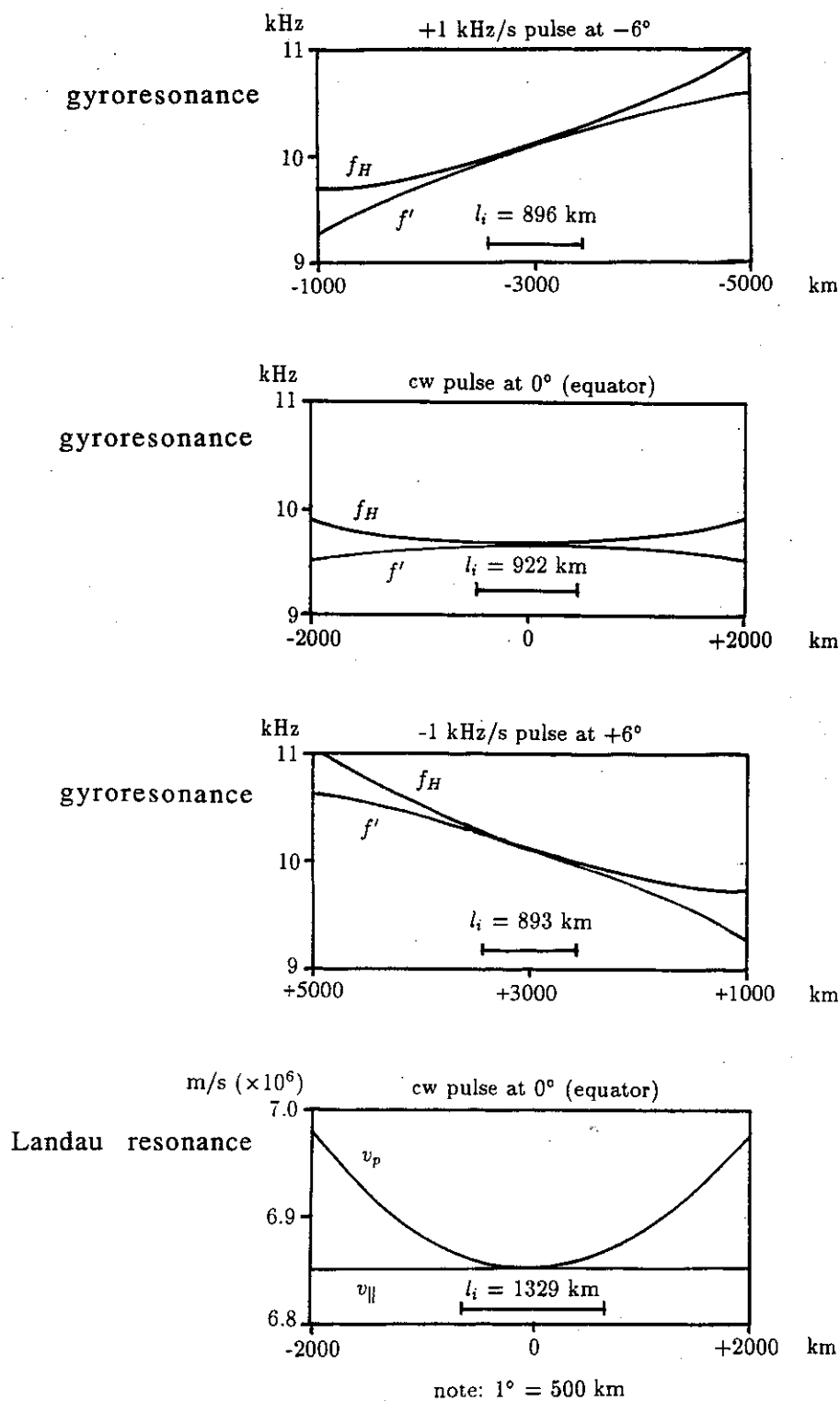


Figure 3.6. Gyroresonance conditions and resulting interaction lengths for the STACO frequency ramps and cw pulse. The Landau resonance case is also shown for the cw pulse; curves for the frequency ramps are not distinguishable from the cw Landau case by eye.

TABLE 1. Interaction lengths and encounter lengths for cw pulses.

Signal	interaction length $l_i$	encounter length $l_e$	$l_e/l_i$	Observations
2s cw power ramp	920km	9200km	9200/920 = 10	growth and triggering (figure 3.5)
1s cw pulse	920km	4600km	4600/920 = 5	growth and triggering (figure 3.4)
200ms cw pulse	920km	920km	920/920 = 1	growth, no triggering (figure 3.5)
100ms cw pulse	920km	460km	460/920 = 1/2	no apparent growth (figures 3.2, 3.3)
50ms cw pulse	920km	230km	230/920 = 1/4	no apparent growth (figures 3.2, 3.3)

TABLE 2. Phase deviations of frequency staircases relative to a resonant frequency ramp.

Signal	maximum instantaneous phase deviation $\theta_i$	$\theta_i/(\pi/2)$	Observations
1ms stair	$0.0003\pi = 0.05^\circ$	0.0006	growth and triggering (figures 3.2, 3.3, 3.5)
10ms stair	$0.03\pi = 5.4^\circ$	0.06	growth and triggering (figures 3.2, 3.3)
25ms stair	$0.17\pi = 30^\circ$	0.34	growth, no triggering (figures 3.2, 3.3)
50ms stair	$0.67\pi = 120^\circ$	1.34	no apparent growth (figures 3.2, 3.3)
100ms stair	$2.7\pi = 490^\circ$	5.4	no apparent growth (figures 3.2, 3.3)

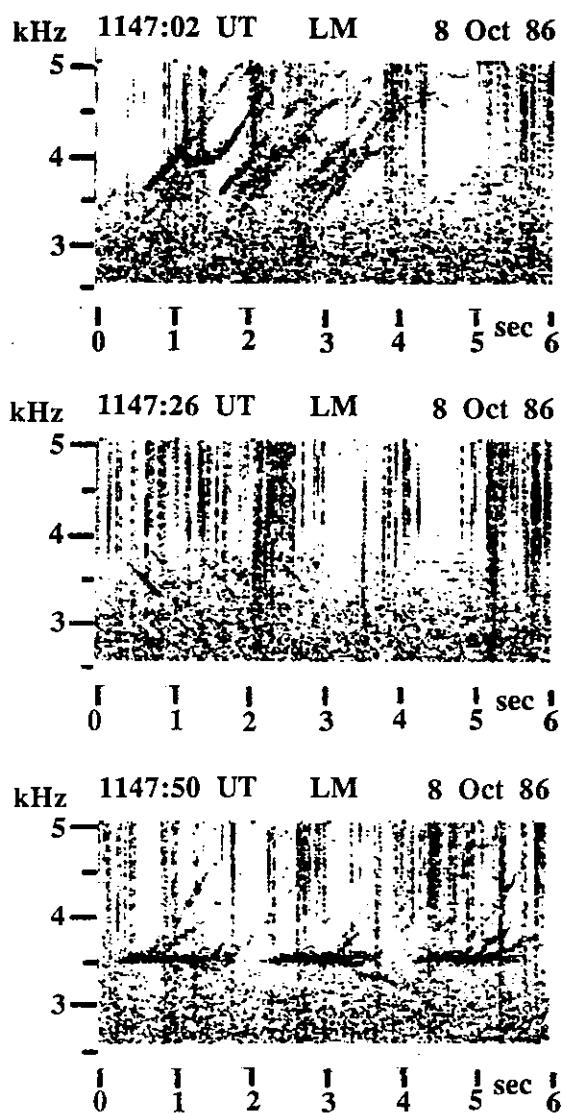


Figure 3.7. The rising frequency staircases (2.98 kHz to 3.98 kHz) with step durations less than 50 ms (upper panel, like those of Figure 2) show growth and emissions on at least three paths. The constant frequency pulses (3.48 kHz) and 25 ms-sawtooth pulses (lower panel, like those of Figure 4) also show growth and emissions on multiple paths (multipath causes the extension of the received pulse length). Falling frequency staircases (3.98 kHz to 2.98 kHz) (middle panel, like those of Figure 3) show less growth. After [Mielke and Helliwell, 1993].

These staircases are therefore expected to show weak interactions with energetic electrons, and indeed are much weaker than the other pulses when received at Lake Mistissini. These data are summarized in Table 2.

In the cases shown in Figures 3.2, 3.3, 3.4, and 3.5 (25 July 1986, 1130 - 1132 UT) the second order resonance theory explains why the rising frequency ramps, rising frequency staircases with modest step length, falling frequency ramps, falling frequency staircases with modest step length, sawtooth and constant frequency pulses transmitted from Siple Station all showed similar magnetospheric growth. It also explains why the coarser frequency staircases showed little magnetospheric growth. Frequently, however, behaviour such as that of Figure 3.7 (8 October 1986, 1147 - 1148 UT) is seen. Here the constant frequency pulses and rising frequency ramps show much stronger magnetospheric growth than the falling frequency ramps. Second order resonance theory predicts near symmetry for rising and falling frequency ramps. Reasons for the observed preferential magnetospheric growth of rising frequency ramps versus falling frequency ramps are not clear. Factors that may be important in this connection but are outside the scope of this paper, are the effect of the actual  $f(t)$  shape of the ramp in the interaction region and the variation of the temporal growth rate with frequency that could affect the relative overall growth of rising and falling ramps.

#### F. SUMMARY OF THE LINEAR FREQUENCY "CHIRP" EXPERIMENT

Experimental evidence supports identification of the electron cyclotron interaction as the underlying process for non-linear wave growth and emission triggering in the magnetosphere. Based on this wave-particle interaction, second order resonance theory predicts the observed relative growth of coarse versus fine frequency staircases. It also predicts the observed relative growth of short versus long constant frequency pulses ("dot-dash anomaly"). An additional feature of the experimental data is that rising frequency ramps often grow more than falling frequency ramps. A theoretical explanation of this preference for rising ramps is not yet available.

#### IV. Siple Station Experiments on Wave-Particle Experiments with Parabolic Frequency "Chirps"

Much of this material was reported in [Helliwell et al, 1990], and is adapted here for summary and discussion.

##### A. BACKGROUND OF THE EXPERIMENT

Magnetospheric whistler-mode signals originating in ground sources (e.g. lightning, VLF transmitters) often stimulate or trigger nonlinear responses in the form of amplified signals, narrowband variable frequency emissions and complex sidebands [Helliwell, 1988]. One such effect commonly associated with nose whistlers is the growth of the whistler in the upper part (above the 'nose') of its frequency range and the associated emission triggering that tends to occur at the whistler's upper cutoff frequency (usually at  $0.5 f_H$ , where  $f_H$  is the equatorial electron gyrofrequency) [Helliwell and Katsufakis, 1974]. An example of the dynamic spectrum of such an event is shown in Figure 4.1a where the growth of the whistler is represented by the darkening and broadening of the upper segment of the trace. The whistler triggered emission is, in essence, a narrowband oscillation of slowly-varying center frequency. What makes this phenomenon remarkable is the relatively short time ( $\sim 50$  ms) of growth ( $\sim 20$  dB) of the whistler compared with the time (200-400 ms) required for a monochromatic signal under comparable conditions to exhibit the same growth [Helliwell, 1988]. Since the triggered emissions associated with whistlers and constant frequency signals (such as those from VLF transmitters) are comparable in their intensities (as observed on the ground or on satellites) and spectral characteristics, one might expect the mechanisms of their generation to be the same. On the other hand, since the typical peak intensities of whistlers excited by lightning impulses are likely to exceed the signal level injected from ground-based transmitters that have been used in such experiments, one might simply attribute the observed difference in behavior to unknown nonlinear effects (none is suggested here) related to the high intensity of the input signals. In this paper, we describe a new experiment where the upper part (i.e. frequencies above the nose frequency [Helliwell, 1965]) of a one-hop nose whistler is simulated using the Siple Station experimental VLF transmitter [Helliwell, 1988] to reproduce two-hop nose whistlers that may exhibit the rapid growth described above (e.g. Figure 4.1a).

##### B. DESCRIPTION OF THE EXPERIMENT

For the experiment described herein a test wave form was designed by fitting the frequencies in a train of contiguous 1 ms segments (above the nose frequency) to a model of one-hop whistlers similar to those shown in Figure 4.1b. The resulting pulse was then injected from Siple Station as a simulated 1-hop whistler, which at Lake Mistissini resembles a 2-hop whistler.

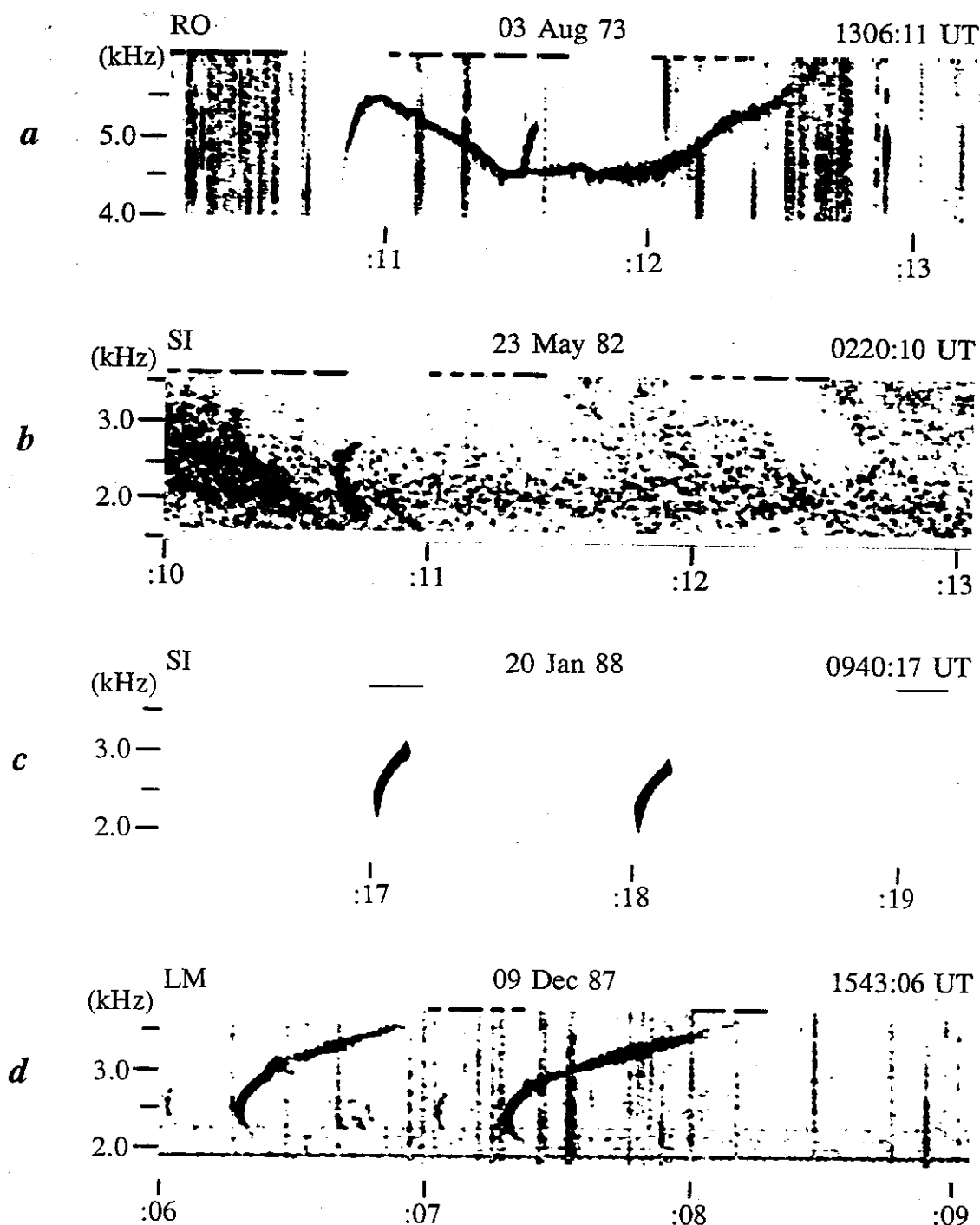


Figure 4.1. Natural and artificial nose whistlers. (a) two-hop whistler with triggered emission observed at Roberval, Canada; (b) one-hop whistlers observed at Siple Station, Antarctica; (c) NOWS (NOse Whistler Simulation) test waveform to simulate one-hop whistler; (d) growth and emissions observed on NOWS signals at Lake Mistissini, Canada. After [Helliwell et. al., 1990].

9 Dec 87

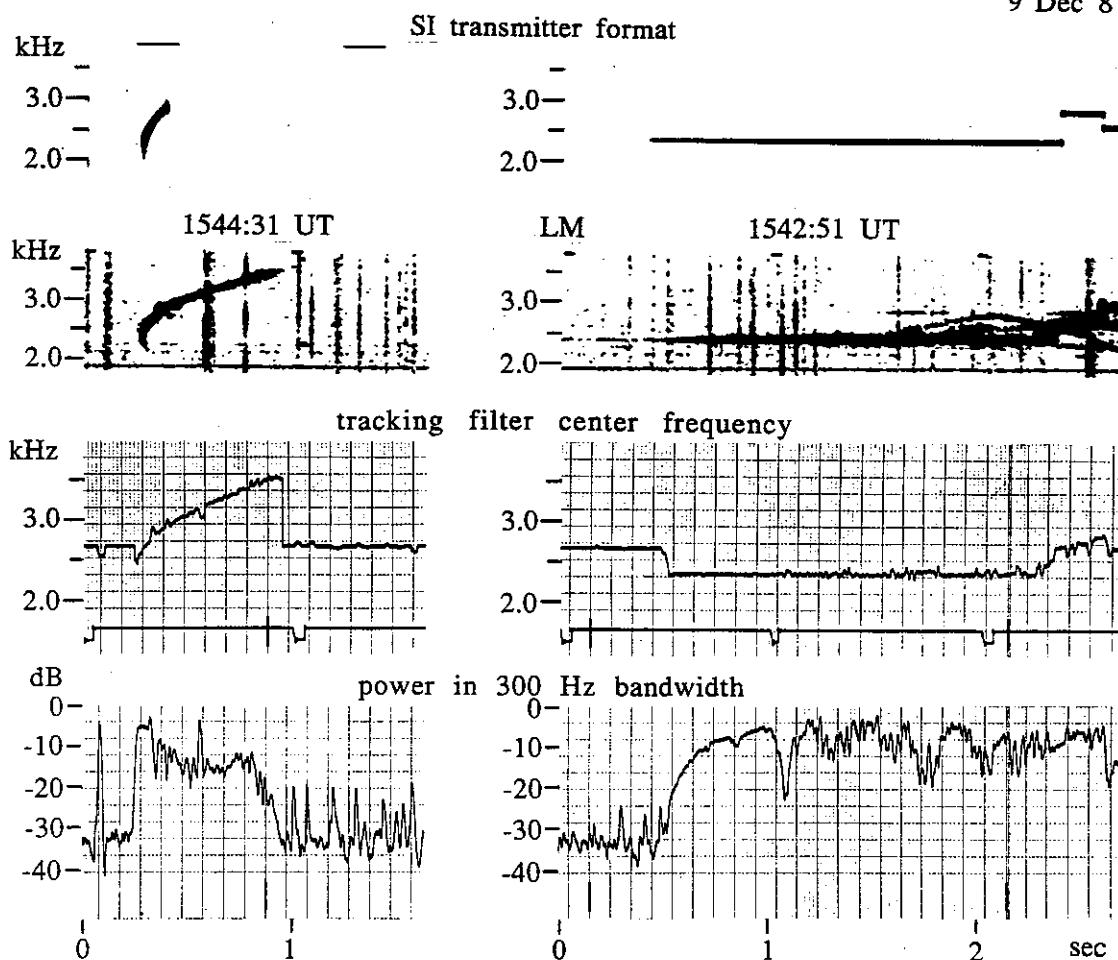


Figure 4.2. Simulated nose whistler (left hand column) and constant frequency pulse (right hand column). After [Helliwell et. al., 1990].

21 Jan 88

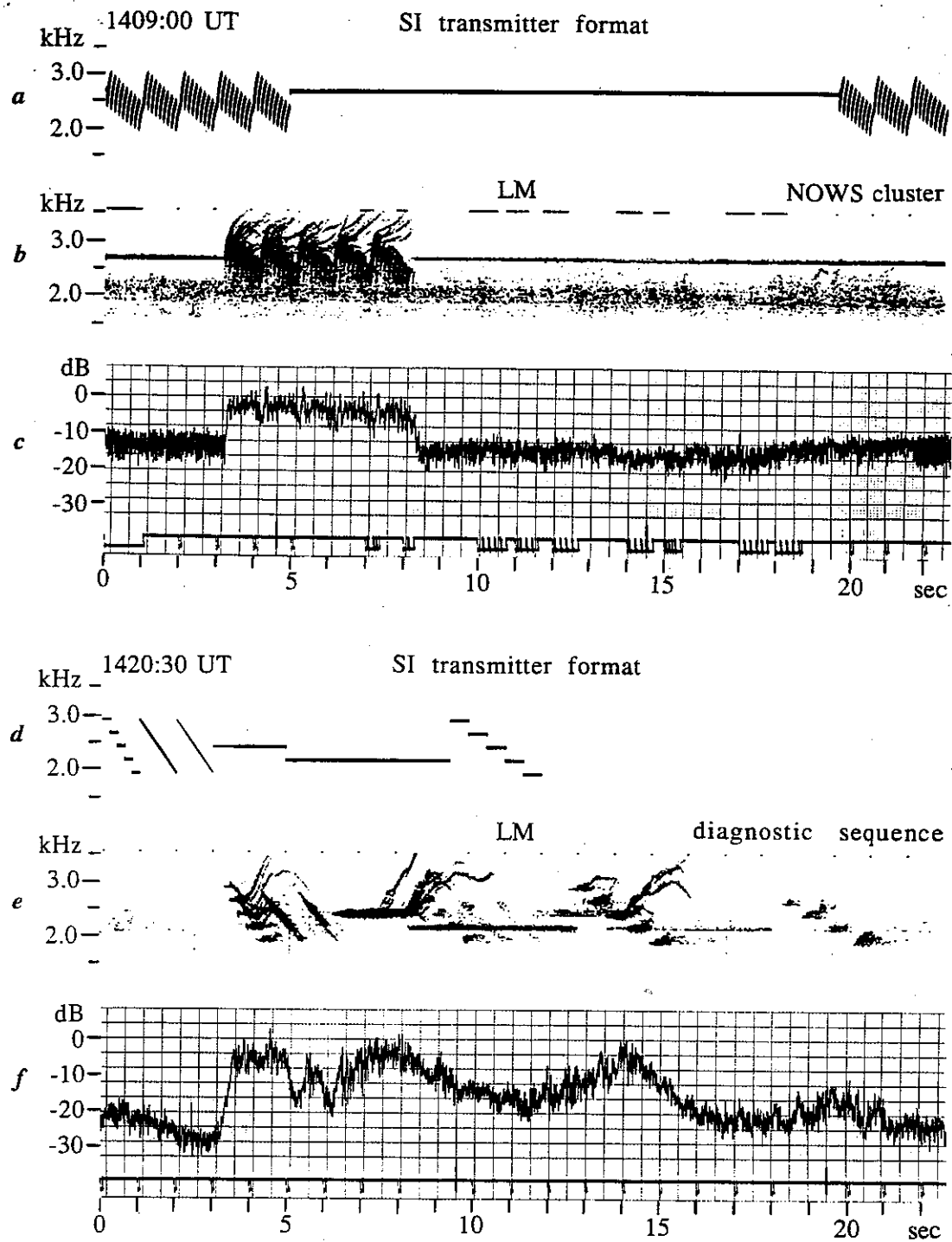


Figure 4.3. NOWS cluster and diagnostic sequence. Panels *c* and *f* show power in a 1 kHz bandwidth centered at 2.64 kHz. After [Helliwell et. al., 1990].

Thus in Figures 4.1c, and 4.1d, we see both growth and emission triggering stimulated by the nose whistler simulation (NOWS) which can therefore be said to have reproduced the principal features of amplified natural nose whistlers. A further demonstration of the enhanced growth rate of NOWS signals is shown in Figure 4.2 in which the spectra and amplitude profiles of the responses to a representative NOWS signal and a continuous wave (cw) signal of about the same input power are compared. Here we see that the saturation level is about the same (-5dB) for both signals, but the peak growth rates are  $\approx 1250$  dB/s for NOWS and 55dB/s (a typical value) for the CW reference signal. Thus the effective NOWS growth rate is  $\approx 20$  times the CW rate. It should be noted that the transmitted CW reference signal was ramped up in amplitude at a rate of 10 dB/s. This power ramp was intended to aid in measuring the threshold level below which temporal amplification does not occur [Helliwell *et al.*, 1980; Helliwell, 1988]. In this instance, the observed CW growth rate (55 dB/s) greatly exceeds 10dB/s from the start of the pulse, showing that the CW input signal power was always above the threshold for CW growth. Once the triggering threshold is reached the temporal growth rate tends to be independent of subsequent increases in the intensity of the input signal. Hence a correction for the 10 dB/s amplitude ramp is not required when measuring the temporal growth rate.

From the results illustrated in Figures 4.1 & 4.2, we conclude that a pulse of the appropriate  $f(t)$  curvature grows much faster than a CW signal at any frequency within the NOWS signal range. It is interesting therefore to pack NOWS pulses as close together in time as possible in order to enhance the averaged wave power output that would be associated with the higher growth rate of a NOWS pulse. The spectrum of such a composite signal, which we shall refer to as a 'NOWS cluster', is shown in Figure 4.3a, and consists of an unbroken sequence of similar NOWS pulses whose frequency ranges are decreased in steps of 16 Hz and where the center frequencies simultaneously are decreased in steps of 70 Hz. The signal spectrum as received at Lake Mistissini is shown in Figure 4.3b, along with its rms amplitude in Figure 4.3c (filter bandwidth=1 kHz). Each NOWS pulse shows growth followed by a triggered emission that tends to entrain the next emission, forming an irregular emission band at the upper border of the cluster. Such entrainment was seen in coarser form in earlier experiments [Helliwell and Katsufakis, 1978]. Several independent triggered emissions are also seen on each cluster, primarily on the first 4 or 5 NOWS pulses. Panels d, e, and f show the same type of data from a diagnostic signal sequence, consisting of stepped CW pulses and frequency ramps, a 2-sec amplitude ramp, and a frequency doublet (two equal amplitude carriers spaced 20 Hz apart). As can be seen by comparing the NOWS-cluster with the diagnostic sequence, the average NOWS level is about -4 dB, whereas the maximum level for the diagnostic pulses is about -8 dB, a gain of 4 dB for the NOWS format. The 1st element of the second cluster of NOWS pulses even

reaches 0 dB, suggesting that "fine tuning" of the NOWS format might produce nearly a factor of 10 increase in average signal power extracted from the magnetosphere compared with a CW input, thus enhancing particle precipitation.

The occurrence of NOWS growth and triggering has to date always been associated with CW pulse growth. For all recordings on which no CW pulse growth was seen, there were no traces of the NOWS format. In the present study the NOWS format was observed at Lake Mistissini on sixty-one occasions between 25 July 1986 and 20 January 1987 and between 30 November 1987 and 21 January 1988. The NOWS signal sequences were only detectable in 70% of the sixty cases in which the CW signal showed growth. In about 20% of those cases the artificial nose whistler was visible but showed no growth, while in 50% of the cases the artificial nose whistler was detected and showed growth. Thus the simulated nose whistler was about half as effective as a CW pulse in causing growth.

### C. INTERPRETATION

To explain the results reported above we invoke the concept of second order resonance [Helliwell, 1967, 1970; Carlson *et al.*, 1985], as developed in the previous chapter. Since the location of the second order resonance region depends on the local rate of change of the wave frequency ( $df/dt$ ) [Helliwell, 1970; Carlson, *et al.*, 1985], different parts of the NOWS wave train will exhibit second order resonance at different locations along the propagation path.

This situation is illustrated by the sketch in Figure 4.4, where the curved NOWS trace is approximated by three straight line segments each of which corresponds to second order resonance with electrons at the location shown. Each of these linear segments is amplified through feedback in much the same way as a CW wave is amplified on the equator [Helliwell, 1970; Helliwell and Inan, 1982]. However, because of the curvature of  $f(t)$ , a wave segment with a particular slope does not last long enough for the signal to reach saturation at that location. Instead growth occurs only while there is significant phase bunching. Thus each slope corresponds to extended resonance at a particular location, as shown in Figure 4.4 [Helliwell *et. al.*, 1990]. As each segment of the wave leaves its second order resonance region, the amplified output from that segment becomes the input of the next segment, giving rise to a kind of drifting feedback amplifier. The drift speed along  $\vec{B}_0$  increases with the curvature  $d^2f/dt^2$ . In terms of the resonant electrons, the length of the interaction region for a particular electron may be significantly reduced with respect to a CW signal on the equator. At the same time the *wave* interaction region is extended to a length defined by the distance along the field line between the second order resonances corresponding to the maximum and the minimum values of  $df/dt$ . Thus the resulting expansion along the  $z$  axis of the wave interaction region compensates in part for the reduced duration of the wave train.

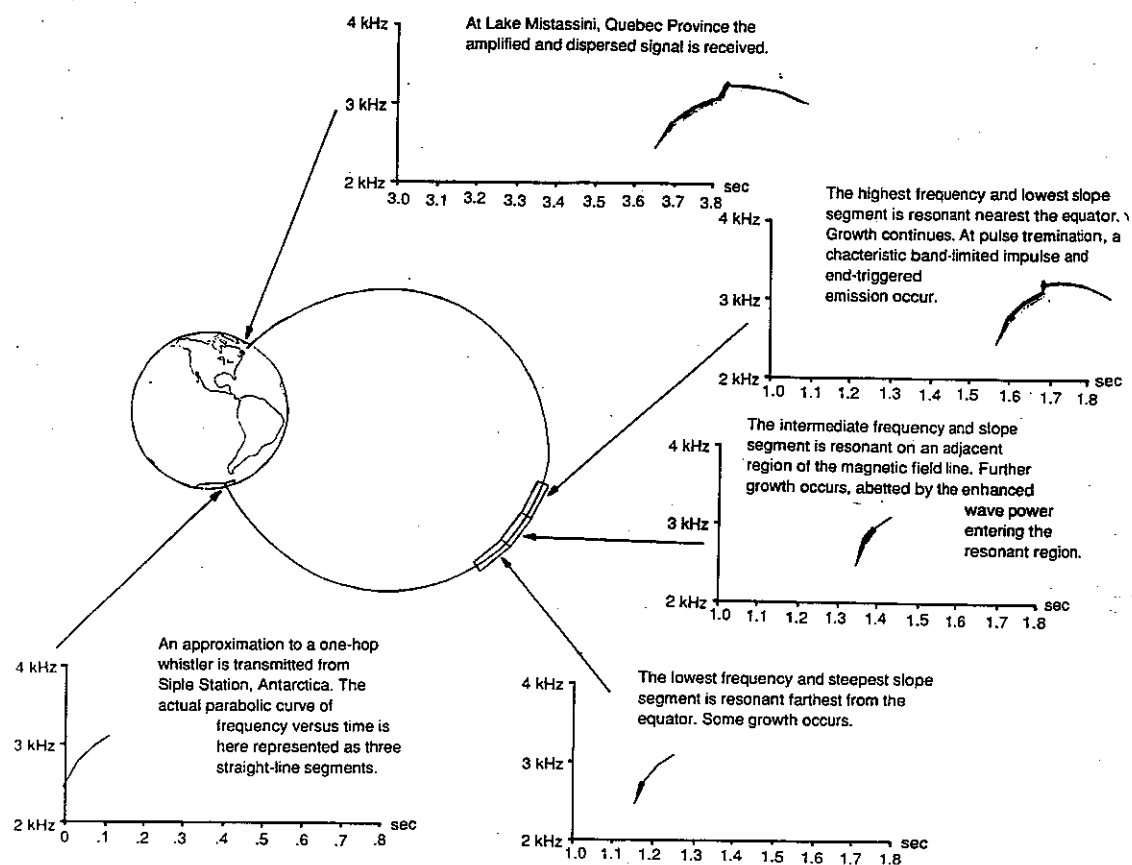


Figure 4.4. Schematic of the NOWS interaction. After [Helliwell et. al., 1990].

The result is a combination of convective and non-convective growth in which the actual time of growth may be much greater than the duration of the signal. We suggest that this process can account for the high apparent growth rates observed on natural as well as simulated nose whistlers.

Calculations using a model magnetosphere [Carlson *et al.*, 1985] and the NOWS trace of Figure 4.2 show that the second order resonance locus extends between  $z \approx 6600$  km and  $z \approx 29400$  km from the equator at  $L=4.5$ . Although the wave train is only 110 ms long, the time of propagation through this region is  $\approx 620$  ms, giving an effective average growth rate as measured in the frame of the traveling wave of only 45 dB/s.

#### D. DISCUSSION OF THE PARABOLIC FREQUENCY "CHIRP" EXPERIMENT

An important aspect of the second order resonance model described above is that growth is not limited to the region near the equator, but may occur anywhere along the field line as long as the necessary resonant electron distribution exists. Electron pitch angle scattering that results from the interactions would also be enhanced at locations far from the magnetic equator.

An alternative approach to the successive second order resonance model is a third order resonance model. In that case, developed in Appendix D, by matching second derivatives of Doppler-shifted wave frequency and gyrofrequency an extended interaction region can also occur. The two models are not equivalent; in the third order resonance model one group of electrons has a long interaction with the wave, while in the successive second order resonance model many different groups of electrons each have short interactions with the wave. Which model best fits the data is not yet clear. Either model will yield electron pitch angle scattering at locations far from the magnetic equator.

Since this model of the growth of NOWS signals is not limited to the equatorial regions it seems possible that significant growth and associated particle scattering may occur on open field lines extending out to the tail of the magnetosphere. Whistler waves of appropriate frequencies might even reach the earth's moon at times when it is in the tail of the magnetosphere. In that case some of the wave energy could be reflected from the moon's surface back along the same path, to be received at the Earth. Any discontinuities in refractive index, such as might be associated with magnetic field line reconnection, could also scatter energy back to the earth, perhaps of sufficient intensity to permit remote sensing from Earth of irregularities in the geomagnetic tail. We note, however, that because whistler-mode propagation cuts off for  $f > f_H$ , the sounding frequency must be less than  $f_H$  everywhere along the path. We estimate that the wave frequency required for such sounding would be of the order of 200 Hz, about an order of magnitude lower than the frequencies usually employed at Siple Station. Since lightning is known to excite whistlers at such frequencies (as deduced from low altitude satellite observations), it would be interesting to look for whistlers on

open field lines, using VLF receivers on future space missions that encounter the geomagnetic tail.

The NOWS experiment described here provides new support for the concept of second order resonance, which has been a central feature of explanations of the various manifestations of the coherent wave instability, underlining the importance of coherence between waves and particles for the growth of whistler-mode signals and the triggering of self-excited narrowband emissions. Enhanced wave-induced precipitation fluxes of energetic particles might also be expected due to the observed rapid growth and frequent triggering of emissions by NOWS clusters which increases the average wave energy (Figure 4.3). Thus we may expect that frequency-time curvature ( $d^2f/dt^2$ ) will play an important role in future controlled experiments on wave-particle interactions.

## V. Siple Station Experiments on the Threshold Effect in the Coherent Wave Instability

Much of this material was reported in [Mielke and Helliwell, 1992], and is adapted here for summary and discussion.

### A. BACKGROUND OF THE EXPERIMENT

The coherent wave instability (CWI), in which a ducted whistler-mode wave (which is frequency-coherent, of sufficient duration, and of sufficient intensity) shows exponential growth and triggers emissions [Helliwell et al, 1980] is presumed to result from interaction between energetic electrons and the coherent wave. The cause of the threshold effect, in which the wave intensity must exceed some threshold level before significant wave growth can occur, has not been established. Two suggested causes of the threshold effect are that (1) wave intensities sufficient to cause "trapping" of electrons are required to excite the CWI [Nunn, 1974; Bell, 1986; Molvig et al, 1988], and (2) ambient noise, such as unducted hiss (which is rarely seen on ground data), might disrupt the wave coherence and hence the CWI [Helliwell et al, 1980; Carlson et al, 1990]. The disruptive effect of random noise added to a ducted coherent signal is not expected to be very sensitive to the wave normal angle of the noise. The NETH (Noise Effect on THreshold) experiments conducted from Siple Station [Mielke and Helliwell, 1992] gave results consistent with the ambient noise hypothesis.

### B. DESCRIPTION OF THE EXPERIMENT

In the NETH experiment simulated VLF noise was superimposed on a variable amplitude constant frequency test signal. The constant frequency test signal (at 2.46 kHz in the example shown) was slowly ramped up in power at 10 dB/s for 4 seconds, then held constant (at maximum available transmitter power) for 1 second. Simulated noise was created by a constant amplitude carrier which was stepped in frequency every 10 ms [Helliwell et al, 1986b]. Each step was randomly selected from a table of frequencies that covered a 200 Hz range in steps of 0.1 Hz. This frequency range was chosen to include wave components up to the maximum  $\Delta f$  ( $\pm 100$  Hz relative to the cw pulse) at which growth suppression had been observed in two-frequency experiments [Helliwell, 1983; Helliwell et al, 1986a]. The bandwidth was limited in range in order to maximize the power spectral density from the peak-power limited transmitter. The composite signal (cw pulse plus simulated noise) was transmitted from Siple Station, Antarctica and (sometimes) received at Lake Mistissini, Quebec with magnetospheric growth and emissions present. Over a two minute period 10 such composite pulses were transmitted, with the simulated noise carrier amplitude "off", at -36dB, -30dB, -24dB, -18dB, "off", -12dB, -6dB, 0dB, and "off" relative to the maximum amplitude of the test signal. The noise "off" pulses were included to sample the CWI threshold and saturated power, which can vary on a time scale of seconds [Helliwell et al, 1980] so as to distinguish the effects of

artificial noise from temporal variations. Dynamic spectra of this experiment are shown in Figure 5.1. Suppression of the CWI by the simulated noise is clearly apparent. Out of 21 days between 25 Jul 1986 and 9 Dec 87 on which growth and emissions were seen on the test signal, suppression effects were visible on 13 days.

### C. DATA INTERPRETATION

While the suppression of growth and emissions by intense (0dB, -6dB, and -12dB) simulated noise, and the lack of suppression by weak (-36dB, -30dB) simulated noise is obvious in Figure 5.1, the precise determination of the level at which the simulated noise has no effect on growth and emissions posed some problems. A filter with adequate time resolution (100 Hz bandwidth, with a time resolution of 10 ms) includes much of the simulated noise, making identification of the threshold level (at which growth increases from the transmitted 10 dB/s to perhaps 40 dB/s) rather difficult. In addition, multipath (apparent in the multiple end-triggered falling tones in Figure 5.1) and natural variations in saturation and threshold levels further complicate the analysis. Examination of the "noise off" pulses led to the conclusion that perceptible variations in the threshold level were occurring on at least a 30 second time scale, and attempts to model the "background" threshold level via linear extrapolation between the "noise off" pulses did not yield useful results. Probably the multiple paths are fading independently of each other, producing variations that cannot be resolved with the available data. A rough measure of suppression was made by counting triggered emissions. This is roughly equivalent to measuring the energy in the received pulse, for the emissions tend to recur at regular intervals after saturation is reached, and so the number of emissions is proportional to the time that the pulse was above threshold. Likewise, the received energy (integral of the received power) may be approximated by time above threshold times saturated power (as saturated power may be 20dB above the threshold level), and so is proportional to the number of emissions. From Figure 5.2, showing the number of emissions versus the simulated noise intensity, we estimate -15 dB as the point where simulated noise ceases to affect the CWI threshold.

Presumably, if the CWI threshold is determined by the ambient noise level, the point at which the simulated noise ceases to affect the threshold is the point at which the intensity of the simulated noise is close to that of the natural background noise. Figure 5.3 shows natural noise observed near the expected CWI interaction region (near the equatorial plane, within 15 degrees of the Siple meridian, at L-shells from 3.9 to 4.4) on the DE-1 satellite. No simultaneous ground NETH data and DE-1 satellite data near the interaction region have been found, but the observed natural noise level and estimated simulated noise level can still be compared.

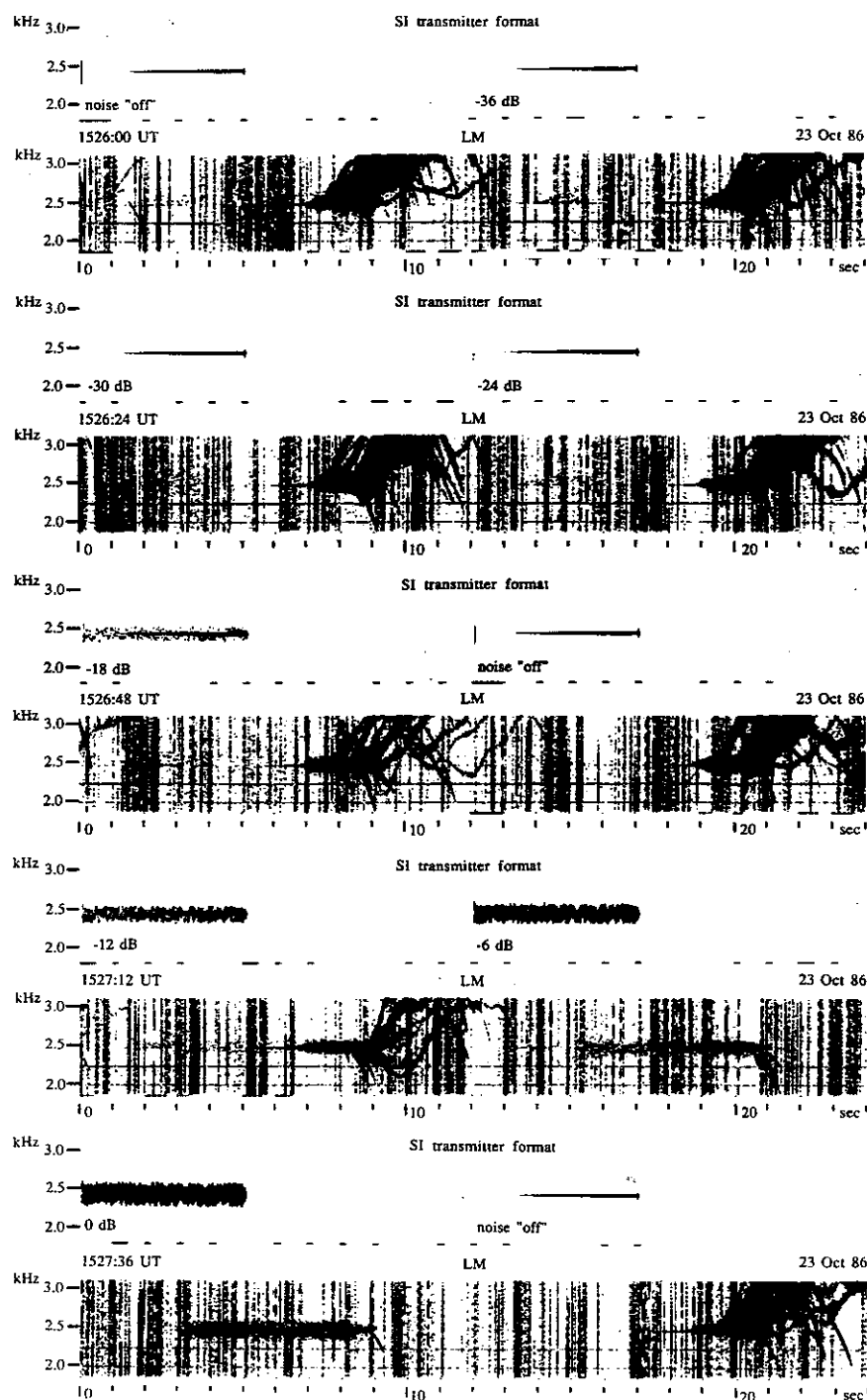


Figure 5.1. The NETH (Noise Effect on Threshold) experiment, showing the suppression of the CWI by simulated noise. Simulated noise intensity (relative to the coherent test signal) is indicated on the Siple (SI) transmitter format spectra. The transmitted signals are received at Lake Mistissini (LM) after a  $\approx 3$  second propagation delay. The short (less than 1 second) pulses at the bottom of the spectra are timing signals. After [Mielke and Helliwell, 1992].

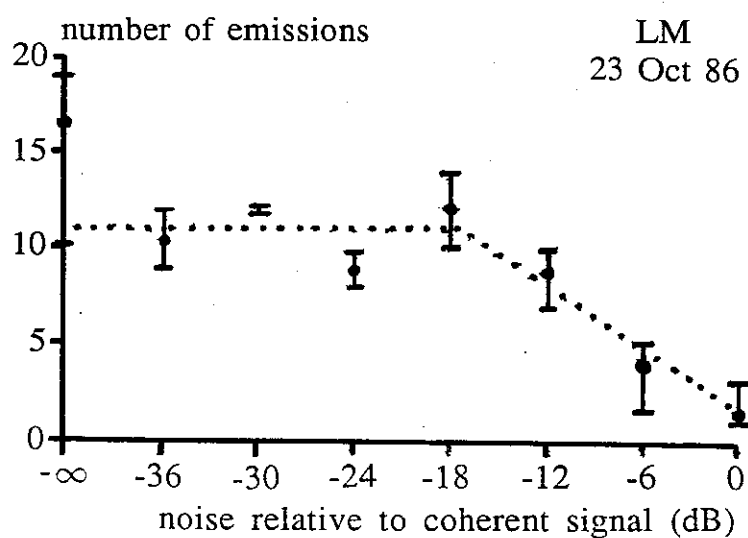


Figure 5.2. Number of triggered emissions versus intensity of the simulated noise. Dots are averages, bars indicate extreme values, and the dotted line indicates the expected trend if the “ambient noise” hypothesis is correct. Data are based on 24 pulses transmitted between 1525 UT and 1530 UT on 23 Oct 86. After [Mielke and Helliwell, 1992].

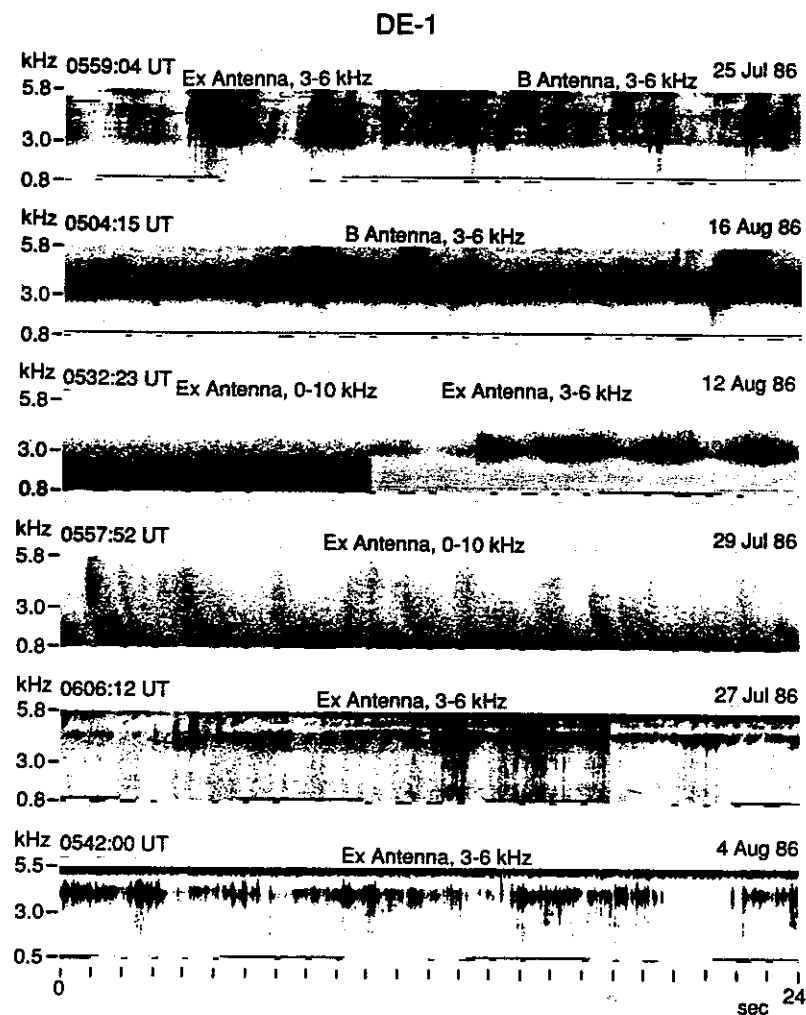


Figure 5.3. Natural noise near the expected CWI interaction region observed by the DE-1 satellite. The line near the bottom of the spectra is a gain-tone which indicates antenna choice and the state of the amplifier automatic gain control in the 3-6 kHz (linear wave receiver) mode. In the 0-10 kHz (wideband receiver) mode wave intensity data is not readily available. Timing signals (pulses of 1 second or less) are apparent below the gain tone. After [Mielke and Helliwell, 1992].

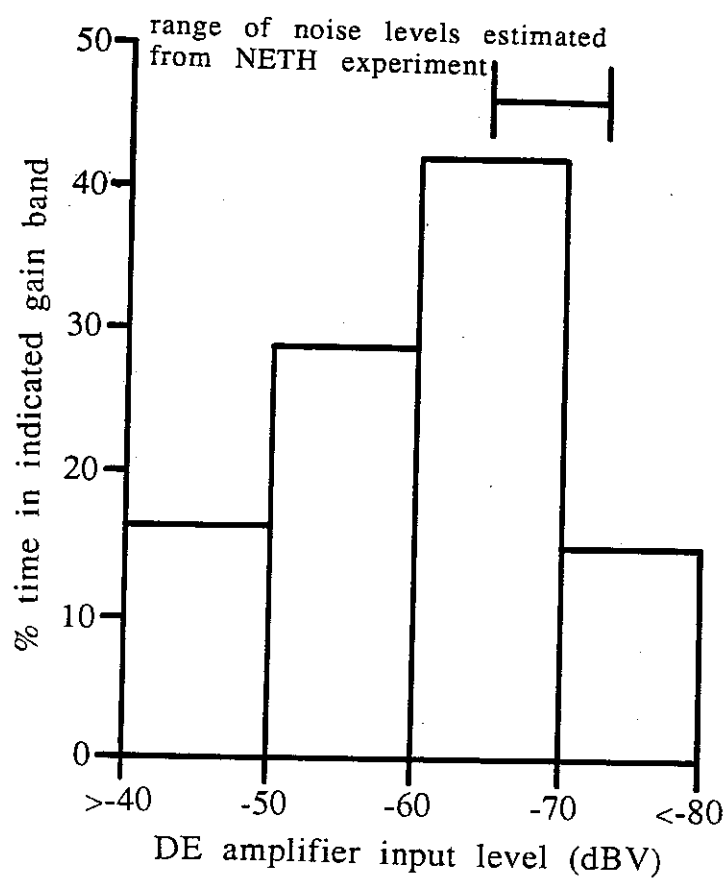


Figure 5.4. Histogram of natural noise intensity observed on DE-1 with the noise level estimated by the NETH experiment indicated. The data covered 68 minutes spread over 10 days in July and August 1982. After [Mielke and Helliwell, 1992].

For conditions typical of Siple signals, with a plasma density of 400 electrons/cc, a gyrofrequency of 13.6 kHz ( $L=4$ , geomagnetic equator), and a wave frequency of 3 kHz, an unamplified signal intensity of 0.2 pT as observed on satellite data [Inan et al, 1977; Rastani et al, 1985] corresponds to an electric field intensity of about  $2 \mu\text{V/m}$ . The simulated noise at -15dB relative to the test signal is then  $0.36 \mu\text{V/m}$ . The equivalent noise signal on DE-1 (3000 Hz bandwidth, 222 m antenna effective length) [Shawhan et al, 1981; Sonwalker and Inan, 1986] is  $3.6 \times 10^{-7} \sqrt{3000/200} \times 222 = 3.1 \times 10^{-4} \text{V} = -70 \text{dBV}$ . In Figure 5.4 a histogram of the natural noise intensity observed on DE-1 ( $E_x$  antenna) is shown, along with the noise level estimated from the NETH experiment. Agreement is satisfactory. Given the uncertainties associated with the lack of simultaneous ground and satellite data and with estimation of the simulated noise intensity, we cannot claim that the "ambient noise" hypothesis is proven, but the data are clearly consistent with that hypothesis. It should be noted that in a "trapping" model of the CWI simulated noise levels comparable to the coherent test signal should also prevent growth. As "trapping" theories ascribe the threshold effect solely to the input wave intensity, however, there is no a priori reason in "trapping" theories to expect simulated noise to cease interfering with growth at the point where it decreases to the in situ natural noise background.

#### D. CONCLUSIONS OF THE THRESHOLD EFFECT EXPERIMENT

Experimental data from Siple Station and the DE-1 satellite support the hypothesis that the coherent wave instability threshold effect is controlled by the ambient noise (probably unducted hiss) in the interaction region. This suggests that ground data on the threshold effect could be used to estimate the intensity of unducted magnetospheric noise that is usually not detected on the ground because of its relatively high wave normal angles.

## VI. Summary and Conclusions

This dissertation covers Siple Station experiments on the coupling of VLF waves from the antenna into the magnetosphere and on wave-particle interactions in the magnetosphere. It summarizes and discusses material from the four papers that have been published on these topics[Helliwell et al, 1990; Mielke et al, 1992; Mielke and Helliwell, 1992; Mielke and Helliwell, 1993]. Contributions made by the research on the experiment on coupling of VLF waves into the magnetosphere include:

- Derivation of an analytic theory of coupling from the Siple Station antenna to whistler-mode signals in the magnetosphere, which was consistent with observations of Siple Station transmitted signals at Lake Mistissini and on the Dynamics Explorer-1 satellite.
- Application of the coupling theory and dispersion data to identify likely duct end point locations.
- The results of the experiment on coupling of VLF waves into the magnetosphere have implications for future experiments. These include the possibility of utilizing the lobed coupling structure resulting from left hand antenna polarization to selectively excite a single field-aligned duct, and the possibility of using right hand polarization in a crossed dipole antenna rather than a single dipole antenna in order to increase the efficiency of whistler-mode signal injection into the magnetosphere.

Contributions made by research on the experiment on wave-particle interactions with linear frequency chirps include:

- Extension of analytic second order gyroresonance theory to regions farther from the magnetic equator, permitting application of analytic theory to frequency ramps with larger  $df/dt$  than was previously possible.
- Application of the extended second order gyroresonance theory to experimental data from Siple Station transmissions, which provided confirmation of the gyroresonance mechanism in the beginning stages of the CWI, and an explanation of the breakdown of wave growth for coarse frequency "staircase" approximations to a frequency ramp.

Contributions made by research on the experiment on wave-particle interactions with parabolic frequency "chirps" include:

- Analysis of experimental data showing magnetospheric growth and triggered emissions on pulses with parabolic frequency-versus-time "chirps".
- As growth of such parabolic "chirps" via second order gyroresonance occurs away from the magnetic equator, this phenomenon could be used to probe the plasma environment on open magnetic field lines, outside the plasmasphere.

- Growth of such parabolic "chirps" away from the magnetic equator could also be used as a probe of the distribution of hot plasma on closed magnetic field lines. Different curvatures would be resonant at different locations along the same field-aligned duct, in principle allowing spatial and temporal mapping of hot plasma in the magnetosphere with a ground-based experiment.

Contributions made by research on the experiment on the threshold effect in the coherent wave instability include:

- Analysis of experimental data on the "threshold effect" [Helliwell et al, 1980], in which the transmitted wave intensity must exceed some threshold intensity before the CWI is excited. This experiment tested the hypothesis that in-situ hiss is responsible for the threshold effect. Results were consistent with the "in-situ hiss" hypothesis.

- The results of the noise effect on threshold experiment suggest that ground data on the suppression of growth by artificial noise could be used to estimate the intensity of unducted magnetospheric hiss that is usually not detected on the ground because of its relatively high wave normal angles.

## Appendix A. Survey of Siple Data and Suggested Future Work

Much of the data from various Siple Station experiments using the VLF transmitter has not been analyzed. A brief review of the current status of Siple data analysis follows, with specific suggestions regarding future work on particular subsets of data, organized by transmitter format. A table listing all transmitter formats in use since 1986 is provided.

About half of the listed formats have been investigated. This dissertation involves the POLA, STACO, NOWS, and NETH formats. Luiz Sa worked on the sideband generation problem, using the formats CBAF, CBVA, CBVF, CISP, PLCCS, PLCRS, PLCTR, PLC1P, PLC2N, PLC2P, PLC60, and PLIC. Only CISP data have been published [Sa and Helliwell, 1988]. Tim Bell and Vikas Sonwalker are working on satellite data, and have examined DE1F, DE861, ISEWN, ISIS87, PRCP5 (used for low orbiting satellites), and VKING formats. Cheng Ong, supervised by R. A. Helliwell and with technical assistance from T. Mielke and W. Burgess, performed a survey of the WIPP1, WIPP2, and WIPP3 formats. Neither Siple Station 20.5 MHz riometer data nor perturbations on VLF propagation from NAA to Saskatoon and Lake Mistissini or NAU to Lake Mistissini showed evidence of energetic particle precipitation correlated with WIPP transmissions. As many of the cases with strong growth and triggering on cw pulses also show evidence of growth and sideband generation on the frequency doublets, a search for phase variations in the WIPP doublets which are correlated with WIPP cw pulses would probably give positive results. It would, however, be difficult to distinguish between correlations caused by particle precipitation and correlations caused by magnetospheric growth of the doublet. Don Carpenter, Vikas Sonwalker, and D. Caudle have done an in-depth analysis of HR241 data. Temporal variations in hot plasma, on a variety of time scales, as evidenced by corresponding variations in magnetospheric growth of Siple signals, are evident. Research on this data set is continuing, and potentially could lead to a ground-based hot plasma diagnostic [V. Sonwalker, personal communication].

Further work, possibly involving undergraduates on research projects, could be attempted. Particular Siple experiments which appear suitable in that their analysis does not require technical sophistication or a deep background in magnetospheric physics include:

CBEX1; investigate magnetospheric growth, suppression, and sideband generation on a coherent pulse versus frequency separation and intensity of a competing signal.

FPATH; search for phase variations in a Siple transmission as received in Canada. Such variations may indicate particle precipitation.

LANDAU (included as a diagnostic), MDIAG and NDIAG; a systematic study of these diagnostic signals could characterize temporal variation of magnetospheric properties and correlations with geomagnetic time, geomagnetic indices ( $K_p$ , etc.).

PAFC1; examine magnetospheric growth of chirped (parabolic frequency versus time) Siple transmissions as a function of first and second derivatives. The use of dispersion analysis, as developed in Appendix B, along with third order resonance, as developed in Appendix C and Appendix D, might allow estimation of interaction lengths for chirped pulses in both PAFC1 and NOWS formats.

STACO; assemble statistics on growth of frequency staircases versus coarseness and sign of ramp slope.

DANE3, TECA1, and TECA2; examine experiments on entrainment of triggered emissions for patterns in morphologies. A systematic examination of this data set on wave-wave magnetospheric interactions might test existing theories.

SULFA; determine if pulsed VLF transmissions stimulated ULF waves in the magnetosphere.

THRSH, THRH2, and THRH3; gather statistics on threshold phenomenon seen in magnetospheric growth and emission triggering. Possibly comparison with magnetospheric hiss statistics derived from DE-1 satellite would elucidate the mechanism behind the threshold phenomenon.

NOWS; gather statistics on the frequency with which artificial nose whistlers transmitted at Siple Station can be observed at Lake Mistissini, Quebec. Growth tends to occur first on cw pulses, then on linear frequency ramps, and last on pulses with frequency-time curvature. Interaction regions for these respective pulses are correspondingly farther from the magnetic equator. Such a study would yield data on spatial and temporal magnetospheric variations.

Satellite data (DE-1 in particular); examine the variation of signal strength of VLF ground transmitters versus distance from the transmitting station for evidence of the proposed "linear growth" [Dowden, 1978]. If "linear growth" occurs, observed signal strengths should be greater than predicted by models assuming propagation effects alone.

Examine the effects of addition of noise to small-signal and large-signal theories of magnetospheric growth. This might involve numerical simulations (such as performed in [Carlson, 1990]), or simplified analytic models. It should be noted that analytic models for the gyro-resonance would need to be developed; not a trivial task. While numerical simulations have been performed, computer memory limitations to date have prevented the use of even frequency doublets, let alone more complicated signals. Still, historical trends in computing power and cost allow for hope in this area.

Pre-1986 formats probably also deserve some attention. That previous generations of students have extracted all the useful information from that data set seems unlikely. In particular, data from the NOSI-1 format show periodic chorus-like elements generated by artificial hiss. Linkage of individual hiss wavelets by second order resonance, as discussed in Appendix E, may be able to explain this artificial chorus generation.

Table 3. List of Siple Station transmitter formats in use since 1986.

<u>format</u>	<u>subject of experiment</u>
CBEX1	growth, suppression, sidebands
CBAF	sideband generation
CBAF2	sideband generation
CBVA	growth suppression by doublets
CBVA1	growth suppression by doublets
CBVF	sideband generation
CISP	power-line harmonic interactions
DANE3	entrainment
DE1F	satellite
DE861	satellite
DIAG	temporal variation of frequency and power ramps
FPATH	phase path variations due to precipitation
FRAHI	stimulate hiss and magnetospheric lines
GACO	interruptions in CW pulses to affect growth
HISS1	artificial hiss
HISS2	artificial hiss
HR241	diagnostic for 24-hour operation
HSS12	artificial hiss
HSS22	artificial hiss
HSS31	artificial hiss
HSS41	artificial hiss
HSS42	artificial hiss
HSS51	artificial hiss
HSS52	artificial hiss
HSS61	artificial hiss
ISEWN	satellite wave-normals
ISIS87	spectral broadening on satellite
LANDAU	gyro versus Landau resonance
LICO2	frequency doublets
MDIAG	normal diagnostic (temporal variations)
MSI1	magnetospheric line generation
NDIAG	new diagnostic (temporal variations)
NETH1	triggering threshold versus noise
NETH2	triggering threshold versus noise
NOSI3	artificial hiss
NOSS	artificial noise with cw pulses and frequency ramps
NOWS1	artificial noise whistlers
NOWS3	artificial noise whistlers
PAFC1	parabolic frequency chirps
PC1M1	frequency doublet
PIPS2	frequency doublet
PLCCS	sideband generation
PLCRS	sideband generation
PLCTR	sideband generation and emissions
PLC1P	sideband generation
PLC2N/GMEAN	sideband generation

PLC2P/GMEAP	sideband generation
PLG60	sideband generation
PLIC	sideband generation
POLAD	antenna polarization
POLA1	antenna polarization
POLA2	antenna polarization
POLA3	antenna polarization
PRCP5	frequency ramps
STACO	frequency staircases
STCO2	frequency staircases
SUBIONOSPHERIC PROPAGATION EXPERIMENT	
SULFA	stimulate ULF with modulated VLF
TECA1	control of stimulated emissions
TECA2	control of stimulated emissions
THRSH	triggering threshold and saturation
THR2	triggering threshold and saturation
THR3	triggering threshold and saturation
VKING	satellite particle measurements
WEWP1	nested simulated nose whistlers
WIPP/WIPP1	induce precipitation and detect by doublet phase
WIPP2	induce precipitation and detect by Trimpi event
WIPP3	induce precipitation

## Appendix B: Dispersion in the Plasmasphere

The following equations concern ducted whistler-mode dispersion in a dipole magnetic field, with a diffusive equilibrium model of electron density [Park, 1972].

### Magnetospheric Conditions

$$f_{H_{eq}} = \frac{873.6}{L^3} \text{kHz}$$

$$f_{p_{eq}} = 8.9775 \sqrt{n_{eq}} \text{kHz with electron density } n_{eq} \text{ in } \text{cm}^{-3}$$

$$v_p = c \frac{f_H}{f_p} \Lambda^{1/2} (1 - \Lambda)^{1/2}$$

$$v_g = 2c \frac{f_H}{f_p} \Lambda^{1/2} (1 - \Lambda)^{3/2}$$

$$\sin^2 \alpha = \frac{f_H}{f_{H_{eq}}} \sin^2 \alpha_{eq}$$

where  $\Lambda = f/f_H$  and  $\alpha_{eq}$  is the equatorial pitch angle.

### Gyrofrequency Expansion

$$f_H = f_{H_{eq}} \frac{(4 - 3 \sin^2 \theta)^{1/2}}{\sin^6 \theta}$$

$$f_H(s) = f_H|_{s_0} + \frac{df_H}{ds}|_{s_0} \Delta s + \frac{1}{2} \frac{d^2 f_H}{ds^2}|_{s_0} \Delta s^2 + \frac{1}{6} \frac{d^3 f_H}{ds^3}|_{s_0} \Delta s^3 + \dots$$

$$\frac{df_H}{ds} = -f_H \frac{3 \cos \theta (3 + 5 \cos^2 \theta)}{R_{eq} \sin^2 \theta (1 + 3 \cos^2 \theta)^{3/2}}$$

$$\frac{d^2 f_H}{ds^2} = f_H \frac{3(3 + 45 \cos^2 \theta + 102 \cos^4 \theta - 43 \cos^6 \theta - 75 \cos^8 \theta)}{R_{eq}^2 \sin^4 \theta (1 + 3 \cos^2 \theta)^3}$$

$$\frac{d^3 f_H}{ds^3} = f_H \frac{3 \cos \theta (39 + 592 \cos^2 \theta + 2046 \cos^4 \theta + 4728 \cos^6 \theta + 2835 \cos^8 \theta)}{R_{eq}^3 \sin^6 \theta (1 + 3 \cos^2 \theta)^{9/2}}$$

$$\text{with } R_{eq} = L R_{earth} = L(6371 \text{km})$$

$\theta$  = the polar angle in spherical coordinates

and  $ds = R_{eq} \sin \theta (4 - 3 \sin^2 \theta)^{1/2} d\theta$  taken in the direction of increasing  $\theta$ .

### Plasma Frequency Expansion

$$f_p = f_{p_{eq}} \exp -((R_{earth} \cot^2 \theta)/2HL)$$

$$f_p(s) = f_p|_{s_0} + \frac{df_p}{ds}|_{s_0} \Delta s + \frac{1}{2} \frac{d^2 f_p}{ds^2}|_{s_0} \Delta s^2 + \frac{1}{6} \frac{d^3 f_p}{ds^3}|_{s_0} \Delta s^3 + \dots$$

$$\frac{df_p}{ds} = -\frac{f_p \cos \theta}{HL^2 \sin^4 \theta (1 + 3 \cos^2 \theta)^{1/2}}$$

$$\frac{d^2 f_p}{ds^2} = -\frac{f_p \left( \frac{R_{eq} \cos^2 \theta}{HL^2 \sin^3 \theta} - \frac{4 \cos^2 \theta}{\sin \theta} + \frac{3 \cos^2 \theta \sin \theta}{1 + 3 \cos^2 \theta} - \sin \theta \right)}{H R_{eq} L^2 \sin^5 \theta (1 + 3 \cos^2 \theta)}$$

$$\text{with } H = (kT)/(m_{electron} g)$$

### Dispersion

Following the approach of [Daniell, 1986a; Daniell, 1986b] the dispersion integral

$$D = t\sqrt{f} = \frac{1}{2c} \int_{path} \frac{f_p f_H}{(f_H - f)^{3/2}} ds$$

is approximated by:

$$\frac{1}{2c} \int_{-s_E}^0 \frac{(f_{p0} + f'_{p0} \Delta s + 1/2 f''_{p0} \Delta s^2)(f_{H0} + f'_{H0} \Delta s + 1/2 f''_{H0} \Delta s^2)}{(f_{H0} + f'_{H0} \Delta s + 1/2 f''_{H0} \Delta s^2)^{3/2}} d\Delta s$$

with  $f_{H0}$  the minimum gyrofrequency on the path of integration,  $f_{p0}$  the plasma frequency at the same location, designated  $s_0$ , and  $s_E$  the distance along the field line from  $s_0$  to the earth's surface. In a dipole field,

$$s = \frac{R_{eq}(x + \sinh x \cosh x)}{2\sqrt{3}}$$

where  $\sinh x = \sqrt{3} \cos \theta$  and  $\theta = \arcsin \sqrt{L}$  at the earth's surface.

The numerator of the above integrand is expanded and all terms of order  $\Delta s^3$  and higher are dropped. Frequencies are scaled by  $f_{H0}$  and distances by wavelength  $\lambda$ . Integration using mathematical tables [Gradshteyn and Ryzhik, 1980] then yields polynomials and a logarithmic term in  $\Delta s$ . The approximate integral is dominated by contributions near the region  $\Delta s = 0$ , where the approximate integrand is fairly accurate. As the true integral, which is much harder to obtain, is also dominated by contributions near the minimum gyrofrequency, this approach gives good results, and has been used to obtain the dispersion for one-hop whistlers [Burgess, 1993]. As the exact value

of  $s_E$  (for large  $s_E$ ) has little effect on the value of the integral, it can be chosen to simplify the form of the approximate integral. The choice  $s_E = \infty$  in the polynomial terms makes negligible terms zero, and the choice  $s_E = R_{eq}$  in the logarithmic term is simple, and a fair approximation over a wide range of L-shells. (Beyond  $s_E \approx 200\lambda$ , the approximate integrand tends to be larger than the true integrand, but the resulting erroneous contribution can be neglected in the polynomial terms of order  $1/\Delta s^2$  and  $1/\Delta s^3$ . The order  $1/\Delta s$  term, which when integrated leads to a logarithmic term does require some care, as it is potentially divergent). The result, with  $\lambda = c/f$ , and  $s_E > 200\lambda$ , is:

$$\begin{aligned}
 D = & + \frac{(f_{H0})^{1/2} [f f_{p0} f'_{H0} / f_{H0} + (1 - f/f_{H0}) (f''_{p0} f_{H0} f'_{H0} / f''_{H0} - 2f'_{p0} f_{H0} + 2f'_{p0} (f'_{H0})^2 / f''_{H0})]}{c[2(f_{H0} - f) f''_{H0} - (f'_{H0})^2] (1 - f/f_{H0})^{1/2}} \\
 & + \frac{f(f_{p0} f''_{H0} + 2f'_{p0} f'_{H0}) + (f'_{H0})^2 (2f'_{p0} f'_{H0} + f''_{p0} f_{H0}) / f''_{H0}}{c[2(f_{H0} - f) f''_{H0} - (f'_{H0})^2] (f''_{H0}/2)^{1/2}} \\
 & - \frac{(1 - f/f_{H0}) f''_{p0} (f_{H0})^2 + 3f'_{p0} f_{H0} f'_{H0}}{c[2(f_{H0} - f) f''_{H0} - (f'_{H0})^2] (f''_{H0}/2)^{1/2}} \\
 & - \frac{(f_{p0} f''_{H0} + 2f'_{p0} f'_{H0} + f''_{p0} f_{H0})}{\sqrt{2} c (f''_{H0})^{3/2}} \ln \left[ \frac{\sqrt{2\lambda^2 f''_{H0} (f_{H0} - f)} - \lambda f'_{H0} / f_{H0}}{2(\lambda R_{eq} f''_{H0} / f_{H0} - \lambda f'_{H0} / f_{H0})} \right]
 \end{aligned}$$

This result can be used at any point on a magnetic field line sufficiently far from the ionosphere, either directly for a  $0^+$  whistler, or subtracted from the single-hop dispersion for a  $1^-$  whistler. With  $s_0$  taken at the magnetic equator, odd derivatives go to zero and the above formula simplifies to the same form as that in [Burgess, 1993].

### Appendix C: Third Order Gyroresonance Equations

The formulas presented here have not been independently verified. In view of the algebric complexity of the derivation of the higher order derivatives, an independent check would be desirable.

The gyrofrequency equations are presented in Appendix A.

The following equations for the Doppler-shifted wave frequency  $f'$  assume the first order resonance condition  $f' = f_H$  and also make use of the relationship  $df/ds = df/dt(1/v_{||} + 1/v_g)$

$$f' = f(1 + \frac{v_{||}}{v_p})$$

$$f'(s) = f'|_{s_0} + \frac{df'}{ds}|_{s_0}\Delta s + \frac{1}{2}\frac{d^2f'}{ds^2}|_{s_0}\Delta s^2 + \frac{1}{6}\frac{d^3f'}{ds^3}|_{s_0}\Delta s^3 + \dots$$

$$\frac{df'}{ds} = \frac{df}{dt} \frac{(1+2\Lambda)^2}{4v_p\Lambda(1-\Lambda)} - \frac{df_H}{ds} \frac{1+(1-\Lambda)\tan^2\alpha}{2} + \frac{df_p}{ds} \frac{f(1-\Lambda)}{f_p\Lambda}$$

$$\begin{aligned} \frac{d^2f'}{ds^2} = & -\frac{d^2f_H}{ds^2} \frac{1+(1-\Lambda)\tan^2\alpha}{2} + \left(\frac{df_H}{ds}\right)^2 \frac{4-[1-(1-\Lambda)\tan^2\alpha]^2}{4f_H(1-\Lambda)} \\ & - \frac{df_H}{ds} \frac{df}{dt} \frac{(1+2\Lambda)[3(1+2\Lambda)+2(1-\Lambda)^2\tan^2\alpha]}{8f_Hv_p\Lambda(1-\Lambda)^2} - \left(\frac{df}{dt}\right)^2 \frac{3(1+2\Lambda)^2(1-4\Lambda)}{16f_Hv_p^2\Lambda^2(1-\Lambda)^3} \\ & + \frac{d^2f}{dt^2} \frac{(1+4\Lambda)(1+2\Lambda)^2}{8v_p^2\Lambda(1-\Lambda)^2} + \frac{d^2f_p}{ds^2} \frac{f_H(1-\Lambda)}{f_p} + \frac{df_p}{ds} \frac{df}{ds} \frac{(1+2\Lambda)^2}{4f_pv_p\Lambda(1-\Lambda)} \\ & - \frac{df_p}{ds} \frac{df_H}{ds} \frac{1+(1-\Lambda)\tan^2\alpha}{f_p} \end{aligned}$$

$$\begin{aligned}
\frac{d^3 f'}{ds^3} = & + \frac{d^3 f}{dt^3} \frac{(1+2\Lambda)^3}{16v_p^3 \Lambda(1-\Lambda)^3} - \frac{d^3 f_p}{ds^3} \frac{f_H(1-\Lambda)}{f_p} \\
& - \frac{d^3 f_H}{ds^3} \frac{(1-\Lambda)(1-\tan^2 \alpha)}{2} \\
& + \frac{d^2 f}{dt^2} \frac{df}{dt} \frac{(1-2\Lambda)^2(-3+\Lambda+46\Lambda^2+4\Lambda^3-24\Lambda^4)}{16v_p^3 f \Lambda(1-\Lambda)^4} \\
& + \frac{d^2 f}{dt^2} \frac{df_p}{ds} \frac{(1+2\Lambda)(4+3\Lambda-6\Lambda^2)}{4v_p^2 f_p \Lambda(1-\Lambda)^2} \\
& - \frac{d^2 f}{dt^2} \frac{df_H}{ds} \frac{(1+2\Lambda)^2(5+6\Lambda) + (1+2\Lambda)(1-\Lambda)(3+4\Lambda+6\Lambda^2) \tan^2 \alpha}{16v_p^2 f(1-\Lambda)^3} \\
& + \frac{d^2 f_p}{ds^2} \frac{df}{dt} \frac{(1+2\Lambda)}{v_p f_p \Lambda(1-\Lambda)} \\
& - \frac{d^2 f_p}{ds^2} \frac{df_H}{ds} \frac{3[1+(1-\Lambda) \tan^2 \alpha]}{2f_p} \\
& - \frac{d^2 f_H}{ds^2} \frac{df}{dt} \frac{4(1+2\Lambda)^2 + (1+2\Lambda)(1-\Lambda)(3+4\Lambda) \tan^2 \alpha}{8v_p f(1-\Lambda)^2} \\
& - \frac{d^2 f_H}{ds^2} \frac{df_p}{ds} \frac{3(1-\Lambda)(2+\tan^2 \alpha)}{2f_p} \\
& + \frac{d^2 f_H}{ds^2} \frac{df_H}{ds} \frac{9+6(1-\Lambda) \tan^2 \alpha - 3(1-\Lambda)^2 \tan^4 \alpha}{4f_H(1-\Lambda)} \\
& + \left(\frac{df_p}{ds}\right)^2 \frac{df}{dt} \frac{3}{2v_p f^2 \Lambda} \\
& - \frac{df_p}{ds} \left(\frac{df}{dt}\right)^2 \frac{3(15+16\Lambda+68\Lambda^2-48\Lambda^3-32\Lambda^4)}{16v_p^2 f f_p \Lambda(1-\Lambda)^3} \\
& + \frac{df_p}{ds} \left(\frac{df_H}{ds}\right)^2 \frac{9(1-2\Lambda)^2 + 6\Lambda^2(1-\Lambda) \tan^2 \alpha - 3\Lambda^2(1-\Lambda)^2 \tan^4 \alpha}{4f f_p \Lambda(1-\Lambda)} \\
& - \frac{df_p}{ds} \frac{df_H}{ds} \frac{df}{dt} \frac{(35-6\Lambda-120\Lambda^2+72\Lambda^3) + 3(1-\Lambda)(3-4\Lambda+8\Lambda^2) \tan^2 \alpha}{8v_p f f_p(1-\Lambda)^2} \\
& - \left(\frac{df_H}{ds}\right)^3 \frac{(27-12\Lambda) + 9(1-\Lambda) \tan^2 \alpha - 3(1-\Lambda)^2 \tan^4 \alpha + 3(1-\Lambda)^3 \tan^6 \alpha}{8f_H^2(1-\Lambda)^2} \\
& - \left(\frac{df_H}{ds}\right)^2 \frac{df}{dt} \frac{(33+128\Lambda+152\Lambda^2-24\Lambda^3)}{16v_p f f_H(1-\Lambda)^3} \\
& - \left(\frac{df_H}{ds}\right)^2 \frac{df}{dt} \frac{-3(1-\Lambda)(1+2\Lambda)(3+2\Lambda-4\Lambda^2) \tan^2 \alpha + 3(1-\Lambda)^2(1+3\Lambda+4\Lambda^2) \tan^4 \alpha}{16v_p f f_H(1-\Lambda)^3} \\
& - \frac{df_H}{ds} \left(\frac{df}{dt}\right)^2 \frac{(6+111\Lambda-296\Lambda^2-392\Lambda^3-264\Lambda^4)}{32v_p^2 f^2(1-\Lambda)^4} \\
& - \frac{df_H}{ds} \left(\frac{df}{dt}\right)^2 \frac{-(1-\Lambda)(9-22\Lambda-8\Lambda^2+48\Lambda^3) \tan^2 \alpha}{32v_p^2 f^2(1-\Lambda)^4} \\
& + \left(\frac{df}{dt}\right)^3 \frac{(1+2\Lambda)(12-33\Lambda-8\Lambda^2+170\Lambda^3+48\Lambda^4+96\Lambda^5)}{32v_p^3 f^2 \Lambda(1-\Lambda)^5}
\end{aligned}$$

### Appendix D: Third Order Landau Resonance Equations

Equations for  $f_H$  and its derivatives are in Appendix A.

Note: for Landau resonance the sign of  $df_H/ds$  is opposite the gyroresonance case due to a change in the direction of  $s$ .

The following equations for spatial derivatives of  $v_p$  assume that the first order resonance condition  $v_p = v_{||}$  holds. They are derived making use of the relationship  $df/ds = df/dt(1/v_{||} - 1/v_g)$ . They have not been independently verified, and in view of the involved algebra required to obtain the higher order derivatives an independent check is desirable.

$$v_{||} = v(1 - \frac{f_H}{f_{H_{eq}}} \sin^2 \alpha)^{1/2}$$

$$v_{||}(s) = v_{||}|_{s_0} + \frac{dv_{||}}{ds}|_{s_0} \Delta s + \frac{1}{2} \frac{d^2 v_{||}}{ds^2}|_{s_0} \Delta s^2 + \frac{1}{6} \frac{d^3 v_{||}}{ds^3}|_{s_0} \Delta s^3 + \dots$$

$$\frac{dv_{||}}{ds} = \frac{-v_{||} \tan^2 \alpha}{2f_H} \frac{df_H}{ds}$$

$$\frac{d^2 v_{||}}{ds^2} = \frac{-v_{||} \tan^4 \alpha}{4f_H^2} \left(\frac{df_H}{ds}\right)^2 - \frac{v_{||} \tan^2 \alpha}{2f_H} \frac{d^2 f_H}{ds^2}$$

$$\frac{d^3 v_{||}}{ds^3} = -\frac{v_{||} \tan^2 \alpha}{2f_H} \frac{d^3 f_H}{ds^3} - \frac{3v_{||} \tan^4 \alpha}{4f_H^2} \frac{d^2 f_H}{ds^2} \frac{df_H}{ds} - \frac{3v_{||} \tan^6 \alpha}{8f_H^3} \left(\frac{df_H}{ds}\right)^3$$

$$v_p = c \frac{f_H}{f_p} \Lambda^{1/2} (1 - \Lambda)^{1/2}$$

$$v_p(s) = v_p|_{s_0} + \frac{dv_p}{ds}|_{s_0} \Delta s + \frac{1}{2} \frac{d^2 v_p}{ds^2}|_{s_0} \Delta s^2 + \frac{1}{6} \frac{d^3 v_p}{ds^3}|_{s_0} \Delta s^3 + \dots$$

$$\frac{dv_p}{ds} = \frac{v_p}{2f_H(1-\Lambda)} \frac{df_H}{ds} + \frac{(1-2\Lambda)^2}{4f(1-\Lambda)^2} \frac{df}{dt} - \frac{v_p}{f_p} \frac{df_p}{ds}$$

$$\begin{aligned} \frac{d^2 v_p}{ds^2} = & + \frac{1-2\Lambda}{8v_p f(1-\Lambda)^3} \frac{d^2 f}{dt^2} - \frac{2v_p}{f_p} \frac{d^2 f_p}{ds^2} \\ & + \frac{v_p}{2f_H(1-\Lambda)} \frac{d^2 f_H}{ds^2} - \frac{v_p}{4f_H^2(1-\Lambda)^2} \left(\frac{df_H}{ds}\right)^2 \\ & - \frac{(1+2\Lambda)[+(3+2\Lambda)+2(1-\Lambda)^2 \tan^2 \alpha]}{8f_H^2 \Lambda(1-\Lambda)^3} \frac{df_H}{ds} \frac{df}{dt} + \frac{(1-2\Lambda)^2(1-4\Lambda)}{16v_p f^2(1-\Lambda)^4} \left(\frac{df}{dt}\right)^2 \\ & + \frac{2v_p}{f_p^2} \left(\frac{df_p}{ds}\right)^2 - \frac{v_p}{f_p f_H(1-\Lambda)} \frac{df_p}{ds} \frac{df_H}{ds} + \frac{(1-2\Lambda)(3-4\Lambda)}{4f f_p(1-\Lambda)^2} \frac{df_p}{ds} \frac{df}{dt} \end{aligned}$$

$$\begin{aligned}
\frac{d^3 v_p}{ds^3} = & + \frac{v_p}{f_p} \frac{d^3 f_p}{ds^3} + \frac{6v_p}{f_p^2} \frac{d^2 f_p}{ds^2} \frac{df_p}{ds} - \frac{3v_p}{2f_p f_H (1-\Lambda)} \frac{d^2 f_p}{ds^2} \frac{df_H}{ds} \\
& - \frac{(1-2\Lambda)(2-3\Lambda)}{2f_p f_H (1-\Lambda)^2} \frac{d^2 f_p}{ds^2} \frac{df}{dt} \\
& - \frac{6v_p}{f_p^3} \left( \frac{df_p}{ds} \right)^3 \\
& + \frac{3v_p}{f_p^2 f_H (1-\Lambda)} \left( \frac{df_p}{ds} \right)^2 \frac{df_H}{ds} \\
& + \frac{(1-2\Lambda)(4-3\Lambda)}{f f_p^2 (1-\Lambda)^2} \left( \frac{df_p}{ds} \right)^2 \frac{df}{dt} \\
& - \frac{3v_p \Lambda}{f_H f_p (1-\Lambda)} \frac{df_p}{ds} \frac{d^2 f_H}{ds^2} \\
& - \frac{3(1-2\Lambda)^2(3-5\Lambda)}{8v_p f f_p (1-\Lambda)^3} \frac{df_p}{ds} \frac{d^2 f}{dt^2} \\
& - \frac{3v_p(3-12\Lambda+8\Lambda^2)}{4f_p f_H^2 (1-\Lambda)^2} \frac{df_p}{ds} \left( \frac{df_H}{ds} \right)^2 \\
& + \frac{(1-2\Lambda)(-7+81\Lambda-112\Lambda^2)}{16v_p f^2 f_p (1-\Lambda)^4} \frac{df_p}{ds} \left( \frac{df}{dt} \right)^2 \\
& - \frac{(13-38\Lambda+60\Lambda^2-48\Lambda^3)+12(1-2\Lambda)(1-\Lambda)^2 \tan^2 \alpha}{8f f_p f_H (1-\Lambda)^3} \frac{df_p}{ds} \frac{df_H}{ds} \frac{df}{dt} \\
& + \frac{v_p}{2f_p f_H (1-\Lambda)} \frac{d^3 f_H}{ds^3} \\
& - \frac{3v_p}{4f_H^2 (1-\Lambda)^2} \frac{d^2 f_H}{ds^2} \frac{df_H}{ds} \\
& + \frac{(1-2\Lambda)[(2+\Lambda)+(1-\Lambda)^2 \tan^2 \alpha]}{4f f_H (1-\Lambda)^3} \frac{d^2 f_H}{ds^2} \frac{df}{dt} \\
& + \frac{3v_p(5-4\Lambda)}{8f_H^3 (1-\Lambda)^3} \left( \frac{df_H}{ds} \right)^3 \\
& - \frac{(3+20\Lambda-28\Lambda^2)+6\Lambda(1-\Lambda)^2 \tan^2 \alpha}{16f f_H^2 (1-\Lambda)^4} \left( \frac{df_H}{ds} \right)^2 \frac{df}{dt} \\
& + \frac{(1-2\Lambda)(11-14\Lambda-12\Lambda^2-120\Lambda^3)+4(3-7\Lambda)(1-\Lambda)^2 \tan^2 \alpha}{32v_p f^2 f_H (1-\Lambda)^5} \frac{df_H}{ds} \left( \frac{df}{dt} \right)^2 \\
& + \frac{3(1-2\Lambda)^2[(1+\Lambda)+(1-\Lambda)^2 \tan^2 \alpha]}{8v_p f f_H (1-\Lambda)^4} \frac{df_H}{ds} \frac{d^2 f}{dt^2} \\
& + \frac{(1-2\Lambda)^4}{16v_p^2 f (1-\Lambda)^4} \frac{d^3 f}{dt^3} \\
& + \frac{(1-2\Lambda)^2(1-3\Lambda+8\Lambda^2)}{8v_p^2 f^2 (1-\Lambda)^5} \frac{d^2 f}{dt^2} \frac{df}{dt} \\
& + \frac{(1-2\Lambda)(-14+117\Lambda-410\Lambda^2+580\Lambda^3-384\Lambda^4)}{64v_p^2 f^3 (1-\Lambda)^6} \left( \frac{df}{dt} \right)^3
\end{aligned}$$

### Appendix E: Some Criteria for Linking cw Pulses via Second Order Gyroresonance

Given pulse 1 at  $f_1$  and pulse 2 at  $f_2$ , each of pulse duration  $\tau$  and separated in time by  $\Delta t$ ,

$$df/dt|_{ave} = (f_2 - f_1)/(\tau + \Delta t)$$

$$f|_{ave} = (f_2 + f_1)/2$$

The first order resonance condition  $f'|_{s_0} = f_H|_{s_0}$  (average values) leads to:

$$f_{H_{eq}}(4 - 3\sin^2 \theta)^{1/2} / \sin^6 \theta = f|_{ave}(1 + v_{\parallel}/v_p)$$

The second order resonance condition  $df'/ds|_{s_0} = df_H/ds|_{s_0}$  (average values) leads to:

$$df/dt|_{ave} \frac{(1 + 2\Lambda)^2}{4v_p\Lambda(1 - \Lambda)} = -f_H \frac{3 \cos \theta (8 - 5 \sin^2 \theta)}{R_{eq} \sin \theta (4 - 3 \sin^2 \theta)} \frac{3 + (1 - \Lambda) \tan^2 \alpha}{2}$$

The instantaneous phase error  $\theta_i$  is given by:

$$\theta_i = \int_0^l \frac{2\pi}{v_{\parallel}} (f_H(s) - f'(s)) ds$$

and is well approximated by :

$$\theta_i = \int_0^l \frac{2\pi}{v_{\parallel}} \left[ \pm \frac{(f_2 - f_1)}{2} (1 + v_{\parallel}|_{s_0}/v_p|_{s_0}) + df_h/ds|_{s_0} \frac{3 + (1 - \Lambda) \tan^2 \alpha}{2} s \right] ds$$

The maximum phase error is at the start/end of the pulse pair, corresponding to the condition:

$$l = \pm \frac{(\tau + \Delta t/2)}{1/v_{\parallel}|_{s_0} + 1/v_g|_{s_0}}$$

The magnitude of the maximum phase error should be less than  $\pi/2$  for effective interaction.

## BIBLIOGRAPHY

- Angerami, J.J., and D. L. Carpenter, Whistler Studies of the Plasmapause in the Magnetosphere, *J. Geophys. Res.*, **71**, 711-725, 1966.
- Bell, T. F., The wave magnetic field amplitude threshold for nonlinear trapping of energetic gyroresonant and Landau resonant electrons by nonducted VLF waves in the magnetosphere, *J. Geophys. Res.*, **91**, 4365-4379, 1986.
- Bernard, L. C., A New Nose Extension Method for Whistlers, *J. Atmos. Terr. Phys.*, **35**, 871-880, 1973.
- Brice, N. M., Traveling Wave Amplification of Whistlers, *J. Geophys. Res.*, **65**, 3840-3842, 1960.
- Brice, N., Fundamentals of Very Low Frequency Emission Generation Mechanisms, *J. Geophys. Res.*, **69**, 4515-4522, 1964.
- Budden, K. G., *Radio Waves in the Ionosphere*, pp. 116-119, Cambridge University Press, Cambridge, 1961.
- Budden, K. G., *The Propagation of Radio Waves*, pp. 304-309, Cambridge University Press, Cambridge, 1985.
- Burgess, W. C., Lightning-Induced Coupling of the Radiation Belts to the Geomagnetically Conjugate Ionospheric Regions, Ph.D. thesis, Stanford University, Stanford, Calif., 1993.
- Carlson, C. R., R. A. Helliwell, and D. L. Carpenter, Variable Frequency VLF Signals in the Magnetosphere: Associated Phenomena and Plasma Diagnostics, *J. Geophys. Res.*, **90**, 1507-1521, 1985.
- Carlson, C. R., R. A. Helliwell, and U. S. Inan, Space-Time Evolution of Whistler-Mode Wave Growth in the Magnetosphere, *J. Geophys. Res.*, **95**, 15073-15089, 1990.
- Carpenter, D. L., Fast Fluctuations in the Arrival Bearing of Magnetospherically Propagating Signals from the Siple, Antarctica, VLF Transmitter, *J. Geophys. Res.*, **85**, 4157-4166, 1980.
- Chang, H. C., U. S. Inan, and T. F. Bell, Energetic electron precipitation due to gyroresonant interactions in the magnetosphere involving coherent VLF waves with slowly varying frequency, *J. Geophys. Res.*, **88**, 7037, 1983.
- Chen, F. F., *Introduction to Plasma Physics and Controlled Fusion, Volume I*, pp. 12, 352, Plenum Press, New York 1984.
- Chodorow, M., and C. Susskind, *Fundamentals of Microwave Electronics*, McGraw-Hill, New York, 1964.
- Daniell, G. J., Approximate dispersion formulae for whistlers, *J. Atmos. Terr. Phys.*, **48**, 267, 1986b.
- Daniell, G. J., Analytic properties of the whistler dispersion function, *J. Atmos. Terr. Phys.*, **48**, 271, 1986b.
- Dowden, R. L., A. D. McKay, L. E. S. Amon, H. C. Koons, and M. H. Dazey, Linear and Nonlinear Amplification in the Magnetosphere During a 6.6-kHz Transmission, *J. Geophys. Res.*, **83**, 169-181, 1978.
- Dysthe, K. B., Some Studies of Triggered Whistler Emissions, *J. Geophys. Res.*, **76**, 6915-6931, 1971.
- Eather, R. H., *Majestic Lights*, p. 219, American Geophysical Union, Washington, D.C., 1980.
- Gradshteyn, I. S., and I. M. Ryzhik, *Table of Integrals, Series, and Products*, p. 83, Academic Press, New York, 1980.
- Helliwell, R. A., J. Katsufakis, M. Trimpi, and N. Brice, Artificially Stimulated Very-Low-Frequency Radiation from the Ionosphere, *J. Geophys. Res.*, **69**, 2391-2394, 1964.
- Helliwell, R. A., *Whistlers and Related Ionospheric Phenomena*, pp. 23-32, 105, 317-321, Stanford University Press, Stanford, California 1965.
- Helliwell, R. A., A Theory of Discrete VLF Emissions from the Magnetosphere, *J. Geophys. Res.*, **72**, 4773-4790, 1967.

- Helliwell, R. A., Intensity of discrete VLF emissions, in *Particles and Fields in the Magnetosphere*, edited by B. M. McCormac, pp. 292-301, D. Reidel, Hingham, Mass., 1970.
- Helliwell, R. A., and J. P. Katsufakis, VLF Wave Injection Into the Magnetosphere From Siple Station, Antarctica, *J. Geophys. Res.*, **79**, 2511-2518, 1974.
- Helliwell, R. A., and J. P. Katsufakis, Controlled Wave-Particle Interaction Experiments, in *Upper Atmosphere Research in Antarctica*, edited by L. J. Lanzerotti and C. G. Park, AGU, Washington D. C., 1978.
- Helliwell, R. A., D. L. Carpenter, and T. R. Miller, Power Threshold for Growth of Coherent VLF Signals in the Magnetosphere, *J. Geophys. Res.*, **85**, 3360-3366, 1980.
- Helliwell, R. A., and U. S. Inan, VLF wave growth and discrete emission triggering in the magnetosphere: a feedback model, *J. Geophys. Res.*, **87**, 3537, 1982.
- Helliwell, R. A., Controlled stimulation of VLF emissions from Siple Station, Antarctica, *Radio Sci.*, **18**, 801-814, 1983.
- Helliwell, R. A., U. S. Inan, J. P. Katsufakis, and D. L. Carpenter, Beat excitation of whistler mode sidebands using the Siple VLF transmitter, *J. Geophys. Res.*, **91**, 143-153, 1986a.
- Helliwell, R. A., D. L. Carpenter, U. S. Inan, and J. P. Katsufakis, Generation of band-limited VLF noise using the Siple transmitter: a model for magnetospheric hiss, *J. Geophys. Res.*, **91**, 4381-4392, 1986b.
- Helliwell, R. A., VLF Wave Stimulation Experiments in the Magnetosphere from Siple Station, Antarctica, *Rev. Geophys.*, **26**, 551-578, 1988.
- Helliwell, R. A., T. Mielke, and U. S. Inan, Rapid Whistler-Mode Wave Growth Resulting From Frequency-Time Curvature, *Geophys. Res. Lett.*, **17**, 599-602, 1990.
- Ho, D. and L. C. Bernard, A Fast Method to Determine the Nose Frequency and Minimum Group Delay of a Whistler when the Causative Spheric is Unknown, *J. Atmos. Terr. Phys.*, **35**, 881-887, 1973.
- Inan, U. S., T. F. Bell, and D. L. Carpenter, Explorer 45 and Imp 6 observations in the magnetosphere of injected waves from the Siple Station VLF transmitter, *J. Geophys. Res.*, **82**, 1177-1187, 1977.
- Inan, U. S., W. C. Burgess, T. G. Wolf, D. C. and Shafer, Lightning-Associated Precipitation of MeV Electrons from the Inner Radiation Belt, *Geophys. Res. Lett.*, **15**, 172-175, 1988.
- Inan, U. S., M. Walt, H. D. Voss, and W. L. Imhof, Energy spectra and pitch angle distributions of lightning-induced electron precipitation: analysis of an event observed on the S81-1 (SEEP) Satellite, *J. Geophys. Res.*, **94**, 1379, 1989.
- Mielke, T. A., C. J. Elkins, R. A. Helliwell, and U. S. Inan, Excitation of whistler mode signals via injection of polarized VLF waves with the Siple transmitter, *Radio Sci.*, **27**, 31-46, 1992.
- Mielke, T. A., and R. A. Helliwell, An Experiment on the Threshold Effect in the Coherent Wave Instability, *Geophys. Res. Lett.*, **19**, 2075-2078, 1992.
- Mielke, T. A., and R. A. Helliwell, Siple Station, Antarctica, Experiments on Staircase Frequency Ramps as Approximations to Continuous Ramps, *J. of Geophys. Res.*, **98**, 4053-4061, 1993.
- Molvig, K., G. Hilfer, R. H. Miller, and J. Myczkowski, Self-consistent Theory of Triggered Whistler Emissions, *J. Geophys. Res.*, **93**, 5665-5683, 1988.
- Nunn, D., A Self-consistent Theory of Triggered VLF Emissions, *Planet. Space Sci.*, **22**, 349-378, 1974.
- Park, C. G., Methods of Determining Electron Concentrations in the Magnetosphere from Nose Whistlers, *Technical Report No. 3454-1*, p. 52, Radioscience Laboratory, Stanford Electronics Laboratories, Stanford University, Stanford, California, 1972.
- Peden, I. C., G. E. Webber, and A. S. Chandler, Complex Permittivity of the Antarctic Ice Sheet in the VLF Band, *Radio Sci.*, **7**, 645-650, 1972.
- Raghuram, R., R. L. Smith, and T. F. Bell, VLF Antarctic Antenna: Impedance and Efficiency, *IEEE Trans. Antennas and Propag.*, **AP-22**, 334-338, 1974.

- Rastani, K., U. S. Inan, and R. A. Helliwell, DE 1 observations of Siple transmitter signals and associated sidebands, *J. Geophys. Res.*, 90, 4128-4140, 1985.
- Roederer, J. G., *Dynamics of Geomagnetically Trapped Radiation*, pp. 34, 52-55, Springer-Verlag, Berlin Heidelberg New York, 1970.
- Sa, L. A. D., and R. A. Helliwell, Structure of VLF Whistler Mode Waves in the Magnetosphere, *J. Geophys. Res.*, 93, 1987-1992, 1988.
- Shawhan, S. D., D. A. Gurnett, D. L. Odem, R. A. Helliwell, and C. G. Park, The Plasma Wave and Quasi-Static Electric Field Instrument (PWI) for Dynamics Explorer-A, *Space Sci. Instrum.*, 5, 535-550, 1981.
- Sonwalkar, V. S., T. F. Bell, R. A. Helliwell, and U. S. Inan, Direct Multiple Path Magnetospheric Propagation: A Fundamental Property of Nonducted VLF Waves, *J. Geophys. Res.*, 89, 2823-2830, 1984.
- Sonwalkar, V. S., and U. S. Inan, Measurements of Siple Transmitter Signals on the DE 1 Satellite: Wave Normal Direction and Antenna Effective Length, *J. Geophys. Res.*, 91, 154-164, 1986.